eISSN: 2791-8742
doi: 10.52460/src

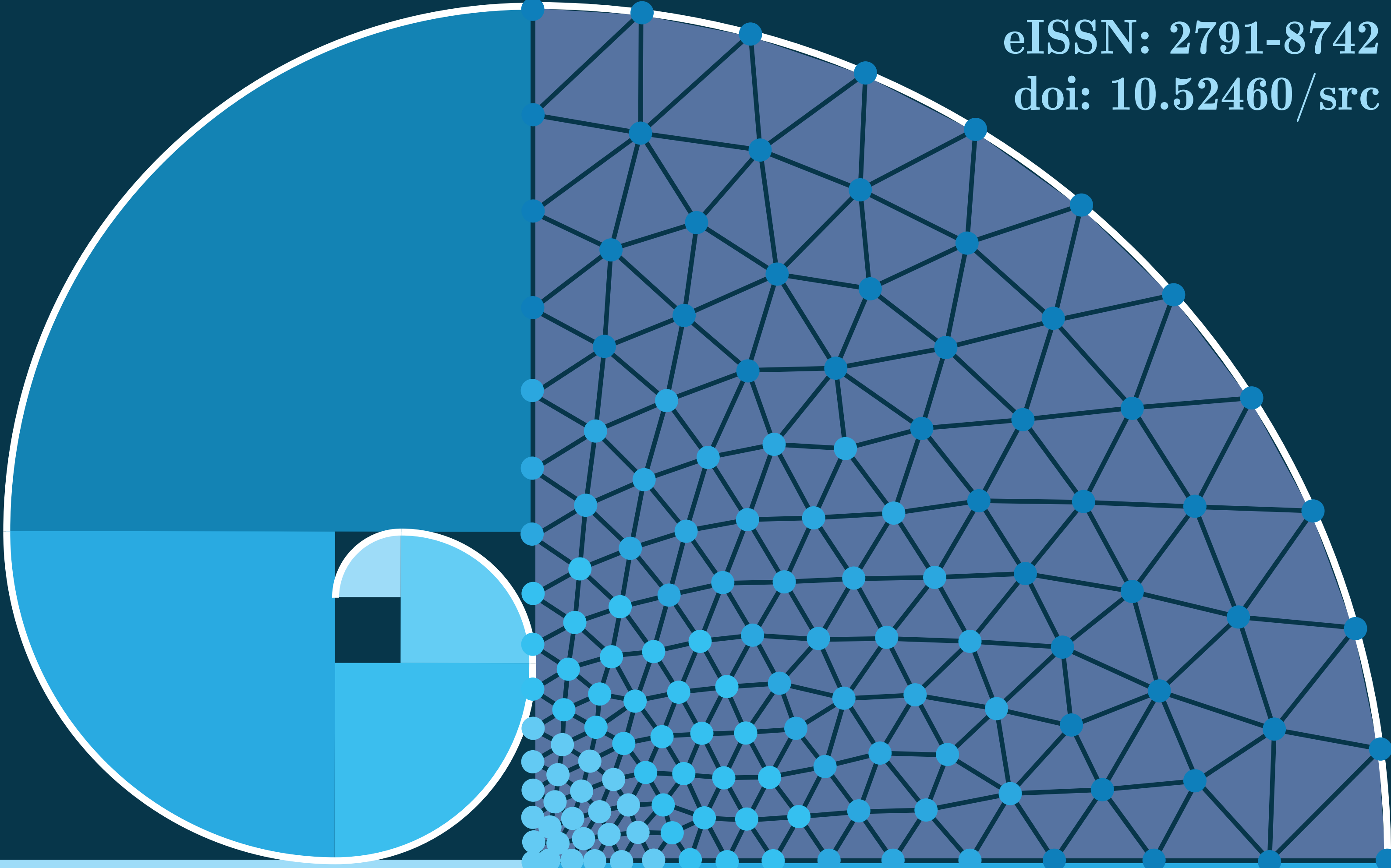

Scientific Research Communications

Volume 3
Issue 1
January 2023

Scientific Research Communications
Volume 3, Issue 1, 2023

Editorial

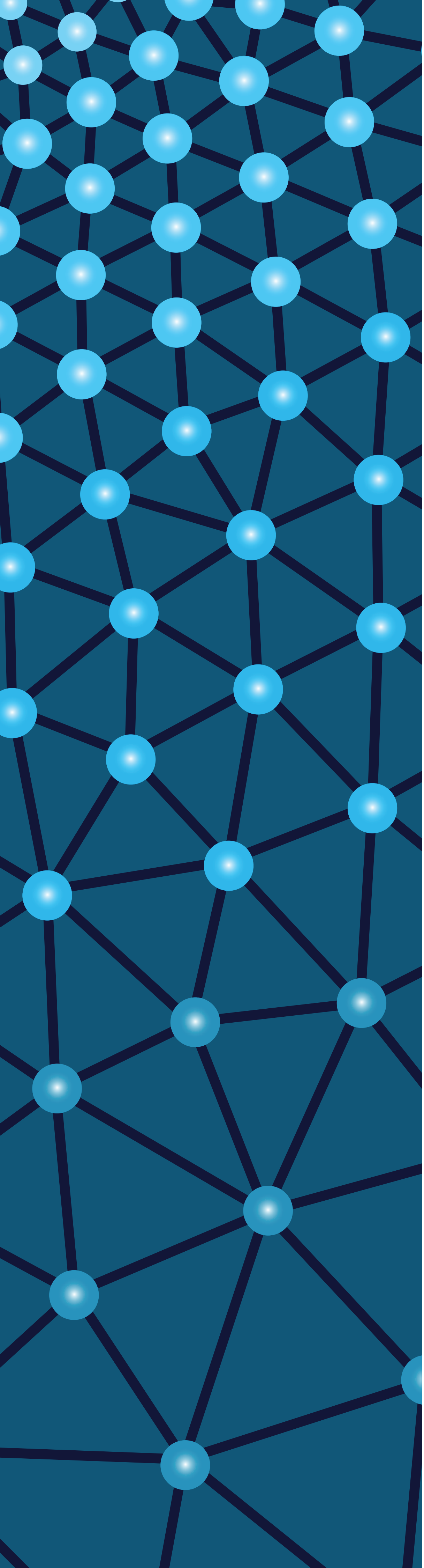

Scientific Research Communications
Volume 3, Issue 1, 2023

Contents

Scientific Research Communications

Review Article

Sci. Res. Comm. (2023)
Volume 3, Issue 1
doi: 10.52460/src.2023.001

Monitoring and Modelling of Sediment Flushing : A Review

Gregor Petkovšek[1,*]

[1] HR Wallingford, Howbery Park, Wallingford, Oxfordshire, United Kingdom
[*] Corresponding author: g.petkovsek@hrwallingford.com

Received: 14.10.2022 Accepted: 05.01.2023

Abstract

With ever decreasing potential for suitable new dam sites, sustainable use of existing water reservoirs is of paramount importance. In absence of appropriate measures, reservoir storage is continually reduced due to sedimentation. One option to remove sediment deposits is hydraulic flushing. During the flushing operation, bottom outlets are open and water and sediment released. Whether flushing successfully removes sediment depends on a number of factors, such as bottom outlets' capacity, reservoir shape and water availability. Modelling is often used to assess viability of flushing for sediment management in the reservoir, as well as to design the operations and optimize their scheduling. One-dimensional numerical models are preferred for long term simulations, assessments on of a large number of scenarios, and optimization studies. Two- and three-dimensional numerical models and physical models can be used, each on their own or in combination as hybrid models, to understand local scouring near the gates and other details of operation. Monitoring of flushing operations can help improving their efficiency while at the same time limit downstream impacts. General monitoring of the reservoir and its catchment can help understanding the sedimentation problem and thus facilitate preparation of efficient sediment management strategies. Live monitoring of sediment concentrations is possible with modern equipment though not without challenges, and reservoir survey can be performed faster. Earth observation techniques are also an attractive option, allowing to monitor large areas and areas of difficult access, as well as to provide historical information going back several decades. This paper reviews monitoring and modelling approaches published in the literature, as well as presents some previously unpublished analyses.

Keywords: Dams and reservoirs; numerical models; earth observation

1. Introduction

Construction of dams to impound rivers and create space for water storage has been attested through history, going back several millennia. Some dams have served many generations and even several civilizations (Smith, 1972; Schnitter, 1994; Bildirici, 2001) confirming the possibility of their sustainable use. Proserpina and Cornalbo dams in Spain are examples of such constructions (Castillo, 2007). Yet also in Spain, Valdinferno dam became completely sedimented and had to be abandoned shortly after its completion (Brown, 1944). Apart from hydrological and sedimentological factors, (un)sustainability issues have possibly arisen by somewhat unfortunate economic doctrines of the previous century, which argued for a fixed life time of dams. In the present time, there is a strong preference towards sustainable design and operation of water reservoirs, as is the case with other projects aimed at exploitation of natural resources.

The aim of sustainable reservoir management is to tackle sedimentation and its adverse impacts by achieving an equilibrium between sediment inflow and outflow (Morris, 2015). One of the management strategies is hydraulic flushing of deposited sediment (Schleiss et al., 2016). This method uses forces of flowing water to remove and release sediment that is deposited between two flushing cycles. The most effective type of flushing is the drawdown flushing (Morris and Fan, 1997), where flow forces are maximised and flow is free from backwater throughout the reservoir. This is performed by opening bottom outlets and drawing down the water level in the reservoir. To what degree a reservoir is amenable to flushing depends on various geographic, hydro-sedimentologic and technical factors (White, 2001). Drawdown flushing requires emptying and refilling of the reservoir, which may not always be feasible. Among other limitations is the width of the flushing channel, which may be limited to part of the reservoir width if the reservoir is wide, and result in removal of only a small proportion of sediment deposits. Further review of limitations, and how to address them, is presented in Petkovšek et al. (2020).

Flushing is successfully practiced in reservoirs of various sizes, from less than 1 million m^3 to large storage reservoirs with capacity of more than 1000 million m^3 (Table 1). Flushing is practiced in countries where storage loss to sedimentation exceeds one percent (e.g. China) as well as in the European Alps where it is ten times lower.

Table 1. Reservoirs where drawdown flushing has been practiced with success

Reservoir / Dam	Country	Year built	CAP (M m^3)	MAR (M m^3)	MAS (Mt) or *MAD (M m^3)	Source
Mangahao	New Zealand	1924	2	n/a	*0.03	Jowett (1984)
Zemo-Afchar	Georgia	1927	n/a	6600	5	UNESCO (1985)
Spencer	USA	1927	20.8	1500	*1	Boyd and Gibson (2016)
Barasona	Spain	1932	92	794	*0.25	Cobo (2008)
Jensanpei	Taiwan	1938	8.1	7	0.25	Wang et al. (2018)
Verbois	Switzerland	1943	15	10,000	0.33	Sumi (2008)
Gmund	Austria	1945	0.93	135	0.07	Morris and Fan (1997)
Genissiat	France	1948	53	11,000	0.73	Sumi (2008)
Lavey	Switzerland	1949	n/a	5700	*0.025	Bieri et al. (2012)
Palagnedra	Switzerland	1952	5.5	199	0.08	White (2001)
Agongdian	Taiwan	1953	36.7	54	0.38	Wang et al. (2018)
Cancano	Italy	1956	124	217	n/a	Espa et al. (2019)
Shuicaozi	China	1958	9.6	514	0.63	White (2001)
Heisonglin	China	1959	8.6	14.2	0.71	Morris and Fan (1997)
Barenburg	Switzerland	1960	1.7	3600	0.02	Sumi (2008)
Sanmenxia	China	1960	9,750	43,000	1600	Morris and Fan (1997)
Ferrera	Switzerland	1961	0.23	1300	0.008	Sumi (2008)
Uch-Kurgan	Kyrgyz Rep.	1961	56.4	15,000	13	UNESCO (1985)
Sefid-Rud	Iran	1962	1760	5000	50	Morris and Fan (1997)
Khashm El Girba	Sudan	1964	1300	12,000	85	Adam & Suleiman (2022)
Hengshan	China	1966	13.3	15.8	n/a	UNESCO (1985)
Cachí	Costa Rica	1966	54	1500	0.8	Morris and Fan (1997)
Fall Creek	USA	1966	140	520	0.05	Schenk and Bragg (2014)
Gebidem	Switzerland	1968	9	430	0.4	Morris and Fan (1997)
Rosegg	Austria	1973	19	6500	2	Steiner et al. (2004)
Santo Domingo	Venezuela	1974	3	450	0.2	Morris and Fan (1997)
Nanqin	China	1974	10.2	121	0.5	White (2001)

Table 1. Reservoirs where drawdown flushing has been practiced with success (continued)

Reservoir / Dam	Country	Year built	CAP (M m^3)	MAR (M m^3)	MAS (Mt) or *MAD (M m^3)	Source
Baira	India	1981	2.4	2700	0.3	White (2001)
Bodendorf	Austria	1982	0.9	1000	*0.04	Hartmann (2009)
Dashidaira	Japan	1985	9	1300	0.62	Sumi (2008)
St Egrève	France	1992	6.8	9500	2	Valette et al. (2013)
Fisching	Austria	1994	1.4	1500	*0.085	Harb (2013)
Angostura	Costa Rica	2000	17	3800	1.5	Hoven (2010)
Xiaolangdi	China	2000	13,000	41,000	1400	Ahn (2011)
Unazuki	Japan	2001	24.7	1800	0.96	Sumi (2008)

CAP = storage capacity, MAR = mean annual runoff, MAS = mean annual sediment yield, MAD = mean annual deposition

For flushing operation to be successful, it must be designed and planned carefully. Design and planning must be supported by flushing studies using evidence from field observation and monitoring. Hartmann (2009), White (2001) and others recommended use of physical and numerical models for flushing studies. Experimental studies, as well as monitoring and observation in nature can help closing gaps in knowledge, both in terms of general theoretical questions and to address and improve site-specific issues. Earth observation is a developing monitoring technique that is almost ready to be applied to aspects of reservoir flushing (e.g. the Hypos project). This paper reviews and analyses the selected modelling and some emerging earth observation monitoring approaches described in the literature and applied in practice.

2. Modelling

Natural processes can be modelled numerically, physically or through hybrid approaches. Each approach has its advantages and disadvantages.

Numerical models mathematically represent a set of ideas about natural processes and their relationships, proposed by experts. Although these ideas and models may not entirely correspond to the reality, they are still empirically known to be useful. Their performance is tested by comparing their numerical output with field or laboratory observations. If the two coincide satisfactorily, the model is accepted. This is often the case for simple and readily observable phenomena. Nevertheless, the degree of agreement between the model predictions and observations tends to decrease with more complex, more difficult to measure or uncommon phenomena. Some processes related to the reservoir sedimentation and flushing modelling fall into the latter category, for example bed load transport, sediment entrainment from bed, impact of sediment on turbulence of water flow etc. (Petkovšek and Kitamura, 2022). The main advantages of numerical models, compared to physical models, are fast execution and lower resource demand. They can cover large areas (e.g., coordinated flushing of reservoirs in chain, modelling of impacts on downstream reaches), use for optimization and trade-off analyses where a large number of runs over long time periods is required, easier coupling with habitat models for evaluation of environmental impact, etc.

The main advantage of physical models, over numerical models, is that they are governed by "true" natural processes. Physical models are however constructed at a scale, which requires certain degree of interpretation of their outputs, which is necessarily a human process. Furthermore, modelling of flushing requires modelling of many different processes in addition to flow of water, such as initiation of sediment motion, bedload, suspended load, secondary currents and bedforms. Each process has its different scaling laws which makes it difficult to select an overarching scaling approach. Olsen and Haun (2014) pointed out that as reservoirs are large, the scale used in a physical model must therefore be small, which makes modelling all relevant processes in a physical model more difficult.

To take advantage (and avoid disadvantages) of physical and numerical modelling, hybrid (also called composite) modelling was sometimes attempted.

2.1.Numerical Modelling

White (2001) suggested the use of 1D models to study feasibility of flushing. These models are the least complex and fastest to execute, while more resource demanding 2D or 3D models should be used where this is necessary (Figure 1). Examples include modelling of local impacts near outlets, simulation of wide reservoirs and reservoirs with complex geometries where flow direction and magnitude varies throughout the reservoir. Olsen and Haun (2014) suggested that 3D models are better suited to model flushing flows in reservoirs with training works or for flushing channels with bends, because they can simulate secondary currents, which by its nature is a 3D phenomenon. Alternatively, some 2D models can simulate sediment transport under secondary currents indirectly (Begnudelli et al., 2010), although they were not specifically tested for flushing channels with bends. A comparison of a 1D, 2D and 3D models that form the same modelling suite TELEMAC-MASCARET was performed by Valette et al., (2013). For a long and narrow St. Egrève reservoir in France, they used two separate flushing events to calibrate and validate each model. All three models were able to accurately predict the mass of sediment flushed during a typical flushing event and confirmed that for a linearly shaped reservoir, concluding 1D modelling was sufficient for most practical purposes.

There are some specific 2D or 3D phenomena related to reservoir sedimentation and flushing. Boyd and Gibson (2016) reported that discrepancies between observed values and HEC-RAS 1D model results were found due to the model not being able to represent lateral widening. Others include vertical sediment concentration distribution for simulation of sediment release through outlets or ingress into intakes. Approaches for modelling of these phenomena have been incorporated in 1D models to make them fit for these specific tasks. Fruchard and Camenen (2012) used the RubarBE 1D model developed at IRSTEA to simulate environmentally friendly flushing, where release was made through outlets at different heights with different sediment concentrations, in order to keep downstream sediment concentrations below the maximum permitted value. In addition to vertical concentration profile at dam, this 1D mode also takes into account slope stability concept to model slope instability during the development of flushing channel. HR Wallingford developed the 1D RESSASS model (Petkovšek and Roca, 2014) specifically for reservoir sedimentation, by incorporating modelling approaches to the vertical gradient of sediment concentration at dam with outlets at multiple levels, widening of flushing channel, slope stability, sediment compaction and turbid density currents. The RESSASS model can also simulate multiple reservoirs, as can GSTARS model (Ahn, 2011). For flushing, the most important property of a model is the ability to model channel widening and slope instability, which both mentioned models can do, as well as can the Courlis model (Valette et al., 2013).

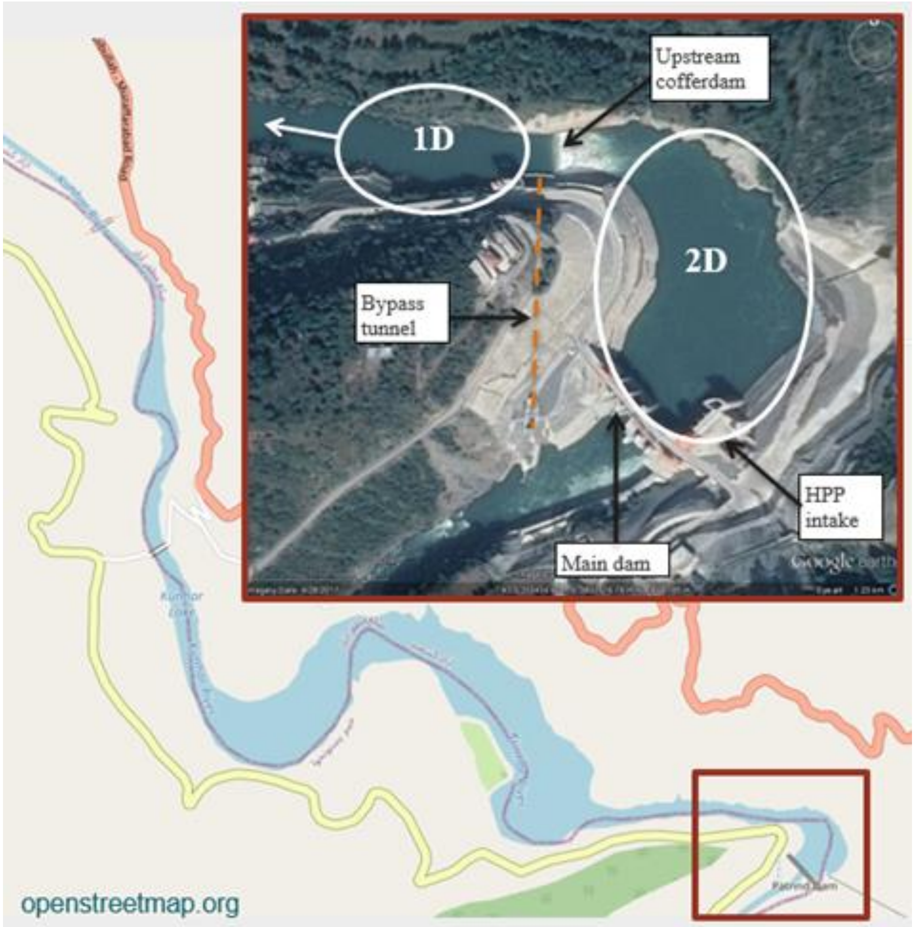

Figure 1. An example of a long narrow reservoir suitable for modelling with a 1D model, while the details near dam and intake are modelled with a 2D model

The use of 3D models has been increasing as their higher demand on computational resources is matched by more capable hardware. Harb (2013) modelled sediment flushing of two reservoirs in Austria, one with SSIIM and another with TELEMAC-3D. The former model was also used by Hoven (2010) to study flushing of a reservoir in Costa Rica, while the latter was used by Aliau et al. (2016) to model eco-friendly flushing of a reservoir in France. Omer et al. (2016) used Delft3D for a reservoir in Japan. A special 3D model for pressure flushing was developed by Sawadogo et al. (2019).

In addition to models that discretise the domain to a particular set of model nodes linked into a numerical mesh (1D, 2D and 3D), meshless models have been, although to a lesser degree, used to study sediment transport and flushing (Maneti et al., 2012; Zubeldia et al., 2018). In both cases, the Smoothed Particle Hydrodynamics (SPH) approach was used. With this approach, the computational points are not ordered in a particular system but follow the movement of fluid. The approach is well suited to cases where the area occupied by fluid(s) changes rapidly, such as rapid erosion of sediment from the reservoir bed during flushing.

For long term simulations, the quasi-steady modelling approach is attractive due to its ability to handle long time steps and generally being numerically more stable than the fully unsteady approach. However, it disregards the local acceleration term and wave propagation through a reservoir during drawdown and infill. This may have some impact on the results. Gibson and Crain (2019) compared the two approaches and the measured values of released sediment concentrations at the Fall Creek Dam, USA. Both approaches predicted similar peak values that were also coherent with the measurements, but overall, the unsteady approach predicted higher values than the quasi-steady approach. Ahn (2011) compared predicted and measured bed level changes in cross sections and longitudinal sections of the Xiaolangdi reservoir. They found that the unsteady approach performed better in the case of cross sections, while quay-steady approach performed better in the case of the longitudinal section.

Flushing can have large impacts on downstream environment. To analyse and ultimately minimise these impacts, the outputs of the sediment models can be coupled with environmental assessment. Moridi and Yazidi (2017) modelled suspended sediment concentrations during flushing operations for Dez Dam in Iran and applied the model results to consider social, environmental and water resources impacts in the study area. Impacts of flushing can be also evaluated by habitat models, for example CASiMiR (Jorde, 1996; Schneider et al., 2001).

2.2.Physical Modelling

Physical modelling supports both theoretical investigations of reservoir flushing processes as well as case-specific flushing studies.

Lai and Shen (1996) theoretically investigated the flushing channel evolution and the amount of sediment released. Kantoush and Schleiss (2014) investigated the effects of the reservoir geometry on sediment deposition and flushing with a series of systematic laboratory experiments. The authors found that both deposition and flushing rates can be well related to a shape factor that they formulated based on geometric properties of the reservoir. Sindelar et al. (2016) investigated the effect of weir height and reservoir widening at the dam on sediment continuity for run-of-river hydropower project on small and medium sized gravel bed rivers. Guillén-Ludeña et al. (2022) performed ninety laboratory experiments to study the efficacy (released sediment to water ratio) of flushing with respect to the volume of stored water, bed slope and sediment size. Only the stored water was used for flushing without any additional inflow. They found that the efficacy increases with slope and decreases with water volume. There was little difference in flushing efficacy between coarse and medium sand, while efficacy for fine sand was somewhat lower, which the authors attributed to the apparent cohesion.

Physical models have been developed to study feasibility and support design of flushing operations in real reservoirs. Examples include Ratnayesuraj et al. (2015), who used a scaled model (1:250) for studies at the Rantambe Reservoir, Sri Lanka. A physical modelling at 1:70 scale for Chamera Hydro-Electric Project in India was constructed to study performance of the reservoir, including sediment flushing (Isaac et al. 2014). For the Cerro del Aguila dam in Peru, a physical model was constructed covering the area from 1000 m upstream of the dam to 350 m downstream from the dam (Sayah et al., 2014). Harb (2013) reported on a physical model of the Schönau reservoir on the river Enns in Austria in 1:40 scale and using lightweight material to represent fine deposits, alongside a 3D numerical model, to study flushing.

2.3.Hybrid Modelling

Hhybrid models use both physical and numerical models. The aim is to take advantage of the respective strengths of each model and to avoid their respective weaknesses. Typically, the numerical model covers the whole domain of interest in space and time at a 1:1 scale, while the physical model is used to add specific information where it is deemed necessary. Possible links between the numerical and physical models are shown in Figure 2.

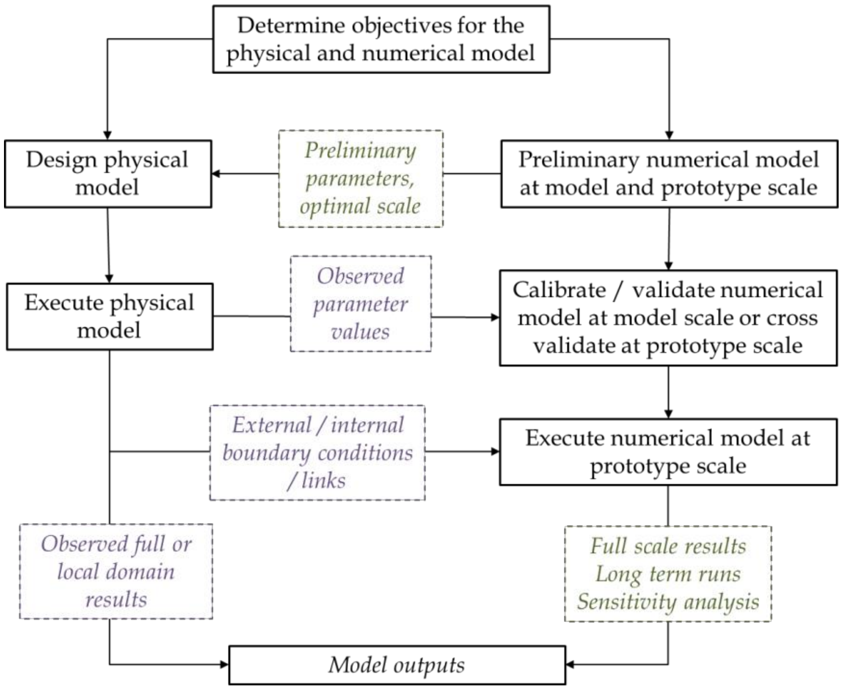

Figure 2. Possible links between a physical and numerical model in the hybrid modelling approach

Hybrid modelling was proposed for flushing studies (Reisenbüchler et al., 2020) and implemented by some authors, e.g. Harb (2013) and Sayah et al. (2014). Schleiss et al. (2011) used a hybrid model of a pressure flushing operation at Räterichsboden reservoir in Switzerland. Numerical modelling was performed by the FLOW-3D software and a 1:35 scale physical model was constructed, used them for cross-checking as well as tested them against one field observations during an annual bottom gate functional testing. The authors concluded that the results were of sufficient similitude to make the cross-checked models suitable for prediction of sediment flushing, including prediction of released sediment concentration as function of outlet gate opening height. Peteuil et al. (2017) presented a hybrid model of the Champagneux reservoir. They applied a numerical model TELEMAC-3D to the whole reservoir, constructed a physical model at a 1:35 scale for the area near dam, and a CFD numerical model of spillway section at both scales. The main aim of modelling was to accurately represent bottom shear stress, which is the main factor in assessment of sediment erosion.

3. Earth Observation Assisted Monitoring

Earth observation has been used extensively in water related research as well as practical application. While not as accurate as the direct on-the-ground observations, earth observation has its advantages, mainly due to large (full) spatial coverage, as well as typically lower processing effort and cost (Peterson et al., 2018).

Flushing channel is the central feature of flushing that also determines how much sediment can be flushed from the reservoir, given the available water discharge, as well as sediment characteristics and slopes. Observations of the final width of flushing channels at different conditions was performed in the past and an empirical relation between the two was proposed (White, 2001). Earth observation data offer an opportunity to enhance this database using historical data for reservoirs where flushing has been practiced purposely as well as where a flushing channel has formed spontaneously in the sediment delta during periodic drawdown. Historical outflows are usually measured and recorded, sediment characteristics are also known, while the width of the flushing channel at different times and locations can be estimated form satellite imagery (Figure 3).

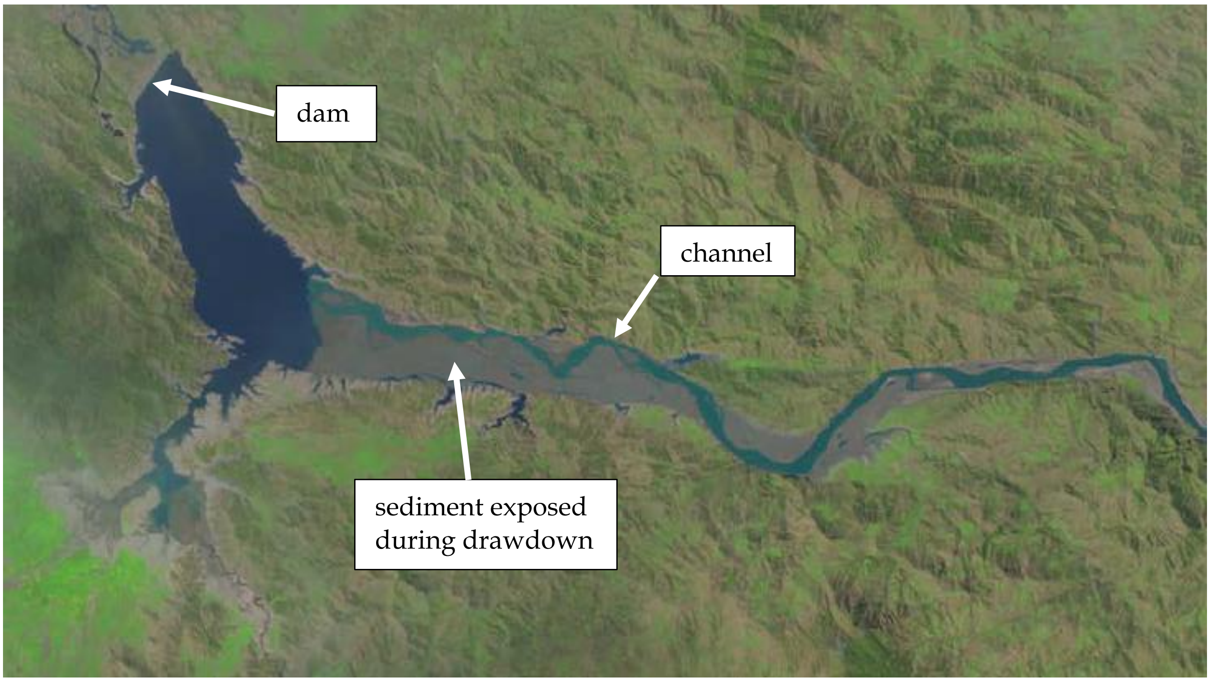

Figure 3. : Scouring channel in Tarbela reservoir sediment delta during the drawdown season shown in a Landsat 7 satellite image from 26/03/2000.

Another application related to flushing and fate of released sediment transport is related to monitoring of sediment concentration in the reservoirs and rivers. In large reservoirs, monitoring based on satellite imagery had been reported already in 1970s (Ritchie et al., 1976). With better spatial resolution and development of assessment techniques, the scope of application can now be extended to smaller reservoirs and longer river reaches. Zhang et al. (2022) used the multispectral imagery and two-stage non-linear relationship between suspended sediment concentration and reflectance in various bands, valid for the range 2-850 PPM, and applied it to the whole mainstream Yangtze River.

The rate of flushing depends on the compaction rate of fine sediment, to some extent (White, 2001). The compaction rate is usually determined from undisturbed samples obtained by in-situ coring. An earth observation-based approach to study compaction rates could be carried out by employing the remote InSAR (interferometric synthetic aperture radar) technology. This method uses radar imagery provided by satellites and can, under certain circumstances, measure surface movements with precision of a few millimeters. In principle, this enables relatively fast and efficient scanning of wide areas, as was done at a large scale, for example for the Meghna River delta in Bangladesh (Higgins et al., 2014). However, there are certain points to note and challenges at present state with the method as it is usually applied. Firstly, the method requires a more or less continuous dataset of 30 images over a period of one year, without major changes to the tracked points on surface (e.g. points can move/subside but they should not be covered by water or other material). This is challenging in many dams where sediment is only exposed during short period of time. Secondly, the measurement is in the line-of-sight (LOS) of the satellite. As it can be safely assumed that the compaction movement is in the vertical direction only, this is not a particular concern. Thirdly, the usually applied method of persistent scatterers works well for solid types of surfaces (buildings, rocks, firm ground) but struggles with coherence (consistent points) in vegetated areas or over water. If sediment is frequently covered by water, the third challenge is related to the first. When sediment is exposed for long periods, it may also be overgrown by vegetation. This again restricts the application of InSAR.

4. Conclusions

Loss of storage due to sedimentation is an important challenge to the sustainable use of water resources. Sediment flushing is potentially a very efficient sediment management strategy that must be carefully designed. Numerical and physical modelling can contribute to the design. Knowledge gaps can be filled through experimental investigation and observation in nature, including through earth observation.

Different modelling methods can be used for assessment of different aspects of flushing operations. For the detailed studies of water and sediment flow near outlets, in particular where vertical component of flow is important, 3D numerical models are most suitable. Further assurance can be obtained by the hybrid approach where numerical modelling is combined with physical modelling in order to benefit from the advantages of each approach: real processes on a physical model and a prototype scale on a numerical model. In time, these models are typically used for the flushing operation itself or its most critical part during drawdown. For long term simulations, scenario exploration or optimization, taking into account the whole reservoir or even the river system impacted by flushing, the use of 3D (or 2D) models is likely to be computationally too expensive. Lighter 1D models can produce satisfactory results, especially if the reservoir is long and narrow. Apart from shorter run times, these models also require less input parameters, that relate to well tested quantities and processes, which is not always the case with the parameters required for the more complex 3D models.

Earth observation is becoming popular but still underused data source for flushing studies. Wealth of information could be obtained from earth observation sources to fill the knowledge gaps with respect to formation of flushing channel and its width. Monitoring of sediment concentrations in rivers is becoming more feasible with higher resolution of satellite imagery and its multispectral characteristics. Sediment compaction can be studied through InSAR techniques, although some important limitations related to the persistency of observed points (scatterers) remain a challenge.

Author Statement

The author confirms sole responsibility for the following: data collection, analysis and interpretation of results, and manuscript preparation.

Conflict of Interest

The author declares no conflict of interest.

References

Adam, E., & Suleiman, M. (2022). Reservoir Sediment Management Practices in Sudan: A Case Study of Khashm El-Girba Dam. *Natural Disaster Science and Mitigation Engineering: Wadi Flash Floods*. Springer, Singapore: Sumi, T., Kantoush, S. A., Saber, M. https://doi.org/10.1007/978-981-16-2904-4_18.

Ahn, J. (2011). Numerical Modelling of Reservoir Sedimentation and Flushing Processes. *PhD Thesis*. Colorado State University, Fort Collins, USA.

Aliau, D., Peteuil, Ch., & Huybrechts, N. (2016). Using an Eco-friendly Flushing Event to Calibrate 3D Sediment Transport Model through a Reservoir: the Case Study of Champagneux Run-of-River Dam on the Rhone River, France. *Proceedings of the XXIII TELEMAC-MASCARET User Conference 2016*. 49-53.

Begnudelli, L., Valiani, A., & Sanders, B. F. (2010). A Balanced Treatment of Secondary Currents, Turbulence and Dispersion in a Depth-integrated Hydrodynamic and Bed Deformation Model for Channel Bends. *Advances in Water Resources,* 33, 17–33.

Bieri, M., Müller, M., Boillat, J.L., Schleiss, A.J. (2012). Modeling of Sediment Management for the Lavey Run-of-River HPP in Switzerland. *Journal of Hydraulic Engineering,* 138(4), 340-347.

Bildirici, M. (2001). Historical dams of Anatolia. *Proc 11th International Conference on Water in Antiquity*. Cura Aquarvm, Israel, 137-144.

Boyd, P., & Gibson, S. (2016). Applying 1D Sediment Models to Reservoir Flushing Studies: Measuring, Monitoring, and Modeling the Spencer Dam Sediment Flush with HEC-RAS. Vicksburg: U.S. *Army Engineer Research and Development Center*. ERDC/CHL CHETN-XIV-52.

Brown, C. B. (1944). The Control of Reservoir Silting. Washington, D. C.: *United Stated Department of Agriculture*, 512.

Castillo, J.C. (2007). Roman Dams in Spain. *Revista Obras Publicas*, 3475, 65-80 (in Spanish).

Cobo, R. (2008). Sediments in Spanish Reservoirs. *Ingenieria del Agua,* 15(4).

Espa, P., Batalla, R.J., Brignoli, M.L., Crosa, G., Gentili, G., & Quadroni, S. (2019). Tackling Reservoir Siltation by Controlled Sediment Flushing: Impact on Downstream Fauna and Related Management Issues. *PLoS ONE,* 14(6). https://doi.org/10.1371/journal.pone.0218822.

Fruchard, F., & Camenen, B. (2012). Resarvoir Sedimentation: Different Type of Flushing - Friendly Flushing; Example of Genissiat Dam Flushing. *ICOLD International Symposium on Dams for a Changing World*. Kyoto, Japan.

Gibson, S., & Crain. J. (2019). Modeling Sediment Concentrations during a Drawdown Reservoir Flush: Simulating the Fall Creek Operations with HEC-RAS. Vicksburg: U.S. *Army Engineer Research and Development Center*. ERDC/TN RSM-19-7. http://dx.doi.org/10.21079/11681/33884.

Guillén-Ludeña, S., Toapaxi, J.A., & Castillo, L.G. (2022). Flushing Capacity of a Stored Volume of Water: An Experimental Study. *Water,* 14(2607). https://doi.org/10.3390/w14172607.

Harb. G. (2013). Numerical Modeling of Sediment Transport Processes in Alpine Reservoirs. *PhD Dissertation*, Graz University of Technology, Graz, Austria.

Hartmann, S. (2009). Sustainable Sediment Management in Alpine Reservoirs Considering Ecological and Economical Aspects: Sediment Management in Alpine Reservoirs – Recommendation and Best Practice. *ALPRESERV Project Report*. 7. http://www.alpine-space.org/2000-2006/temp-results16.html.

Higgins, S.A., Overeem, I., Steckler, M.S., Syvitski, J.P.M., Seeber, L., & Humayn Akhter, S. (2014). InSAR Measurements of Compaction and Subsidence in the Ganges-Brahmaputra Delta, Bangladesh. *JGR Earth Surface,* 119(8), 1768-1781.

Hoven, L.E. (2010). Three-dimensional Numerical Modelling of Sediments in Water Reservoirs. *Master's thesis*. NUST, Trondheim, Norway.

Isaac, N., Eldho, T.I., & Gupta, I.D. (2014). Numerical and Physical Model Studies for Hydraulic Flushing of Sediment from Chamera-II Reservoir, Himachal Pradesh, India. *ISH Journal of Hydraulic Engineering,* 20(1), 14-23.

Jorde, K. (1996). Ecological Evaluation of Instream Flow Regulations Based on Temporal and Spatial Variability of Bottom Shear Stress and Hydraulic Habitat Quality. *Proceedings of the Second International Symposium on Habitat Hydraulics, Ecohydraulics 2000*. Quebec City, Canada, 163-174.

Jowett, I. (1984). Sedimentation in New Zealand Hydroelectric Schemes. *Water International, 9,* 172-176.

Kantoush, S.A., & Schleiss, A.J. (2014). Influence of Geometry Shape Factor on Trapping and Flushing Efficiencies. *Proceedings of River Flow 2014*. Lausanne, Switzerland, 129-137.

Lai, J.S., & Shen, H.W. (1996). Flushing Sediment through Reservoirs. *J. Hydraul. Res*., 34, 237–255.

Manenti, S., Sibilla, S., Gallati, M., Agate, G., & Guandalini, R. (2012). SPH Simulation of Sediment Flushing Induced by a Rapid Water Flow. *Journal Hydraulic Engineering,* 138, 272–284.

Moridi, A., & Yazidi. J. (2017). Sediment Flushing of Reservoirs under Environmental Considerations. *Water Resources Management* 31(6), 1899–1914.

Morris, G.L. (2015). Management Alternatives to Combat Reservoir Sedimentation. *Proceedings of Int Workshop on Sediment Bypass Tunnels*. Zurich, Switzerland.

Morris, G.L., & Fan, J. (1997). *Reservoir Sedimentation Handbook*. New York: McGraw-Hill.

Olsen, N.R.B., & Haun, S. (2014). Free Surface Algorithms for 3D Numerical Modelling of Reservoir Flushing. *Proceedings of River Flow 2010*. Karlsruhe: Bundesanstalt für Wasserbau (BAW), 1105-1110.

Omer, A.Y.A., Huismans, Y., Sloff, K., & Kitamura, Y. (2016). The Effect of Different Gate Opening Patterns on Reservoir Flushing and Morphological Changes Downstream a Dam. *Deltares project DEL026*. The Netherlands.

Peterson, K.T., Sagan, V., Sidike, P., Cox, A.L., & Martinez, M. (2018). Suspended Sediment Concentration Estimation from Landsat Imagery along the Lower Missouri and Middle Mississippi Rivers Using an Extreme Learning Machine. *Remote Sens*., 10, 1503.

Peteuil, C., Alliau, D., Wirz, C., Fretaud, T., Decachard, M., Roux, S., Reynaud, S., Boisson, N., Vollant, A., & Baux, Y. (2017). Evaluating Favorable Conditions for Sediment Transport in Reservoirs: Champagneux Dam Case Study, France. *Proceedings of 85th Annual Meeting of International Commission on Large Dams*. Prague, Czech Republic.

Petkovšek, G., & Roca, M. (2014). Impact of Reservoir Operation on Sediment Deposition. *Proceedings of ICE, Water Management* 167(10), 577-584.

Petkovšek, G., Roca, M., & Kitamura, Y. (2020). Sediment Flushing from Reservoirs: A Review. *Dams and Reservoirs,* 30(1), 12-21, DOI 10.1680/jdare.20.00005.

Petkovšek, G., & Kitamura, Y. (2022). Numerical Modelling of Reservoir Flushing: A Review. *14th International Conference on Hydroscience & Engineering*. Urla, Türkiye.

Ratnayesuraj, C. R., Rifas, K. M., Risly, S., & Weerakoon, S. B. (2015). Model Study of Sediment Flushing in Rantambe Reservoir. *Proceedings 3rd International Symposium on Advances in Civil and Environmental Engineering Practices for Sustainable Development*. Galle, Sri Lanka, 300-306.

Reisenbüchler, M., Bui, M. D., Skublics, D., & Rutschmann, P. (2020). Sediment Management at Run-of-River Reservoirs Using Numerical Modelling. *Water 12(1), 249*, doi:10.3390/w12010249.

Ritchie, J.C., Schiebe, F.R., & McHenry, J.R. (1976). Remote Sensing of Suspended Sediment in Surface Water. *Photogramm. Eng. Remote Sens*, 42, 1539–1545.

Sawadogo, U., Basson, G.R, &Schneiderbauer, S. (2019). Physical and Coupled Fully Three-dimensional Numerical Modeling of Pressurized Bottom Outlet Flushing Processes in Reservoirs. *International Journal of Sediment Research*, 34(5), 461-474.

Sayah, S. M., Bonanni, S., & Fenelli, A. (2014). Physical and Numerical Modelling of Cerro del Águila Dam: Hydraulic and Sedimentation. *Proceedings of Hydro 2014 Conference (Hydropower and Dams)*. Como, Italy.

Schenk, L.N., & Bragg, H.M. (2014) Assessment of Suspended-Sediment Transport, Bedload, and Dissolved Oxygen during a Short-Term Drawdown of Fall Creek Lake, Oregon, Winter 2012–13. *USGS Open File Report* 2014-1114.

Schleiss, A. J., Boes, R. M., Daneshvari, M., & De Cesare, G. (2011). Hybrid Modeling of Sediment Management during Drawdown of Räterichsboden Reservoir. *Proc. of International Symposium on Dams and Reservoirs under Changing Challenges, (79th Annual Meeting of ICOLD)*. 421-428.

Schleiss, A. J., Franca, M. J., Juez, C., & De Cesare, G. (2016). Reservoir Sedimentation. *Journal of Hydraulic Research,* 54(6), 595–614.

Schneider, M., Jorde, K., Zollner, F., & Kerle, F. (2001). Development of a User-friendly Software for Ecological Investigations on River Systems, Integration of a Fuzzy Rule-based Approach. *Proceedings of 15th International Symposium on Environmental Informatics*. ETH Zurich, Switzerland.

Schnitter, N. J. (1994). *A History of Dams – The Useful Pyramids*. A.A. Balkema. Netherlands.

Sindelar, C., Schobesberger, J., & Habersack, H. (2016). Effects of Weir Height and Reservoir Widening on Sediment Continuity at Run-of-River Hydropower Plants in Gravel Bed Rivers. *Geomorphology,* 291, 106–115.

Smith, N. (1972). *A History of Dams*. Citadel Press Inc, New Jersey, USA.

Steiner, H. A., Moser, A., & Kaefer, S. (2004). Naturschutz und Kunst als Landschaftsgestalterische Element bei Hochwassesschutzmassnahmen im Stauraum Feistriz-Ludmannsdorf (Nature Protection and Arts as Elements of Landscape Engineering Measures for Flood Protection in the Storage Reservoirs Bistrica-Bilčovs). *Int Symp INTERPRAEVENT*. Riva, Italy.

Sumi, T. (2008). Evaluation of Efficiency of Reservoir Sediment Flushing in Kurobe River. *Proc. Fourth International Conference on Scour and Erosion*. D-18, 608-613.

UNESCO (1985). Methods of computing sedimentation in lakes and reservoirs*. UNESCO Report*.

Valette, E., Villaret, C., Tassi, P., & Jodeau, M. (2013). St Egrève Reservoir – Multi-Dimensional Modelling of Flushing and Evolution of the Channel Bed. *Proceeding of the XXth TELEMAC-MASCARET User Conference 2013*. Karlsruhe, Germany, 127-132.

Wang, H. W., Kondolff, M., Tullos, D., & Kuo, W. C. (2018). Sediment Management in Taiwan's Reservoirs and Barriers to Implementation. *Water,* 10, 1034, doi:10.3390/w10081034.

White, R. (2001). *Evacuation of Sediments from Reservoirs*. London: Thomas Telford.

Zhang, C., Liu, Y., Chen, X., & Gao, Y. (2022). Estimation of Suspended Sediment Concentration in the Yangtze Main Stream Based on Sentinel-2 MSI Data. *Remote Sens., 14, 4446*. https://doi.org/10.3390/rs14184446.

Zubeldia, E. H., Fourtakas, G., Rogers, B. D., & Farias, M. M. (2018). Multi-phase SPH Model for Simulation of Erosion and Scouring by Means of the Shields and Drucker–Prager Criteria. *Advances in Water Resources,* 117, 98-114. https://doi.org/10.1016/j.advwatres.2018.04.011.

Scientific Research Communications

Research Article

Sci. Res. Comm. (2023)
Volume 3, Issue 1
doi: 10.52460/src.2023.002

Lucas Polynomial Solution of a Single Degree of Freedom System

Nurcan Baykuş Savaşaneril[1,*]

[1] Izmir Vocational School, Dokuz Eylül University, Izmir, Turkey
[*] nurcan.savasaneril@deu.edu.tr

Received: 19.01.2023 Accepted: 30.01.2023

Abstract

Free vibration of a single degree of freedom system is a fundamental topic in mechanical vibrations. The present study introduces a novel and simple numerical method for the solution of this system in terms of Lucas polynomials in the matrix form. Particular and general solutions of the differential equation can be determined by this method. The method is illustrated by a numerical application and the results obtained are compared with those of the exact solution.

Keywords: Vibration Spring-mass-damper system, Lucas polynomials and series, collocation points and matrix method

1. Introduction

Ordinary differential equations, a crucial part of applied mathe- matics, have many applications in different science and engineering disciplines. The study of the free vibration of damped spring-mass systems having single degree of freedom is fundamental to the understanding of advanced subjects in mechanical vibrations. In many cases, a complicated system can be idealized as a single degree of freedom spring-mass system. Therefore, solving the equations of motion of this system would serve for many other more advanced problems. There are various useful methods for calculating solutions of a spring-mass-damper system excited by a harmonic force. Kurt and Çevik (2008) and Savaşaneril (2018) proposed a matrix method for solving this problem.

The present study introduces a novel and simple method in terms of Lucas polynomials in the matrix form. Lucas polynomials have been used by many researchers for the solution of differential and integral equations. Gümgüm et al. (2018) proposed a Lucas expansion approach for functional integro-differential equations involving variable delays. Baykus (2017) used this method to find the approximate solution of high-order pantograph type delay differential equations with variables delays. Gümgüm et al. (2020) gave an approach for Second Order Nonlinear Differential Equations via Lucas polinomial. The method has also been used to solve nonlinear equations by Gümgüm et al. (2019). Yüzbaşı and Yıldırım (2020) proposed Pell-Lucas collocation method to solve high-order linear Fredholm-Volterra integro-differential equations. In addition, Kübra et al. (2021) , Yüzbaşı and Ismailov (2018), Kürkçü and Sezer (2022) proposed a different the matrix method.

In general, an m^{th} order differential equation can be written as:

$$\sum_{k=0}^{m} P_k x^k(t) = f(t), \tag{1}$$

with initial conditions

$$\sum_{k=0}^{m-1} a_{ik} x^{(k)}(a) = \lambda_i, \quad i = 0,1,...,m-1, \tag{2}$$

where $P_k(t)$ are analytic functions defined on $a \le t \le b$, and a_{ik}, λ_i are suitable constants. In the present method, the solution of Eq. (1) is expressed in the Lucas polynomial form as:

$$x(t) = x_N(t) = \sum_{n=0}^{N} a_n L_n(t), \tag{3}$$

where $L_n(t)$ are the Lucas polynomials and a_n, $n=0,1,2,\ldots N$ are unknown coefficients (Baykus, N., 2017).

2. Fundamental Matrix Relations

In this section, we constitute the matrix forms of the unknown function $x(t)$ defined by Eq. (3) and the derivative $x^{(k)}(t)$ in Eq. (1). We can first write the truncated Lucas series (3) in the matrix form, for $n=0,1,2,\ldots.N$:

$$x(t) = x_N(t) = \mathbf{L}(t)\mathbf{A}, \tag{4}$$

where

$$\mathbf{L}(t) = \begin{bmatrix} L_0(t) & L_1(t) & \cdots & L_N(t) \end{bmatrix}, \quad \mathbf{A} = \begin{bmatrix} a_0 & a_1 & \cdots & a_N \end{bmatrix}^T \tag{5}$$

$$\begin{aligned} & L_0(t) = 2, \\ & L_1(t) = t, \\ & \vdots \\ & L_{n+1}(t) = t\,L_n(t) + L_{n-1}(t), \quad n \ge 1. \end{aligned} \tag{6}$$

Then, by using the Lucas polynomials $L_n(t)$ given by Eq. (6), we write the matrix form $\mathbf{L}(t)$ as follows:

$$\mathbf{L}(t) = \mathbf{T}(t)\mathbf{M}, \tag{7}$$

where

$$\mathbf{T} = \begin{bmatrix} 1 & t & \cdots & t^N \end{bmatrix}. \tag{8}$$

If N is odd,

$$\mathbf{M}^T = \begin{bmatrix} 2 & 0 & 0 & \cdots & 0 \\ 0 & \frac{1}{1}\binom{1}{0} & 0 & \cdots & 0 \\ \frac{2}{1}\binom{1}{1} & 0 & \frac{2}{2}\binom{2}{0} & \cdots & 0 \\ 0 & \frac{3}{2}\binom{2}{1} & 0 & \cdots & 0 \\ \vdots & \vdots & \vdots & \ddots & 0 \\ \frac{(n-1)}{\binom{\frac{n-1}{2}}{}}\binom{\frac{n-1}{2}}{\frac{n-1}{2}} & 0 & \frac{(n-1)}{\binom{\frac{n+1}{2}}{}}\binom{\frac{n+1}{2}}{\frac{n-3}{2}} & \cdots & 0 \\ 0 & \frac{n}{\binom{\frac{n+1}{2}}{}}\binom{\frac{n+1}{2}}{\frac{n-1}{2}} & 0 & \cdots & \frac{n}{n}\binom{n}{0} \end{bmatrix}. \tag{9}$$

If N is even,

$$\mathbf{M}^T = \begin{bmatrix} 2 & 0 & 0 & \cdots & 0 \\ 0 & \frac{1}{1}\binom{1}{0} & 0 & \cdots & 0 \\ \frac{2}{1}\binom{1}{1} & 0 & \frac{2}{2}\binom{2}{0} & \cdots & 0 \\ 0 & \frac{3}{2}\binom{2}{1} & 0 & \cdots & 0 \\ \vdots & \vdots & \vdots & \ddots & 0 \\ 0 & \frac{(n-1)}{\binom{\frac{n}{2}}{}}\binom{\frac{n}{2}}{\frac{n-2}{2}} & 0 & \cdots & 0 \\ \frac{n}{\frac{n}{2}}\binom{\frac{n}{2}}{\frac{n}{2}} & 0 & \frac{n}{\binom{\frac{n+2}{2}}{}}\binom{\frac{n+2}{2}}{\frac{n-2}{2}} & \cdots & \frac{n}{n}\binom{n}{0} \end{bmatrix}. \tag{10}$$

By the matrix relations in Eq. (4) and Eq. (7), it follows that,

$$x_N(t) = \mathbf{T}(t)\mathbf{MA}. \tag{11}$$

Besides, it is well known from Gümgüm et al. (2019) that the relation between $\mathbf{T}(t)$ and its derivative $T^{(k)}(t)$ is of the form:

$$\mathbf{T}^{(k)}(t) = \mathbf{T}(t)\,\mathbf{B}^k, \tag{12}$$

where

$$\mathbf{B} = \begin{bmatrix} 0 & 1 & 0 & \cdots & 0 \\ 0 & 0 & 2 & \cdots & 0 \\ \vdots & \vdots & \vdots & \ddots & \vdots \\ 0 & 0 & 0 & \cdots & N \\ 0 & 0 & 0 & \cdots & 0 \end{bmatrix} \tag{13}$$

and $\mathbf{B}^0$ is a unit matrix.

By using Eq. (11) and Eq. (12), we have the matrix relation:

$$x_N^{(k)}(t) = \mathbf{T}(t)\,\mathbf{B}^k\mathbf{M}\,\mathbf{A}, \quad k = 0,1,\ldots,m. \tag{14}$$

Inserting the collocation points

$$x_i = a + \frac{b-a}{N} i, \quad i = 0,1,\ldots,N \tag{15}$$

into Eq. (1) gives

$$\sum_{k=0}^{m} P_k x^k(t_i) = f(t_i), \tag{16}$$

which can be written in matrix form as:

$$\mathbf{W} = \left[w_{pq}\right] = \sum_{k=0}^{m} P_k \mathbf{T}(t)\,\mathbf{B}^k\mathbf{M}, \quad p,q = 0,1,\ldots,N.$$

Now, by the relation Eq. (14), we can obtain the condition matrix form for the initial conditions (Eq. (2)) $\mathbf{U}_i\mathbf{A}=\lambda$ or

$$\left[\mathbf{U}_i \quad ; \quad \lambda_i\right], \quad i = 0,1,\ldots,m-1 \tag{17}$$

such that

$$\mathbf{U}_i = \sum_{k=0}^{m-1} a_{ik} T(a)\mathbf{B}^k\mathbf{M} = \left[u_{i0} \quad u_{i1} \quad \cdots \quad u_{iN}\right]. \tag{18}$$

In order to determine the particular solution of the problem in matrix form, Eq. (17) is written briefly in the form:

$$\mathbf{WX} = \mathbf{F} \qquad \text{or} \qquad \left[\mathbf{W} \quad ; \quad \mathbf{F}\right], \tag{19}$$

where

$$\mathbf{W}=\left[w_{pq}\right]=\sum_{k=0}^{m}P_k\mathbf{T}(t)\,\mathbf{B}^k\mathbf{M},\quad p,q=0,1,...,N. \tag{20}$$

By consequence,

$$\mathbf{X}=\mathbf{W}^{-1}\mathbf{F}, \tag{21}$$

which yields the desired Lucas cofficients x_n, $n=0,1,2,\ldots,N$ of the particular solution.

Now, to solve the problem, the following augmented matrix is constructed by replacing the last 2 rows of [**W** ; **F**] of Eq. (22) by the 2-row matrix [$\mathbf{U}_i$; λ_i]:

$$\left[\mathbf{W};\mathbf{F}\right]=\begin{bmatrix} w_{00} & w_{01} & & w_{0N} & ; & f_0(t)\\ w_{10} & w_{11} & & w_{1N} & ; & f_1(t)\\ \vdots & \vdots & & \vdots & \vdots & \\ w_{N-m,0} & w_{N-m,1} & \cdots & w_{N-m,N} & ; & f_{N-m}(t)\\ u_{00} & u_{01} & \cdots & u_{0N} & ; & \lambda_0\\ u_{10} & u_{11} & \cdots & u_{1N} & ; & \lambda_1\\ \vdots & \vdots & \vdots & \vdots & \ddots & \vdots\\ u_{m-1,0} & u_{m-1,1} & \cdots & u_{m-1,N} & ; & \lambda_{m-1} \end{bmatrix}. \tag{22}$$

3. Lucas Matrix – Collocation Technique of The Problem

In this study, the viscously damped single degree of freedom system subjected to harmonic excitation (Inman, 2001):

$$M\,\ddot{x}+C\,\dot{x}+Kx=F_0\cos wt, \tag{23}$$

with initial conditions

$$\begin{aligned} x(0)&=\lambda_0\\ \dot{x}(0)&=\lambda_1 \end{aligned} \tag{24}$$

will be solved by Lucas matrix method. In this case, we have m=2 and the constants $P_2=M$, $P_1=C$, $P_0=K$ *in* Eq. (1):

$$M\,\ddot{x}+C\,\dot{x}+Kx=\sum_{k=0}^{2}P_k\mathbf{T}(t)\,\mathbf{B}^k\mathbf{M}\,\mathbf{X}. \tag{25}$$

3.1. Particular solution

In order to determine the particular solution of the problem in matrix form, Eq. (23) is written briefly in the form:

$$\mathbf{W}=\left[w_{pq}\right]=\sum_{k=0}^{2}P_k\mathbf{T}(t)\,\mathbf{B}^k\mathbf{M},\quad p,q=0,1,...,N\ . \tag{26}$$

By consequence,

$$\mathbf{X}=\mathbf{W}^{-1}\mathbf{F}, \tag{27}$$

which yields the desired Lucas cofficients x_n, $n=0,1,2,\dots,N$ of the particular solution.

3.2. General solution

To determine the general solution, the matrix form of the boundary conditions (21) is written as:

$$\mathbf{U}_i=\sum_{k=0}^{1} a_{ik}T(a)\mathbf{B}^k\mathbf{M}=\begin{bmatrix}u_{i0} & u_{i1} & \cdots & u_{iN}\end{bmatrix} \qquad i=0,1 \tag{28}$$

Now, to solve the problem, the following augmented matrix is constructed by replacing the last 2 rows of [**W** ; **F**] of Eq. (26) by the 2-row matrix [$\mathbf{U}_i$; λ_i]:

$$\left[\mathbf{W};\mathbf{F}\right]=\begin{bmatrix} w_{00} & w_{01} & \cdots & w_{0N} & ; & f_0 \\ w_{10} & w_{11} & \cdots & w_{1N} & ; & f_1 \\ \vdots & \vdots & \ddots & \vdots & ; & \vdots \\ w_{N-2,0} & w_{N-2,1} & \cdots & w_{N-2,N} & ; & f_{N-2} \\ u_{00} & u_{01} & \cdots & u_{0N} & ; & \lambda_0 \\ u_{10} & u_{11} & \cdots & u_{1N} & ; & \lambda_1 \end{bmatrix}. \tag{29}$$

In Eq. (25), if $rank\widetilde{\mathbf{W}}=rank\left[\widetilde{\mathbf{W}};\tilde{\mathbf{F}}\right]=N+1$, then the coefficient matrix A is uniquely determined and so the solution of the problem Eq. (1)-(2) is obtained as:

$$x_N(t)=\mathbf{L}(t)\mathbf{A} \text{ or } x_N(t)=\mathbf{T}(t)\mathbf{M}\mathbf{A}. \tag{30}$$

4. Numerical Example

A spring-mass-damper system with a mass of M = 10 kg, damping coefficient of C = 20 kg/s and spring stiffness of K = 4000 N/m subject to an excitation force of amplitude $F_0=100N$ and frequency $\omega=10$ rad/s is considered with initial conditions $x(0)=0.01, \dot{x}(0)=0$. The matrix operations in this section are performed by using Wolfram Mathematica 13.0.

The exact solution is given by (Inman, D.J., 2001):

$$x(t)=\tan^{-1}\frac{x_0\omega_d}{v_0+\xi\omega_n x_0}, \qquad A=\frac{1}{\omega_d}\sqrt{(v_0+\xi\omega_n x_0)^2+(x_0\omega_d)^2}, \qquad x=0,$$

for free response, and,

$$x(t)=\tan^{-1}\frac{\omega_d(x_0-x\cos\theta)}{v_0+(x_0-x\cos\theta)\xi\omega_n-\omega x\sin\theta}, \qquad A=\frac{x_0-x\cos\theta}{\sin\phi},$$

$$\theta=\tan^{-1}\frac{2\xi\omega_n\omega}{\omega_n^2-\omega^2}, \qquad x=\frac{f_0}{\sqrt{(\omega_n^2-\omega^2)^2+(2\xi\omega_n\omega)^2}},$$

for forced response. From the (11) fundamental matrix equation is:

$$10\mathbf{T}(t).\mathbf{B}^2\mathbf{M}^T\mathbf{A}+20\mathbf{T}(t).\mathbf{B}\mathbf{M}^T\mathbf{A}+4000\mathbf{T}(t)\mathbf{M}^T\mathbf{A}=100\cos 10t. \tag{31}$$

By using (15) the collocation points for N = 5 is calculated as:

$$\left\{0,\frac{1}{5},\frac{2}{5},\frac{3}{5},\frac{4}{5},1\right\},$$

and we obtain:

$$\mathbf{W}=\begin{bmatrix} 8000 & 20 & 8020 & 60 & 8080 & 100 \\ 8000 & 820 & 8188 & 2506.4 & 8763.84 & 4335.04 \\ 8000 & 1620 & 8676 & 5149.6 & 10830.7 & 9604.32 \\ 8000 & 2420 & 9484 & 8181.6 & 14514.9 & 17075.2 \\ 8000 & 3220 & 10612 & 11794.4 & 20204.2 & 28226.1 \\ 8000 & 4020 & 12060 & 16180 & 28440 & 45000 \end{bmatrix}.$$

The augmented matrix for this fundamental matrix equation is calculated as:

$$\left[\mathbf{W};\mathbf{G}\right]=\begin{bmatrix} 8000 & 20 & 8020 & 60 & 8080 & 100 & ; & 100 \\ 8000 & 820 & 8188 & 2506.4 & 8763.84 & 4335.04 & ; & 28.3662 \\ 8000 & 1620 & 8676 & 5149.6 & 10830.7 & 9604.32 & ; & -65.3644 \\ 8000 & 2420 & 9484 & 8181.6 & 14514.9 & 17075.2 & ; & 96.017 \\ 2 & 0 & 2 & 0 & 2 & 0 & ; & 0.01 \\ 0 & 1 & 0 & 3 & 0 & 5 & ; & 0 \end{bmatrix}.$$

Performing the necessary matrix operations, the particular solution is determined as:

$$x_p(t)=184063-160037L_1(t)-123718L_2(t)+88047.9L_3(t)+31679L_4(t)-20838L_5(t)$$

in Lucas polynomial form, and the general solution is:

$$x_g(t)=323.256-313.714L_1(t)-216.497L_2(t)+168.799L_3(t)+54.8743L_4(t)-38.5364L_5(t)$$

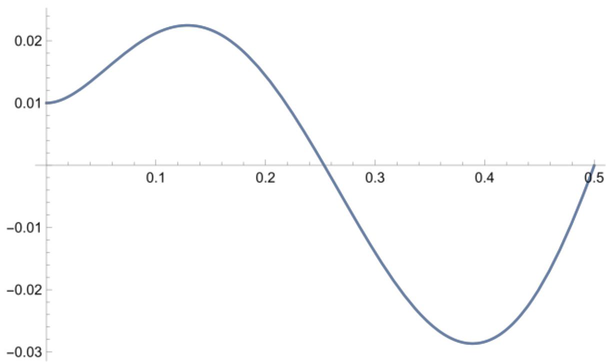

Figure 1. The general solution

Finally $x_{40}(t)$ is obtained for N=40:

$$x_{40}(t) = -5.894703961761931.10^{7} + 4.809657176756848.10^{8}.L_1(t) + 7.467470466915241.10^{7}.L_2(t)$$
$$-4.293391442061826.10^{8}.L_3(t) - 8.93847819837741.10^{8}.L_4(t) + 3.132395109718503.10^{8}.L_5(t) +$$
$$6.567014129734314.10^{7}.L_6(t) - 1.59204644360381.10^{8}.L_7(t) - 2.54515240071604.10^{7}.L_8(t)$$
$$+3.495715330499887.L_9(t) + 6614643.904937126.L_{10}(t) + 1.748782280616832.10^{7}.L_{11}(t)$$
$$-7920874.169940725.L_{12}(t) - 1.725364834634807.10^{7}.L_{13}(t) + 9165009.245850491.L_{14}(t)$$
$$5109995.376942811.L_{15}(t) - 5203828.325874632.L_{16}(t) + 220814.41721369085.L_{17}(t)$$
$$+1459939.562524835.L_{18}(t) - 569693.2886912221.L_{19}(t) - 112126.0439566288.L_{20}(t)$$
$$+167623.56494754046.L_{21}(t) - 43435.56898627258.L_{22}(t) - 17906.61385994068.L_{23}(t)$$
$$-10833.4183322996338..L_{24}(t) - 3193.338078951663.L_{25}(t) + 25413.043724168358.L_{26}(t)$$
$$-1638.6461992483767.L_{27}(t) - 10040.921604866502.L_{28}(t) + 1137.8678286578668.L_{29}(t)$$
$$1236.9842049196193.L_{30}(t) + 3300786570862636.L_{31}(t) - 174.6007432535557.L_{32}(t)$$
$$-65.0753966189064.L_{33}(t) + 35.56471110532434.L_{34}(t) - 26.896999946160374.L_{35}(t)$$
$$7.621730624316185.L_{36}(t) - 3.0780533665079806.L_{37}(t) + 6.4648253275926315.L_{38}(t)$$
$$-3.293481976937444.L_{39}(t) + 0.4951794203008488.L_{40}(t)$$

The results for different values of N are compared in Table 1. In the table, it is obviously seen that the Lucas solution approaches the exact solution as the truncation limit N is increased.

Table 1. Convergence of the Lucas results to those of exact solution

	Exact	Present Method (N =5)	Present Method (N =30)	Present Method (N = 40)
t	x(t)	x_5(t)	x_{30}(t)	x40 (t)
0	0.010000000102	0.010000000000033538	0.0099998963996768	0.010000037786085159
0.1	0.026606378588454577	0.021218558662097035	0.026608246698293588	0.02660616339402371
02	0.002080749042409633	0.014399161349069003	0.00207760236634558	0.0020807331586712163
0.3	−0.04851575510425815	−0.01401641114458152	−0.04851778585172134	−0.048516383083797576
0.4	−0.022765129712940937	−0.02837548614445584	−0.022765300714933545	−0.02276530628618173
0.5	0.019920584607770103	−0.00005820215181184807	0.01991818146927926	0.019921048858392965
0.6	0.021295471543613383	0.04627878810085573	0.021294628886607825	0.0212938860227041
0.7	0.023585587433570195	−0.013541385405768658	0.023586714873090386	0.023585824521433096
0.8	0.007669134885655218	−0.4494595130334105	0.007668879581615329	0.0076684916857630014
0.9	−0.03468236386751298	−1.723424008541791	−0.034679219126701355	−0.034682015888392925
1	−0.033476404064609305	−4.535634612144179	−0.03263649344444275	−0.03311382979154587

As N increased, better results were obtained. The efficiency and validity of the method are obvious.

5. Conclusions

A Lucas polynomial matrix solution has been presented for the periodic motion of an underdamped single degree of freedom spring-mass system subjected to harmonic excitation. Both particular and general solutions of the differential equation can be determined by this method. The results show a very good agreement with the method of undetermined coefficients (exact solution). The solution can also be applied to higher order systems with the same simplicity and application of the method to these problems offers a considerable facility. The method is applicable to any function that can be expanded to Lucas series. Accurate results can be obtained with rather low values of the truncation limit N; however, in order to have a better approximation, the truncation limit should be increased.

Author Statement

The author confirms sole responsibility for the following: study conception and design, data collection, analysis and interpretation of results, and manuscript preparation.

Conflict of Interest

The authors declare no conflict of interest.

References

Baykus, N. and Sezer, M. (2017), “Hybrid Taylor-Lucas Collocation Method for Numerical Solution of High-Order Pantograph Type Delay Differential Equations With Variables Delays,”*Applied Mathematics & Information Sciences*, 11(6), 1795-1801.

Gümgüm, S., Savaşaneril, N. B., Kürkçü, Ö. K. and Sezer, M. (2020), “Lucas Polynomial Approach for Second Order Nonlinear Differential Equations”, *Süleyman Demirel Üniversitesi Fen Bilimleri Enstitüsü Dergisi*, 24(1), 230-236.

Gümgüm, S., Savaşaneril, N. B., Kürkçü, Ö. K. and Sezer, M. (2019), “Lucas Polynomial Solution of Nonlinear Differential Equations With Variable Delay”, *Hacettepe Journal of Mathematics and Statistics*, 1-12.

Gümgüm, S., Savaşaneril, N. B., Kürkçü, Ö. K. and Sezer, M. (2018), “A Numerical Technique Based on Lucas Polynomials Together With Standard and Chebyshev-Lobatto Collocation Points for Solving Functional Integro-Differential Equations Involving Variable Delays,” *Sakarya University Journal of Science*, 22(6), 1659-1668.

Gümgüm, S., Savaşaneril, N., B., Kürkçü, Ö. K. and Sezer, M. (2019), “Lucas Polynomial Solution of Nonlinear Differential Equations With Variable Delay,” *Hacettepe Journal of Mathematics and Statistics*, 1-12.

Inman, D.J. (2001), “Engineering Vibration (2nd Ed.),” Prentice-Hall, New Jersey.

Biçer, K. E., Sezer, M. and Kazaz, M. (2021), "Numerical Solutions of System of First Order Normalized Linear Differential Equations by Using Bernoulli Matrix Method," *Celal Bayar University Journal of Science*, 17(2), 153–158.

Kurt, N. and Cevik, M. (2008), “Polynomial Solution of the Single Degree of Freedom System by Taylor Matrix Method,” *Mechanics Research Communications*, 35(8), 530-536.

Kürkçü, Ö. K. and Sezer, M. (2022) , " Charlier Series Solutions of Systems of First Order Delay Differential Equations with Proportional and Constant Arguments", *Scientific Research Communications,* 2(1), 1-11.

Sezer M. and Daşcıoğlu, A.A. (2007), "A Taylor Method for Numerical Solution of Generalized Pantograph Equations With Linear Functional Argument," *J. Comput. Appl. Math.*, 200, 217–225.

Savaşaneril, N. B. (2018), "Laguerre Series Solutions of the Delayed Single Degree-of-Freedom Oscillator Excited by an External Excitation and Controlled by a Control Force," *Journal of Computational and Theoretical Nanoscience*, 15(2), 606-610.

Yüzbaşı, Ş. and Ismailov, N. (2018) "An Operational Matrix Method for Solving Linear Fredholm-Volterra Integro-Differential Equations", *Turkish Journal of Mathematics*, 4242, 243-256.

Yüzbaşı, Ş. and Yıldırım, G. (2020), "Pell-Lucas Collocation Method to Solve High-Order Linear Fredholm-Volterra Integro-Differential Equations and Residual Correction," *Turkish Journal of Mathematics*, 4(4), 243-256.

Scientific Research Communications

Research Article

Sci. Res. Comm. (2023)
Volume 3, Issue 1
doi: 10.52460/src.2023.003

A Comparison of The Performances of Conventional and Low Salinity Water Alternating Gas Injection for Displacement of Oil

Emmanuel Bucyanayandi[1,*] Muhammed Said Ergül[1] İbrahim Kocabaş[1]

[1] İzmir Kâtip Çelebi University, Department of Energy Engineering, Çiğli Main Campus, İzmir, Türkiye
*Correspondent author: bucyaemmanuel@gmail.com

Received: 28.07.2022 Accepted: 29.01.2023

Abstract

This study focuses on identifying the crucial physical and chemical factors, such as gravity, initial oil phase, injection depth, vertical to horizontal permeability contrast, and salinity of injected water for improving oil recovery factor during water alternating gas (WAG) injection. The conventional WAG injection attracts interest from oil and gas industry and hence, has become one of the most reliable enhanced oil recoveries (EOR) techniques. During WAG injection, due to gravity effect, water subsides below oil layer while gas overflow above the oil layer. In fact, water sweeps bottom zones of the reservoir and gas sweep the attic oil at the upper zones of the reservoir.

Although the conventional WAG does improve oil recovery factor, there still remains a substantial amount of oil in reservoir pores due to rock-fluid and fluid-fluid interfacial tensions (IFT) that leads to the capillary forces impeding the microscopic displacement efficiency. The low salinity waterflooding (LSWF) was therefore proposed to break the IFT between rock clay and fluids, and further increase oil recovery factor. Recent researches revealed that LSWF alters oil-wet reservoir to water-wet behavior. This wettability alteration is believed to be the main mechanism of LSWF to improve oil recovery. Other mechanisms of LSWF include multi-ion exchange (MIE) between rock clay minerals and injected salt water, pH increase, and fines migration. In this study, the CMG GEM simulator was used to simulate conventional WAG injection and LSWAG injection. The simulation results showed that there is an increase of oil recovery factor of about 6% for WAG injection with low salinity water of 1027ppm to sea water of 51,346 ppm. The simulations have also showed that the physical factors namely, gravity, initial oil phase, injection depth, vertical to horizontal permeability contrast are influential on the displacement efficiency and must be studied thoroughly in the design of LSWAG operations besides the salinity and chemical composition of the injection water.

Keywords: Waterflooding; CO_2 flooding; conventional WAG injection; low salinity WAG injection; displacement efficiency of WAG processes

1. Introduction

The economically feasible production of oil is achieved in three stages namely, primary recovery, secondary recovery, and tertiary or enhanced oil recovery. The primary oil recovery stage refers to the flow of oil from the reservoir into the production wells due to the natural energy/forces that exists in the reservoir. These forces are classified as formation drive due to the compressional energy stored in the oil, connate water and porous formation in the reservoir rock, solution gas drive due the dissolved gas in the oil, gas cap drive due to presence of a gas cap, water drive due to the compressional energy stored in the neighboring large size aquifers, and gravity drive.

The oil recovery factor or the ratio of ultimate cumulative oil production to initial oil in place in the primary stage ranges from 5% to 30%. Secondary recovery methods, namely immiscible waterflooding and gas flooding are usually applied at some stage of primary recovery to enhance and accelerate the production. The additional oil recovery factor due to secondary recovery methods ranges from 5% to 20%. On the average, the total oil recovery factor after primary and secondary recovery methods is between 15% and 40% (Bonder, 2010). The enhanced oil recovery (EOR) methods are applied to recover an additional economically feasible amount of oil that usually remains in the reservoir after primary and secondary recovery methods. Figure 1 shows the partitions of oil recovery percentage by each type of oil recovery methods. It shows that the additional oil recovery factor of 15% to 25% can be achieved by applying EOR methods.

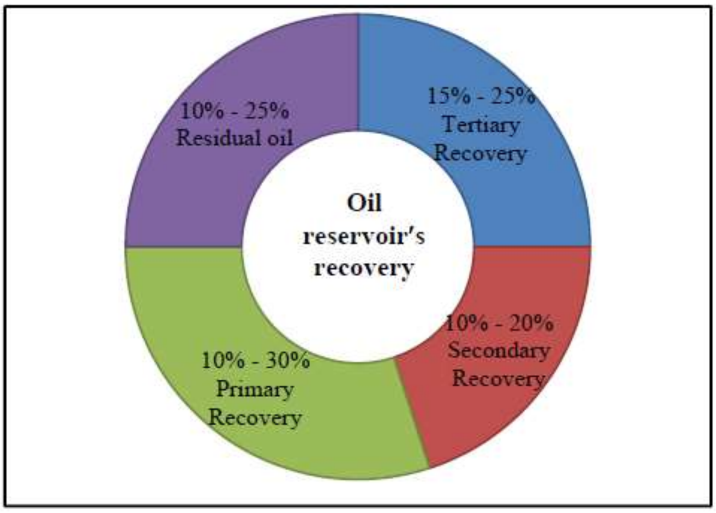

Figure 1. Reservoir oil recovery (Muggeridge et al., 2014; Zitha et al., 2011)

While waterflooding and gas injection are separately considered as secondary oil recovery mechanisms, their combination known as water alternating gas (WAG) injection is referred to as a tertiary or an enhanced oil recovery method. Gas has substantially lower viscosity and density compared to crude oil. Therefore, as a secondary recovery method continous gas injection provides poor macroscopic sweep efficiency due to its high mobility ratio and low density that joinly cause early gas breakthrough (Hustad and Holt, 1992). Therefore, WAG injection was initially used to target improving macroscopic sweep efficiency in gas injection. In fact, conventional WAG injection improves the macroscopic sweep efficiency compared to water flooding and both microscopic and macroacopic displacement efficiency compared to gas injection (Touray, 2013). This improvement is attained by water sweeping the bottom part of the reservoir due to its high-density and gas driving the attic oil due to its low density(Knappskog, 2012). However, the conventional WAG still has its limitations due to strong IFT that hold oil molecules to rock clay surface by multi-valent ions.

Low salinity waterflooding was proposed and applied to improve oil recovery factor further from classical waterflooding. The low salinity waterflooding could increase oil recovery factor from 6 to 12% which takes waterflooding recovery to 8 to 19% orginal oil in place (OOIP) (McGuire et al., 2005). The increase of oil recovery by low salinity water flooding is attributed to four mechanisms: changing the wettability to water wet due to the clay migration; increasing of pH due to $CaCO_3$ that results in wettability alteration; generation of surfactants and reduction of interfacial tension (IFT); multicomponent ion exchange (MIE) between clay minerals and injected brine (Bernard, 1967; Buckley et al., 1989; McGuire et al., 2005).

Low salinity waterflooding changes the reservoir wettability from oil wet to water wet. In other words, low salinity waterflooding affects the oil wet but has no effect on water wet sample. It was found that high concentrations of Ca^{+2} and Mg^{+2} ions in brine formation make the sample more oil wet. Low salinity water flooding also changes the composition of rock and its properties. The experiments showed that the low salinity water dissolves anhydride cements in rock formation. As a result, low salinity water flooding also increases the permeability of reservoir rock (Hamouda and Valderhaug, 2014).

Knowing the effectiveness of conventional WAG and Low Salinity Waterflooding individually, one wonders what could be the performance of low salinity WAG compared to conventional WAG under the influence of other operational and/or design factors such as gravity, initial oil phase, injection depth, and vertical to harizontal permeability contrast. Therefore, this study is aimed to evaluate and compare the performances of conventional WAG injection and LSWAG in improving the oil recovery factor in an 80 ft thick and 1000 ft long sandstone reservoir by considering these factors. These factors are selected and adjusted to evaluate the efficiencies of sea water WAG and low salinity WAG injection. The influence of these factors sequentially on waterflooding, CO_2 gas injection, and WAG injection is investigated with numerical simulations by using CMG-GEM reservoir simulator.

2. Theory of WAG Processes

2.1. Darcy's Law

The flow of fluids in porous medium is governed by Darcy's law. For multiphase flow in porous medium, Darcy's velocity of individual fluid ($\vec{V_i}$) is proportional to effective permeability (k_i) and pressure gradient with gravity effect ($\nabla P - \rho g \nabla d$) and inversely proportional to the viscosity μ_i. In oil reservoirs, velocities of gas, oil, and water are hence calculated by using the flowing Eq. (1), Eq. (2) and Eq. (3) respectively as by Darcy's law.

For gas:
$$\vec{V_g} = -\frac{k_g}{\mu_g}\left(\nabla P_g - \rho_g g \nabla d\right) \tag{1}$$

For oil:
$$\vec{V_o} = -\frac{k_o}{\mu_o}\left(\nabla P_o - \rho_o g \nabla d\right) \tag{2}$$

For water:
$$\vec{V_w} = -\frac{k_w}{\mu_w}\left(\nabla P_w - \rho_w g \nabla d\right) \tag{3}$$

2.2. Relative Permeability

The concept of relative permeability was adopted to express the effective permeability to the base permeability (usually effective permeability to oil at irreducible water saturation). Relative permeability to fluid (k_{ri}) is the ability of medium to conduct that fluid in presence of other fluids. Relative permeability depends on microscopic distribution and saturation of fluid. It is experimentally correlated with saturation of fluid. The Modified Brooks-Corey (MBC) correlation is a power law model proposed to determine relative permeability for both experimental and field data. Relative permeability is therefore correlated with fluid saturation as shown in the following Eq. (4), Eq. (5) and Eq. (6). (Alpak et al., 1999; Behrenbruch and Goda, 2006; Brooks and Corey, 1964).

$$k_{rw} = k_{rw,max}\left(\frac{S_w - S_{wc}}{1 - S_{or} - S_{wc} - S_{gc}}\right)^{n_w} \tag{4}$$

$$k_{ro} = k_{ro,max}\left(\frac{S_o - S_{or}}{1 - S_{or} - S_{wc} - S_{gc}}\right)^{n_o} \tag{5}$$

$$k_{rg} = k_{rg,max}\left(\frac{S_g - S_{gc}}{1 - S_{or} - S_{wc} - S_{gc}}\right)^{n_g} \tag{6}$$

Where, S_w is water saturation, S_{wc} is irreducible water saturation, S_o is oil saturation, S_{or} is residual oil saturation, S_g is gas saturation, S_{gc} is irreducible gas saturation, n_w, n_o, and n_g refer to corey exponents and they range from 1 to 6, and $k_{rw,max}$, $k_{ro,max}$, and $k_{rg,max}$ are the maximum or end point relative permeabilities.

3. Theory of the Mechanisms of Low Salinity Waterflooding

Low salinity waterflooding is a technique of injecting water with low concentration of salts between (salinity: 1000-2000 ppm). It is a chemical technique that was recently adopted to improve oil production. From different experimental analysis of core flooding, chemical changes of rock and fluids due to low salinity flooding are the main reason of oil recovery improvement. The mechanism of low salinity waterflooding is based on breaking the electric forces exhibited by high salinity formation water to oil to rock surface. Hence, certain conditions that include the presence of clay minerals like calcite and dolomite and the polarity of oil, they are the key conditions for effectiveness of low salinity waterflooding (Bernard, 1967; Tang and Morrow, 1999). The following are the main mechanisms by which low salinity waterflooding improve the oil displacement in the reservoir:

3.1. Multicomponent Ion Exchange (MIE)

In the reservoir, oil is attached to rock surface by bonding to multivalent cations. By injecting the low salinity water, K^+ and Na^+ ions replace these multivalent ions like Ca^{2+} and Mg^{2+}. As a result, the oil is released from rock surface in the form of calcium or magnesium carboxy complex. Unlike for high salinity water that strengthen the oil bonding to clay, injection of low salinity water weakens these bonding for ion exchange to occur. The effectiveness of low salinity water flooding therefore depends on composition of water formation and injection brine.

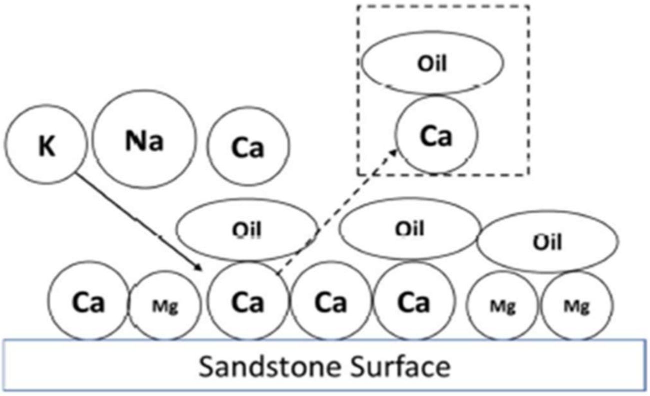

Figure 2. Low salinity mechanisms of multiple ions exchange (MIE) with potassium replacing calcium and liberation of oil in the form of calcium carboxylate complex, modified after (Srisuriyachai and Muchalintamolee, 2014).

3.2. Wettability Alteration

According to different researches, low salinity water injection changes the wettability. The low salinity waterflooding alters the reservoir from oil wet to water wet. It was obtained that low salinity waterflooding affect the oil wet and it has no effect on water wet sample. It was found that high concentrations of Ca^{2+} and Mg^{2+} ions in brine formation make the sample more oil wet. The effect of reservoir rock mineralogy on the application of low salinity water was also reviewed. Low salinity waterflooding therefore changes the composition of rock and its properties. The experiments showed that the low salinity water dissolves anhydride cements in rock formation. As the result, low salinity water flooding increases the permeability of reservoir rock (Tang and Morrow, 1999).

3.3. Increased pH Effect and Reduced Interfacial Tension (IFT)

Low salinity water flooding leads to generation of hydroxyl ions to reactions with rock minerals. This causes the pH increase from 7 to 8 and even to 9. In fact, low salinity waterflooding like alkaline flooding reduces the interfacial tensions between oil and rock and increases pH. The IFT are the forces that hold oil into pore spaces. The increase of pH and reduction of interfacial tensions between reservoir rock and fluids alter the rock to more water wet and hence improve oil recovery. In addition, oil with its chemical structure, the increase of pH facilitates the in-situ surfactant generation by saponification reactions as shown below (McGuire et al., 2005). In this case, low salinity water flooding acts like surfactant flooding and cause oil dispersion into water.

$$\mathrm{(RCOO)_3C_3H_5 + 3\ NaOH \rightarrow 3(RCOONa) + C_3H_5(OH)_3}$$

$$\mathrm{2(RCOONa)} + Ca\mathrm{(HCO_3)_2 \rightarrow (RCOO)_2Ca + 2(NaHCO_3)}$$

4. Methodology

The CMG-GEM one of the reservoir simulators developed by Computer Modeling Group (CMG) was used to simulate different scenarios of waterflooding, gas injection, and WAG injection. GEM is a generalized equation of state model reservoir simulator, i.e., it is an equation of state compositional simulator for multi-component reservoir fluids. GEM is used to simulate all the processes involving chemical change in the reservoir but at a constant temperature.

4.1. Reservoir and Fluids Modelling

The actual data from the Cranfield oil field reservoir and some assumptions were considered to model the reservoir and formation fluids. As published in the Mississippi oil and gas board (MOGB) publication in 1966, Cranfield oil field was discovered in 1943, its reservoir has a geological dome with gas cap, oil ring and water at different depths (Mississippi Oil and Gas Board, 1966). Until 1966, the total oil and gas production was at least 37mmbbl and 672 bscf respectively, then the reservoir was subjected to secondary oil recovery by water drive in 2005, and with enhanced oil recovery by CO_2 flooding in 2008 at some part of the field (Hovorka et al., 2008). A CO_2 sequestration test was also carried out in Cranfield pilot size of 9400 ft x 8400ft with net pay of 80ft (Delshad et al., 2013; Hosseini et al., 2013). In this study, the reservoir model in Table 1 was built by using the data published on Cranfield oil field reservoir.

Table 1. Reservoir model

Parameter	Value
Reservoir size (ft)	1000 x 100x 80
Number of grid blocks	20x1x8
Reservoir depth (ft)	9950
Reservoir Temperature (°F)	257
Initial oil saturation	0.6
Initial Pressure (psi)	4650
Salinity, TDS (ppm)	150,000

By using GEM builder and Winprop, a reservoir model was built by inputting the data to be processed by CMG-GEM. The dimension of the reservoir model is 1000 ft x 100ft x 80ft. In fact, as shown in Figure 3, the two-dimensional (2D) reservoir model was considered with single injector well and producer well pattern.

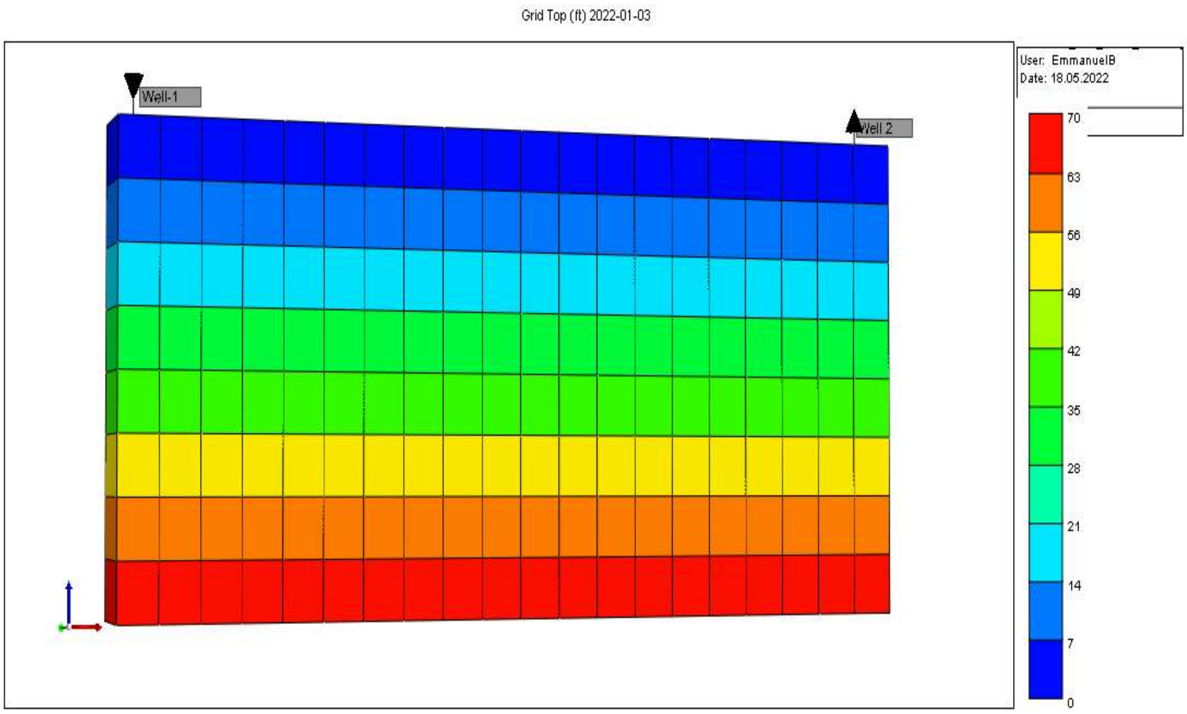

Figure 3. Reservoir model with single injector and producer wells

Reservoir fluids model was built by using the data of composition of reservoir fluids as also published in MOGB publication, 1966 (Mississippi Oil and Gas Board, 1966). The composition of reservoir fluid is shown in Table 2. The two-phase envelope in Figure 4 shows that the crude oil is in two phases (liquid and gas) at initial conditions of 4650 psi and 257 °F.

Table 2. Reservoir Fluid Composition (Mississippi Oil and Gas Board, 1966).

Component	Composition (Mol Fraction)
CO_2	0.0184
CH_4	0.5376
C_2H_6	0.0717
C_3H_8	0.0334
IC_4	0.0104
NC_4	0.0158
IC_5	0.0123
NC_5	0.0095
NC_6	0.0248
C_{7+}	0.2661

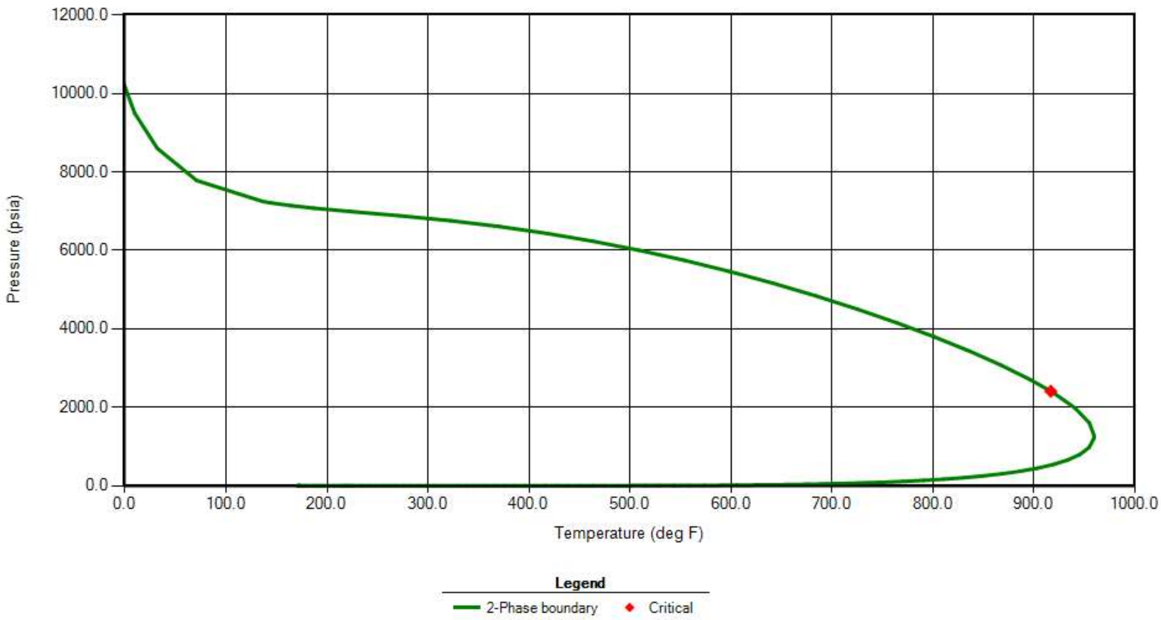

Figure 4. The two-phase envelope for crude oil initially in two phases using Peng-Robinson EOS

The relative permeability data in Table 3 were used for this reservoir and assumed for high salinity waterflooding. Brooks-Corey correlation was then applied to model and produce the oil-water and liquid-gas relative permeability curves.

Table 3. Rock and fluid parameters for relative permeability curves of the base case (Delshad et al., 2013; Hosseini et al., 2013)

Rock-fluid parameters	Values
$\mathbf{k_{rwo}^0}$: $\mathbf{k_{rw}}$ at irreducible oil	0.5
$\mathbf{k_{row}^0}$: $\mathbf{k_{ro}}$ at connate water	0.65
$\mathbf{k_{rgw}^0} = \mathbf{k_{rgo}^0}$: $\mathbf{k_{rg}}$ at connate liquid	0.8
$\mathbf{S_{org}}$: endpoint saturation (residual oil for gas liquid table)	0.15
$\mathbf{S_{wrg}} = \mathbf{S_{wro}}$: endpoint saturation (connate water)	4.0
$\mathbf{S_{orw}}$, endpoint saturation (residual oil for water oil table)	0.2
$\mathbf{S_{grw}} = \mathbf{S_{gro}}$: endpoint saturation (connate gas)	0.075
$\mathbf{n_{1wo}}$: exponent for calculating $\mathbf{k_{rw}}$	4.0
$\mathbf{n_{1wg}} = \mathbf{C_{1og}}$: exponent for calculating $\mathbf{k_{rog}}$	4.0
$\mathbf{n_{1ow}}$: exponent for calculating $\mathbf{k_{row}}$	2.38
$\mathbf{n_{1gw}} = \mathbf{C_{1go}}$: exponent for calculating $\mathbf{k_{rg}}$	2.2

4.2. Geochemical Reactions Modelling

The geochemical reactions were modelled by using the data taken from different literatures. The Cranfield oil reservoir is a Lower Tuscaloosa Formation (LTF) that is locally referred as "D-E sand". The LTF is mainly composed of quartz (79.4%), chlorite (chamosite) (11.8%), kaolinite (3.1%), and illite (1.3%). There is also the presence of soluble and active minerals like calcite (1.1%), dolomite (0.4%), and albite (0.2%). On the other hand, the Tuscaloosa formation brine is a Na-Ca-Cl water type. The average salinity of the formation water is measured as 150000ppm (Total Dissolved Solids, TDS) and its pH is 5.7 (Lu et al., 2012; Soong et al., 2016; Stancliffe and Adams, 1986). Table 4 shows the ionic composition of the formation brine used.

Table 4. Mineral composition of Lower Tuscaloosa Formation brine (Soong et al., 2016)

Ions	**Concentration (ppm)**
Ca^{2+}	11798
Mg^{2+}	1035
Na^{+}	43743
SO_4^{2-}	238
Cl^{-}	92223

The data for synthetic sea water were taken from experimental research by Teklu et al., 2017. Low salinity water was hence modelled by diluting sea water 2 times, 4 times and 5 times (Teklu et al., 2017). The ions concentration of injected sea water and low salinity water are illustrated in Table 5.

Table 5. Concentration of ions of brine and low salinity water used for simulation

Ions	Sea Water (ppm)	LoSal1 (ppm)	Losal2(ppm)	LoSal3(ppm)
Ca^{2+}	691.5	346	173	13.7
Mg^{2+}	3459.0	1729.5	864.9	69.2
Na^{+}	1286.1	6495.1	3247.6	259.8
SO_4^{2-}	4098.8	2049.8	1024.9	82.1
Cl^{-}	30110.6	15058.7	7529.7	602.1
TDS	**51346**	**25679.1**	**12840.1**	**1026.9**

The injection of water with different salinity content to formation brine affects the rock-brine-oil system interfaces equilibrium and causes chemical change in the reservoir. Software packages like WOLERY and PHREEQC were programed for this geochemistry. These databases were therefore used through Process Wizard interface provided in GEM simulator to model the aqueous, mineral, and ion exchange reactions. These chemical reactions are reversible according to ions concentration in injected water.

Aqueous Reactions:

$$\mathrm{CO_2 + H_2O \leftrightarrow H^+ + HCO_3{}^-}$$
$$\mathrm{H^+ + OH^- \leftrightarrow H_2O}$$
$$\mathrm{CaSO_4 \leftrightarrow Ca^{2+} + SO_4{}^{2-}}$$
$$\mathrm{MgSO_4 \leftrightarrow Mg^{2+} + SO_4{}^{2-}}$$
$$\mathrm{NaCl \leftrightarrow Na^+ + Cl^-}$$

Mineral Reactions:

$$\mathrm{CaCO_3 + H^+ \leftrightarrow Ca^{2+} + HCO_3{}^-}$$
$$\mathrm{CaMg(CO_3)_2 + 2H^+ \leftrightarrow Ca^{2+} + Mg^{2+} + HCO_3{}^-}$$

Ion Exchange Reactions:

$$\frac{1}{2}\mathrm{Ca - X_2 + Na^+ \leftrightarrow \frac{1}{2}Ca^{2+} + Na - X}$$
$$\frac{1}{2}\mathrm{Mg - X_2 + Na^+ \leftrightarrow \frac{1}{2}Mg^{2+} + Na - X}$$

In these ion exchange reactions, Na^+ is taken up by the exchanger X on the clay surface. In case of low salinity water injection, multivalent ions like Ca^{2+} and Mg^{2+} dissolute with carboxylate group from the clay surface and exchange with mono-valent ions like Na^+ and K^+.

For these ion exchange reactions on clay surface are measured by equivalent fractions $\zeta(\mathrm{Na-X})$, $\zeta(\mathrm{Ca-X_2})$, and $\zeta(\mathrm{Mg-X_2})$. Therefore, ion exchanges are modelled by selectivity coefficients which are operational variables as shown in Eq. (7) and Eq. (8) (Dang et al., 2013; Dang et al., 2015; Dang et al., 2016; Gaines and Thomas, 1953; CMG-GEM)

$$K'_{\mathrm{Na/Ca}} = \frac{\zeta(\mathrm{Na-X})[m(\mathrm{Ca^{2+}})]^{0.5}}{[\zeta(\mathrm{Ca-X_2})]^{0.5}m(\mathrm{Na^+})} \times \frac{[\gamma(\mathrm{Ca^{2+}})]^{0.5}}{\gamma(\mathrm{Na^+})} \quad (7)$$

$$K'_{\mathrm{Na/Mg}} = \frac{\zeta(\mathrm{Na-X})[m(\mathrm{Mg^{2+}})]^{0.5}}{[\zeta(\mathrm{Mg-X_2})]^{0.5}m(\mathrm{Na^+})} \times \frac{[\gamma(\mathrm{Mg^{2+}})]^{0.5}}{\gamma(\mathrm{Na^+})} \quad (8)$$

Where, m is the ion concentration and γ is the activity coefficient. In GEM, a parameter Cation Exchange Capacity (CEC) was introduced to measure the number of ions adsorbed on clay surface by ion exchange. Hence, the total number of moles of $Na - X$, $Ca - X_2$, and $Mg - X_2$ are calculated for total grid bulk volume (V) as shown in Eq. (9).

$$V\varphi(CEC) = VN_{Na-X} + 2VN_{Ca-X_2} + 2VN_{Mg-X_2} \tag{9}$$

The number of moles of $Na - X$, $Ca - X_2$, and $Mg - X_2$ per grid block are therefore calculated by dividing the bulk volume as indicated in Eq. (10).

$$\varphi(CEC) = N_{Na-X} + 2N_{Ca-X_2} + 2N_{Mg-X_2} \tag{10}$$

Consequently, equivalent fractions are calculated as in the following Eq. (11), Eq. (12) and Eq. (13).

$$\zeta(Na - X) = \frac{N_{Na-X}}{\varphi(CEC)} \tag{11}$$

$$\zeta(Ca - X_2) = \frac{N_{Ca-X_2}}{\varphi(CEC)} \tag{12}$$

$$\zeta(Mg - X_2) = \frac{N_{Mg-X_2}}{\varphi(CEC)} \tag{13}$$

4.3. Wettability Alteration Model

Wettability alteration due to LSWF is modelled by shifting relative permeability curves to water wetting conditions. Normally relative permeability data for simulation are measured through core analysis experiments. However, in this study, relative permeability data are assumed for formation brine and the rock is considered oil wet. Therefore, relative permeability curves for LSWF were obtained by reducing S_{or} from 0.2 to 0.14 but the curvature was not changed as shown in the Figure 5.

From these two sets of relative permeability curves, it is required to perform an interpolation for oil-water relative permeability for different salinity water injections. Relative permeability changes because the adsorption, dissolution, or precipitation that take place during salty water injection. The ion exchange equivalent fraction one of the options provided by GEM was selected for oil water relative permeability curves interpolations. The ion exchange equivalent fraction is preferred because it includes ion exchange as the main mechanism of low salinity waterflooding. It was assumed in this study that if the initial equivalent fraction $\zeta(Ca - X_2)$, is greater than 0.4, the relative permeability curves for high salinity is used and if it is less than 0.19, then those for low salinity are used. The initial equivalent fraction $\zeta(Ca - X_2)$, between 0.4 and 0.19, the interpolation is then performed.

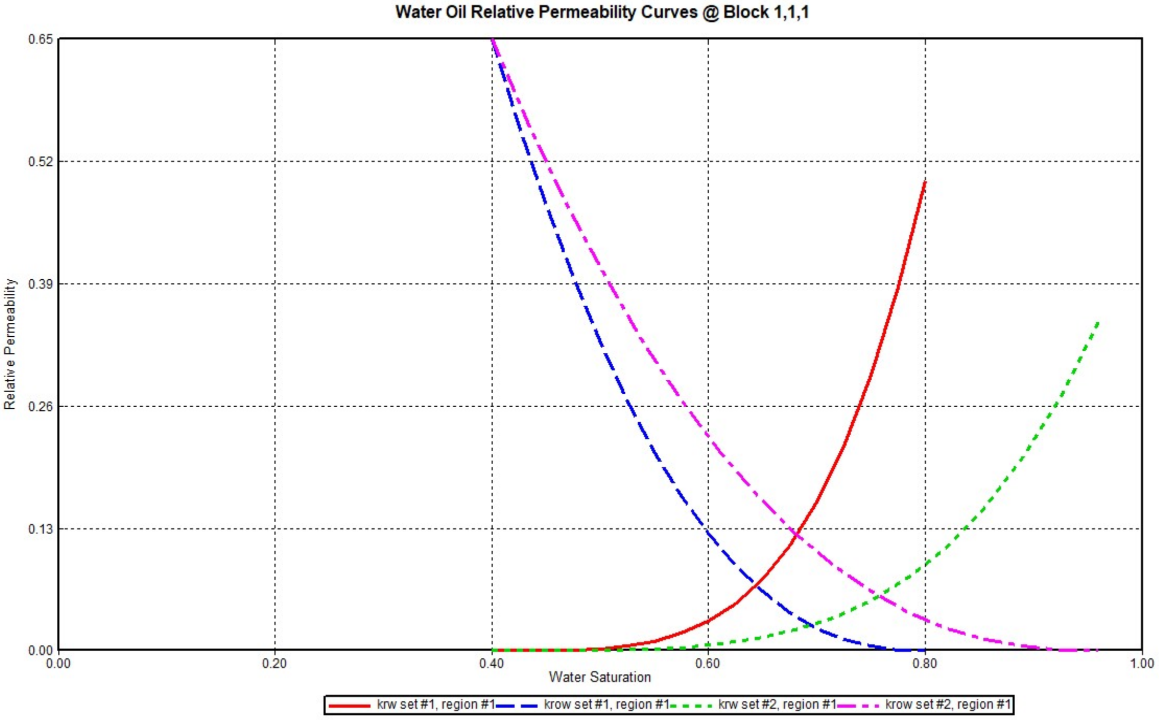

Figure 5. Wettability alteration modeling by shifting relative permeability curves from oil wet to water wet behavior

The Eq. (14) demonstrates how the interpolant for ion exchange is calculated as proposed in these research studies (Egbe et al., 2021; Jerauld et al., 2008; Qiao et al. , 2015).

$$\omega = \frac{\zeta(\mathrm{Ca} - \mathrm{X}_2) - \zeta(\mathrm{Ca} - \mathrm{X}_2)^{\mathrm{HSW}}}{\zeta(\mathrm{Ca} - \mathrm{X}_2)^{\mathrm{LSW}} - \zeta(\mathrm{Ca} - \mathrm{X}_2)^{\mathrm{HSW}}} \tag{14}$$

Relative permeability values can then be calculated by linear interpolation as shown in the following Eq. (15) and Eq. (16).

$$\mathrm{K_{rw}} = \omega \mathrm{K_{rw}^{LSW}} + (1 - \omega)\mathrm{K_{rw}^{HSW}} \tag{15}$$

$$\mathrm{K_{ro}} = \omega \mathrm{K_{ro}^{LSW}} + (1 - \omega)\mathrm{K_{ro}^{HSW}} \tag{16}$$

Where, $\mathrm{K_{rw}}$ and $\mathrm{K_{ro}}$ are water and oil relative permeability for injected brine respectively, $\mathrm{K_{rw}^{HSW}}$ and $\mathrm{K_{ro}^{HSW}}$ are water and oil relative permeability for formation brine respectively, $\mathrm{K_{rw}^{LSW}}$ and $\mathrm{K_{ro}^{LSW}}$ are water and oil relative permeability of low salinity water respectively.

4.4. Waterflooding and CO2 Gas Flooding Modelling

The waterflooding was modelled by using Process Wizard interface in builder that was provided for modelling the processes that involve geochemical changes. The maximum bottom hole pressure of 5500 psi and the maximum surface water rate (SWR) of 100bbl/day were set as the injector well constraints. The CO_2 gas that was already modelled in the components of crude oil was selected as the injected fluid. The maximum bottom hole pressure of 5500 psi was also set as the injector well constraint with surface gas rate (SGR) of 100000 ft^3/day. The producer well constraints for both waterflooding and CO_2 gas flooding were the minimum bottom hole pressure of 4060 psi and the surface oil rate (STO) of 200bbl/day. The simulations were run for 6 years continuously. The parameters in Table 6 were used in order to evaluate and compare the oil sweep efficiencies.

Table 6. Operational parameters for Waterflooding and CO_2 gas injection simulations

Parameters	Waterflooding	CO_2 gas injection
Initial phase of oil	• Two phases (liquid-gas) • Single phase (liquid)	• Two phases (liquid-gas) • Single phase (liquid)
Injection Depth	• All zones • Upper zones	• All zones • Lower zones
Vertical Permeability	• 50 md • 10 md	• 50 md • 10 md

4.5. Conventional WAG and LSWAG Modelling

The typical WAG injection was modelled by injecting both water and CO_2 gas at the same injector well. The injector well was open and shut-in alternately after each six month for 6 years. The figure 6 is the graphical illustration of the WAG model created.

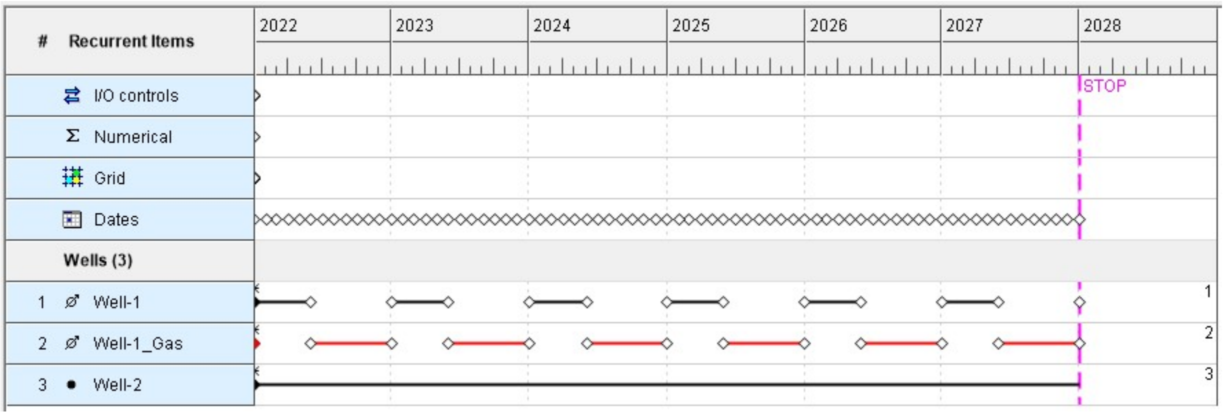

Figure 6. Graphic Model of WAG injection

5. Results and Discussion

5.1. Effect of initial phase of reservoir fluid

The effect of initial phase of crude oil was evaluated by simulation of waterflooding and CO_2 gas injection separately. Due to high mole fraction of methane compared to those of other components, oil was initially found to exist in two phases (liquid and gas) as shown in Figure 4. Mole fraction of oil components was therefore adjusted to create initial single liquid phase by increasing mole fraction of C_{7+} to 0.4661 and decreasing mole fraction of methane to 0.3376.

Figure 7 illustrates the oil recovery factors comparison with oil initially in single phase and two-phases during sea waterflooding and CO_2 gas injection respectively. The oil recovery factor difference is attributed to the fact that gas oil ratio is high for oil initially in two phases during production. In fact, the high gas production with oil initially in two phases influenced the relative permeabilities and caused to obtain less oil recovery percentage.

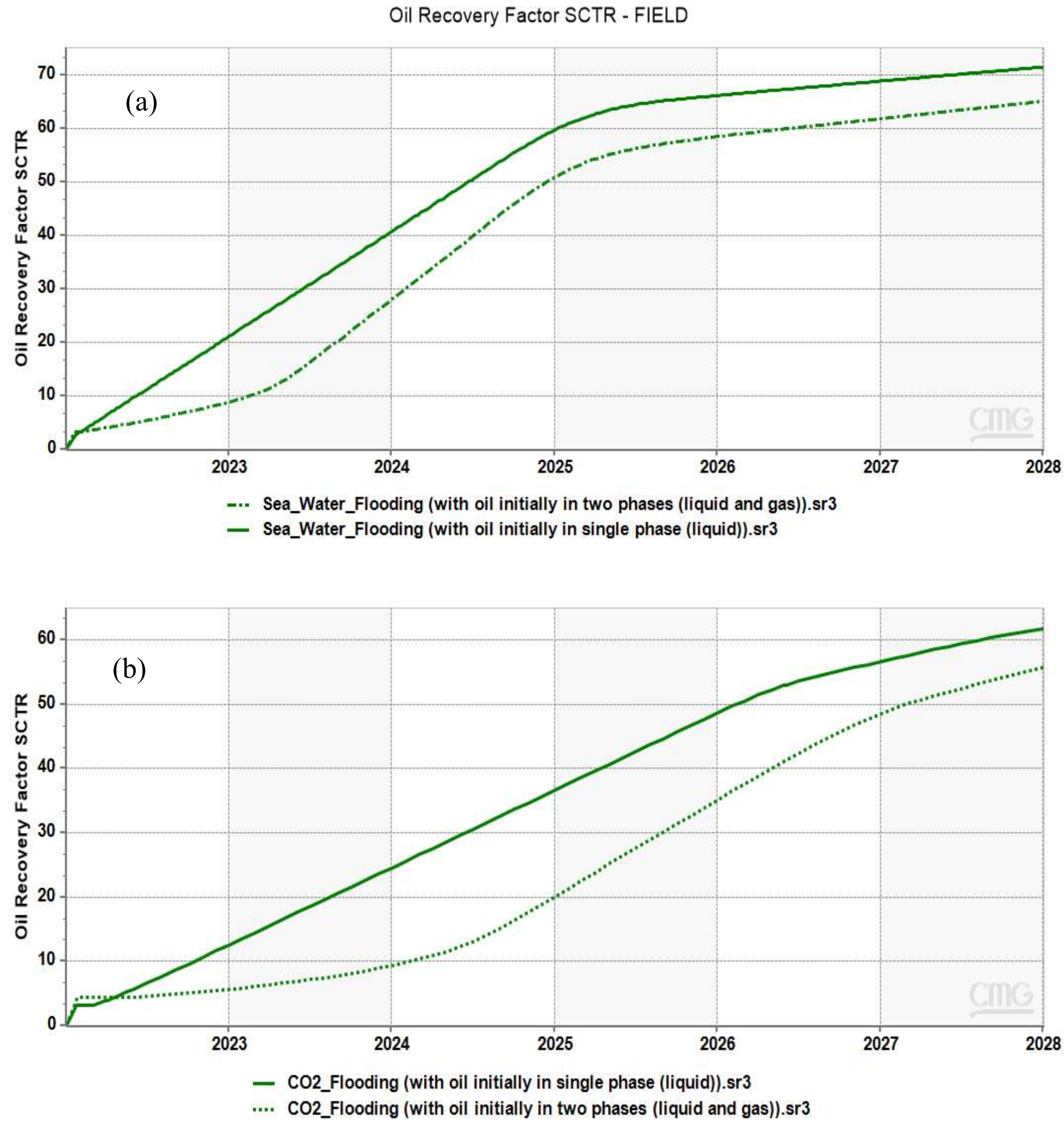

Figure 7. Effect of initial phase of crude oil on oil recovery factor during (a) waterflooding, (b) CO_2 injection

5.2. Gravity Effect

Figure 8 displays the water and gas saturation on the course of continuing waterflooding and CO_2 gas injection respectively. During waterflooding, water displaces oil from side-bottom of the reservoir from injector to the producer well. In fact, due to gravity effect, water flow down at the lower zones of the reservoir because it is denser than oil. The pressure difference also causes water saturation to increase going forward from the injector well to the producer well. In the case of continued CO_2 gas injection, gravity effect also causes the gas to move to the upper zones of the reservoir from injector well to the producer well.

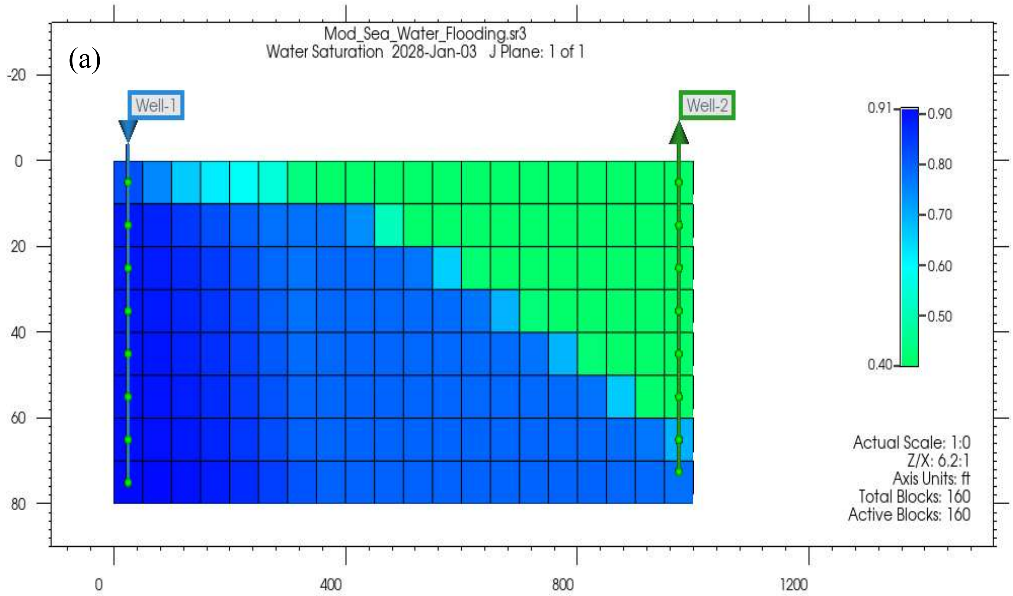

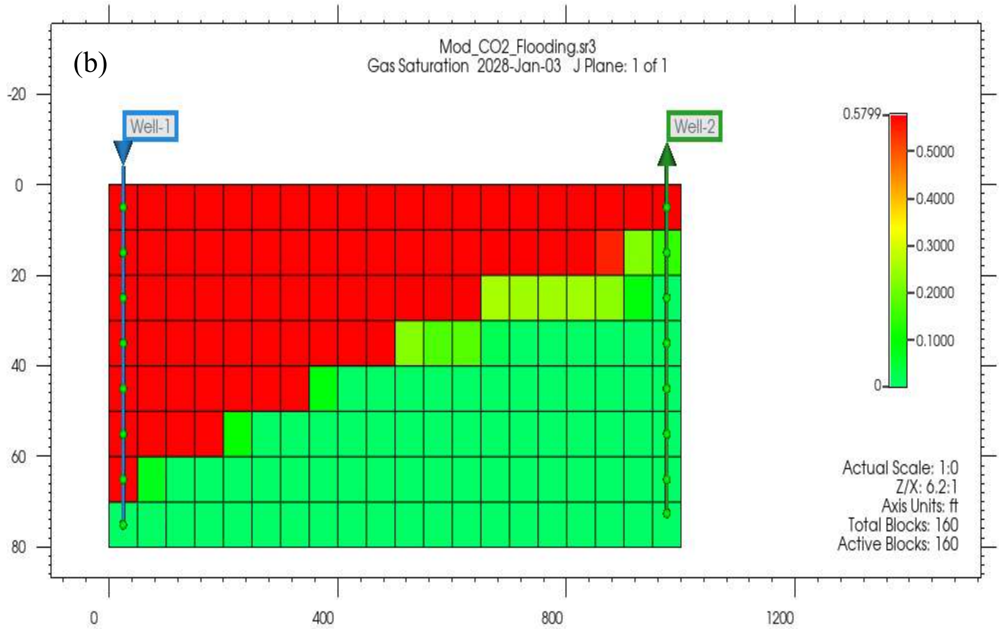

Figure 8. Water saturation during (a) waterflooding, (b) CO_2 gas flooding

5.3. Injection Depth Effect

In order to control the water and gas early breakthrough from lower and upper zones of reservoir respectively, and improve the sweep efficiencies, the adjustment on the injection depth was applied by perforating upper zones for waterflooding and lower zones for gas injection. It was deemed to be of importance to inject water from upper zones to increase the volumetric sweep efficiency by retarding the water breakthrough while favoring the horizontal front displacement of water in upper zones of the reservoir. The graphs in Figure 9 display the comparison between front displacement of water when injected from upper zones and when injected from all zones.

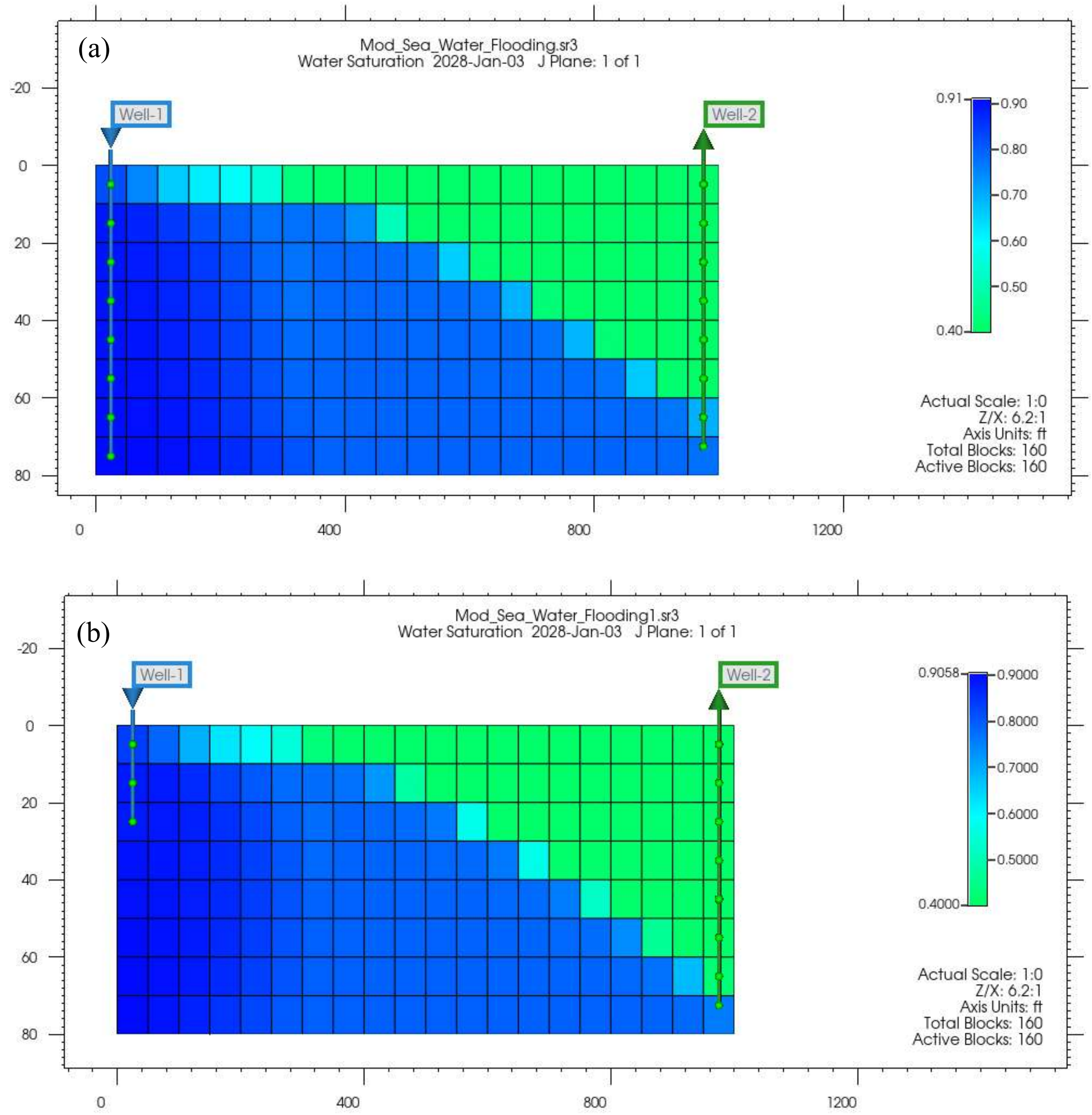

Figure 9. Water saturation profile during waterflooding from (a) all zones, (b) upper zones

On the other hand gas was injected from lower zones of the reservoir to allow gas to contact with oil at the lower and middle zones of the reservoir and eventually prevent early gas breakthrough at the upper zones of the reservoir. Figure 10 below shows the positive impact of injecting gas through perforations in the lower zones; there is an increased region contacted with gas and hence increased the oil sweep efficiency.

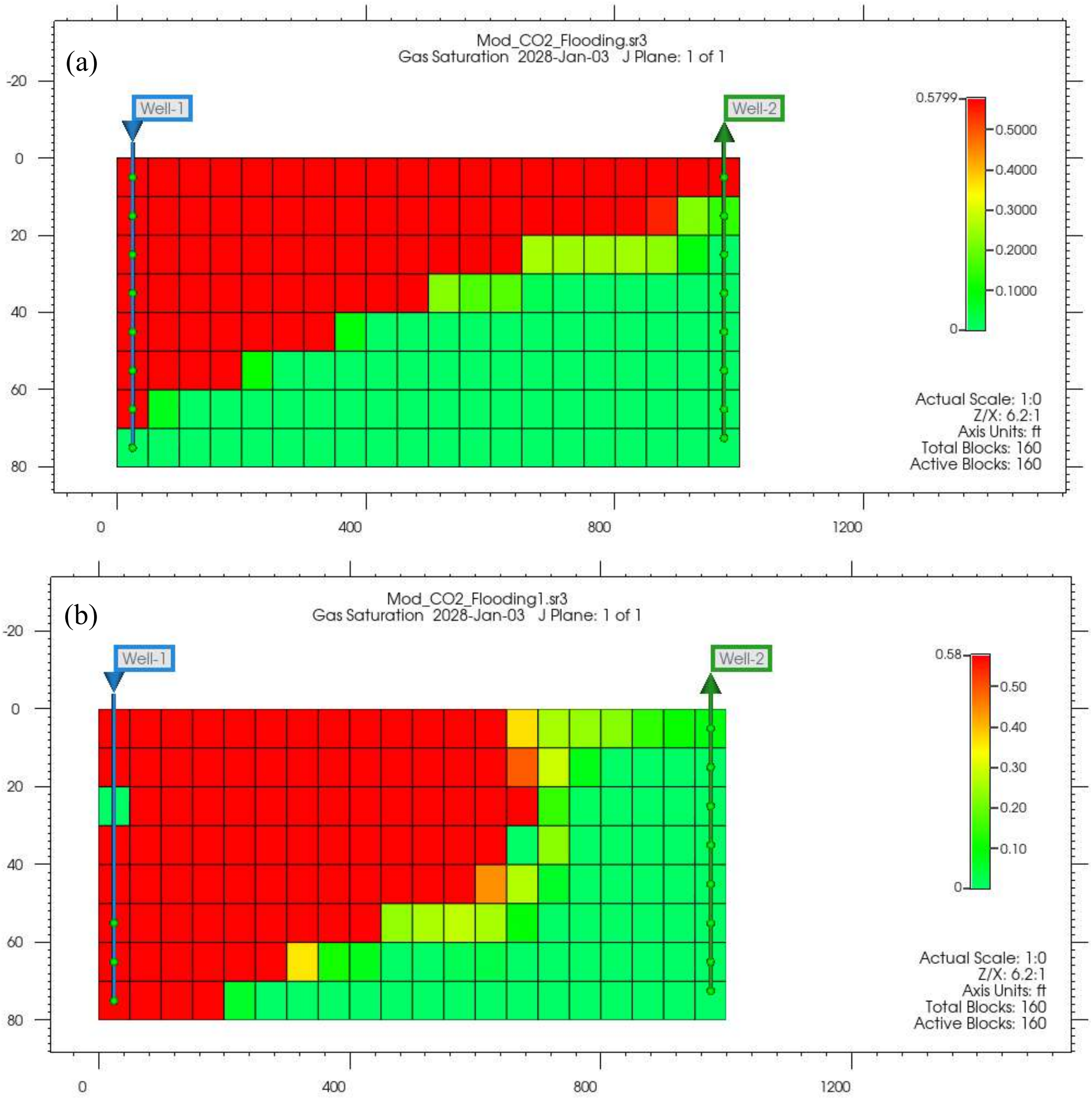

Figure 10. Gas saturation profile during gas injection from (a) all zones, (b) lower zones

5.4. Effect of Vertical to Horizontal Permeability Ratio

Vertical permeability controls vertical flow of reservoir fluids as well as the injected fluid. The effect of the ratio of vertical to horizontal permeability was therefore evaluated through simulation results. The simulation results of waterflooding and CO_2 gas injection with constant horizontal permeability (50md) and different vertical permeability (50 md and 10 md) are reported through water and gas saturation profiles. From Figure 11, with low vertical permeability (10 md) there is an increase of volumetric sweep efficiency of water displacing oil during waterflooding. In fact, volumetric sweep efficiency is increased with low vertical to horizontal permeability ratio because water injected from the upper zones can relatively flow horizontally.

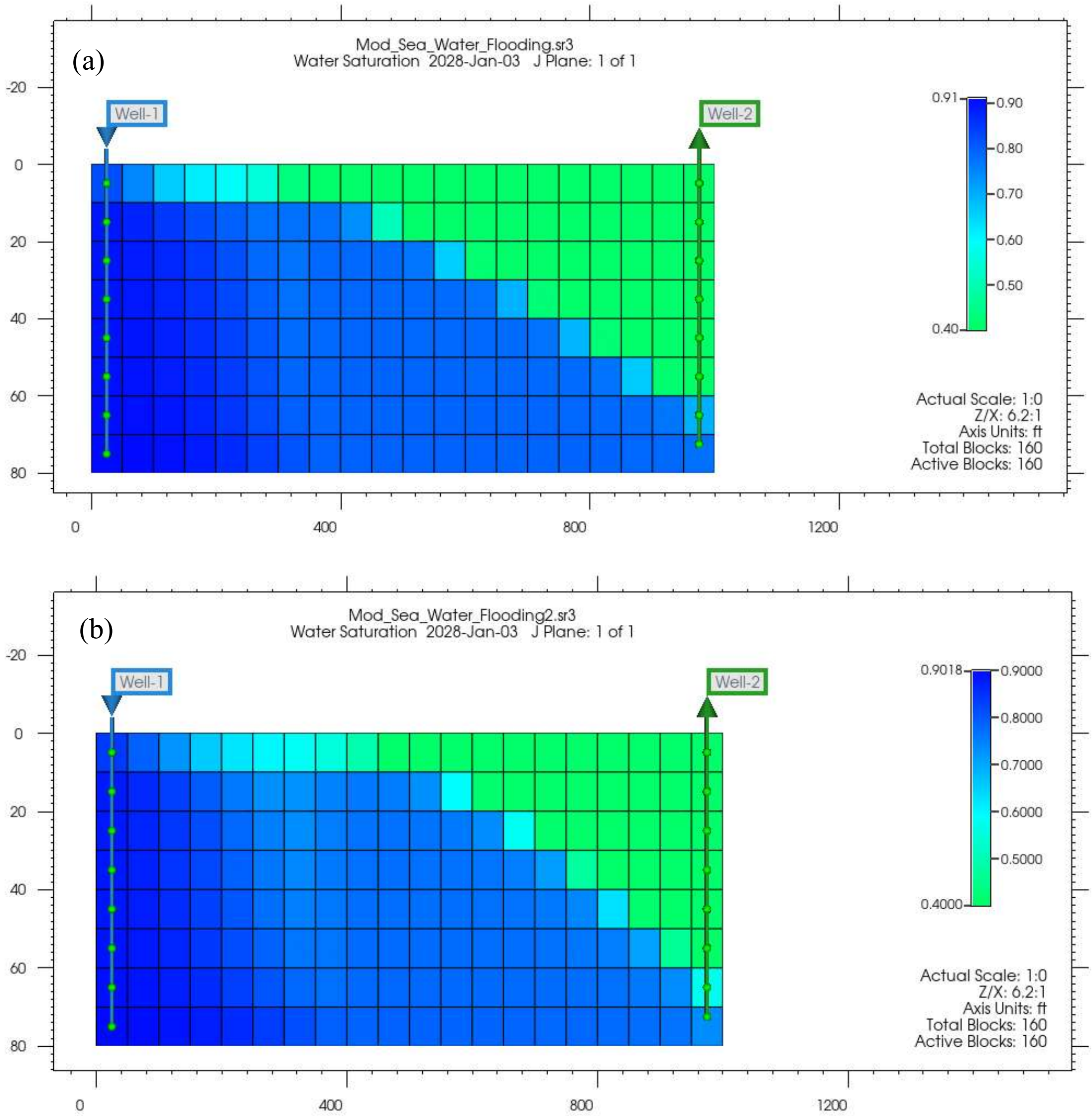

Figure 11: Water saturation during waterflooding with vertical permeability of (a) 50 md and (b) 10 md

In Figure 12, lowering the vertical permeability increases the frontal displacement of oil by gas injection in lower and middle zones of the reservoir while also controlling the early gas break through from the upper zones of the reservoir.

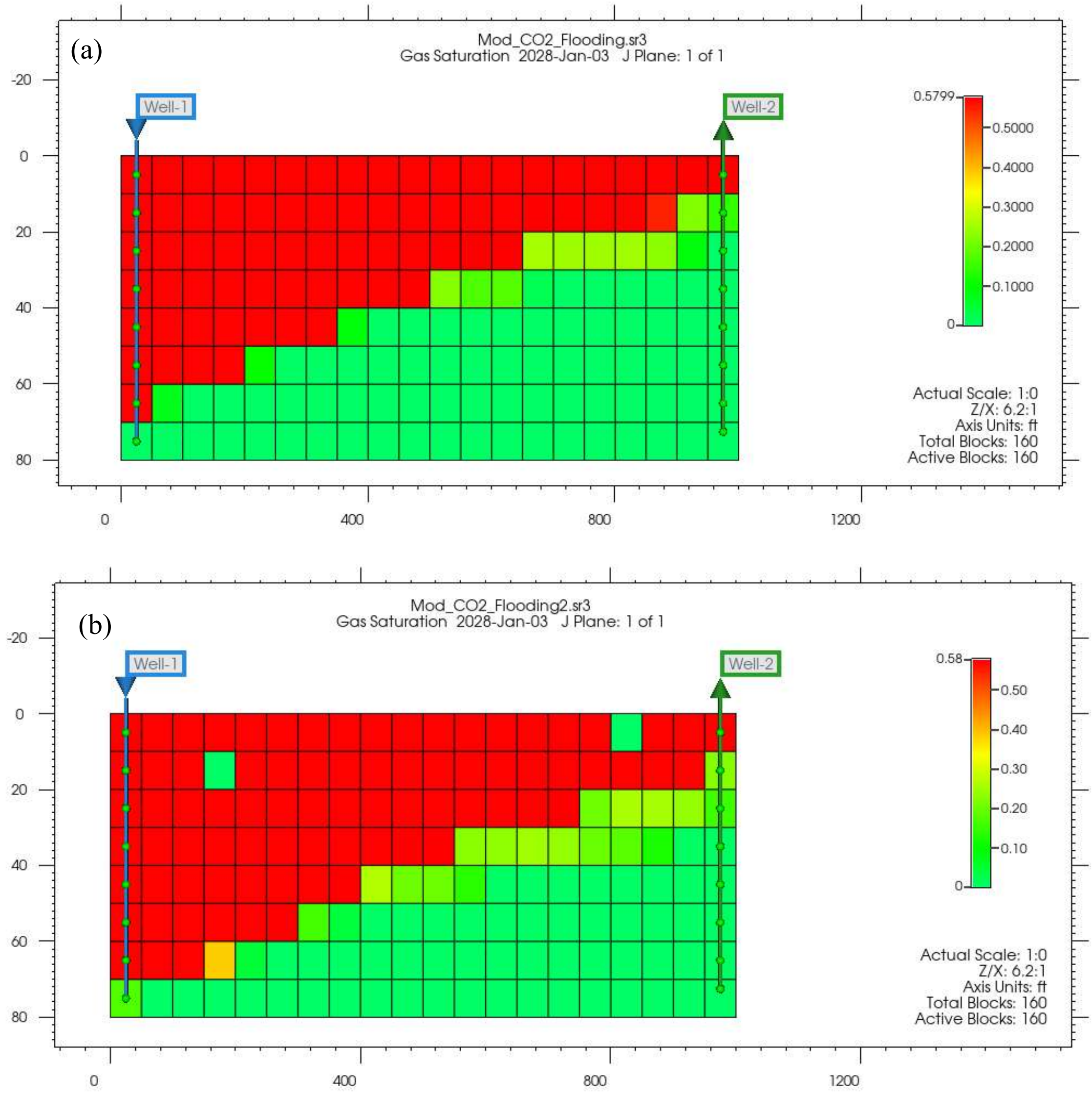

Figure 12. Gas saturation during CO_2 gas injection with vertical permeability of (a) 50 md and (b) 10 md

5.5. Conventional WAG injection

In both cases of separate waterflooding and CO_2 gas injection, there are eventually water and gas breakthrough from lower and upper zones of the reservoir respectively while there remains a sizable region un-swept. It is therefore for this reason that the combination of water and gas was proposed and applied to produce the attic oil that remains in the case of only waterflooding and oil in lower zones in the case of only gas injection. After analysis of effects of gravity, initial oil phase, injection depth, and vertical to horizontal permeability ratio on individual waterflooding and CO_2 gas injection; the favorable conditions were applied for WAG injection simulation.

The initial single phase of oil was considered as it produced higher oil recovery percentage. The gravity effect during WAG injection is the most obvious because of density differences between water, oil, and gas. The waterflooding from the upper zones and CO_2 gas injection from the lower zones of the reservoir was also applied. In addition, the vertical permeability of 10 md and horizontal permeability of 50 md were used for WAG injection. As results, it is shown in Figure 13 that the combination of water and gas is more efficient for increasing the sweep area and consequently increases the oil recovery.

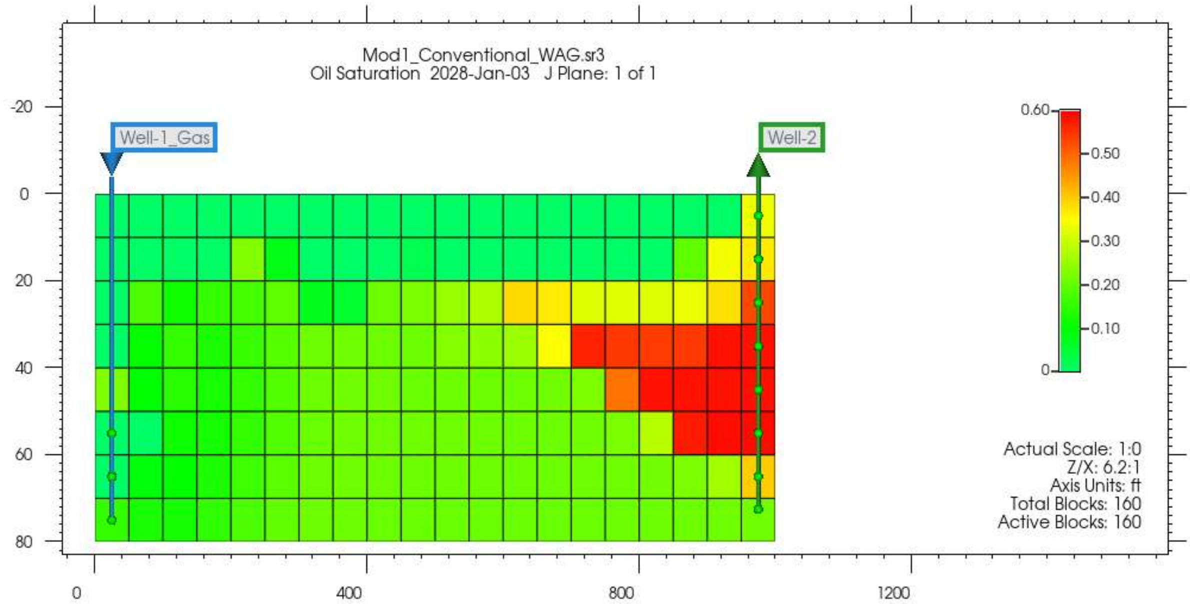

Figure 13. Frontal displacement of oil during WAG injection

Figure 14 shows the comparison of oil recovery factor for waterflooding, CO_2 gas injection and conventional WAG injection. The WAG injection increased oil recovery factor by about 10% from individual waterflooding and CO_2 gas injection. This result is explained by the fact that the combination of water and gas improves both macroscopic oil sweep and oil displacement efficiencies respectively. In fact, water displace oil from side-bottom and hence improve the macroscopic oil sweep efficiency. On the other hand, the CO_2 gas increases oil mobility by reducing its viscosity and hence it improves the oil displacement efficiency.

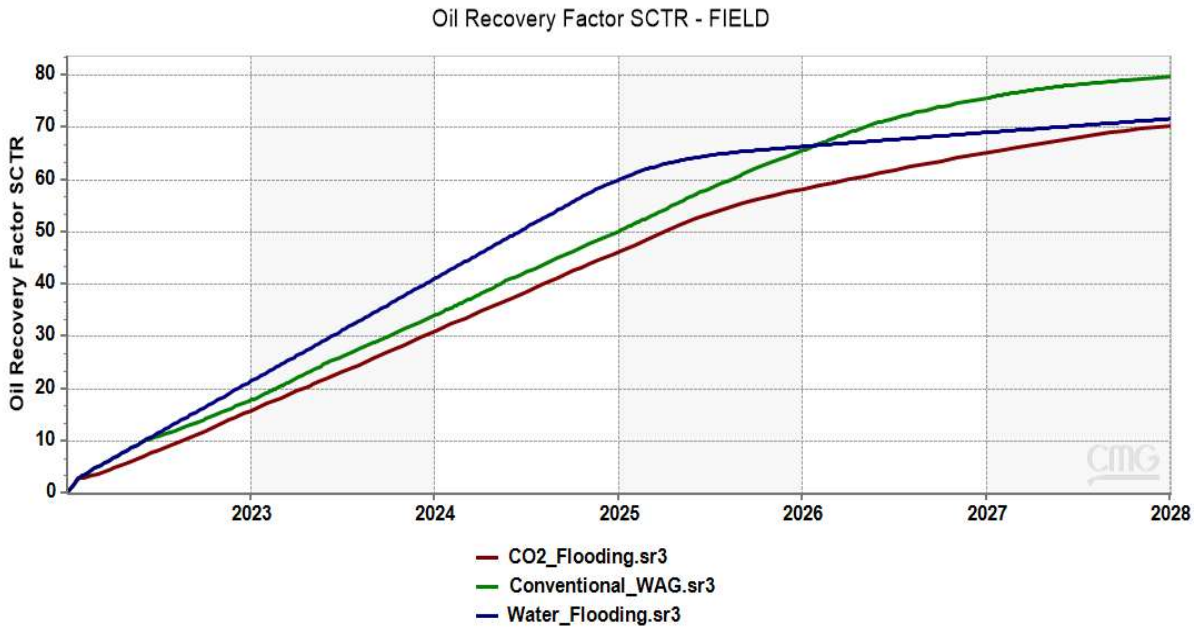

Figure 14. Advantage of WAG injection over continued waterflooding and CO_2 gas injection

5.6. Low Salinity Waterflooding (LSWF)

The effect of salinity of injected water was also evaluated through the results from a series of waterflooding by tunning its salinity. From the simulation results of different waterflooding scenarios as shown in Figure 15, there is an increase of about 8% of oil recovery factor from simulation with sea water of 51346ppm to simulation with low salinity of 1026.9ppm. In addition, the results show that low salinity and completely deionized waterflooding provide the same oil recovery factor. It means that the necessary dissolution of clay minerals for optimum oil recovery is achieved with low salinity of 1026.9ppm.

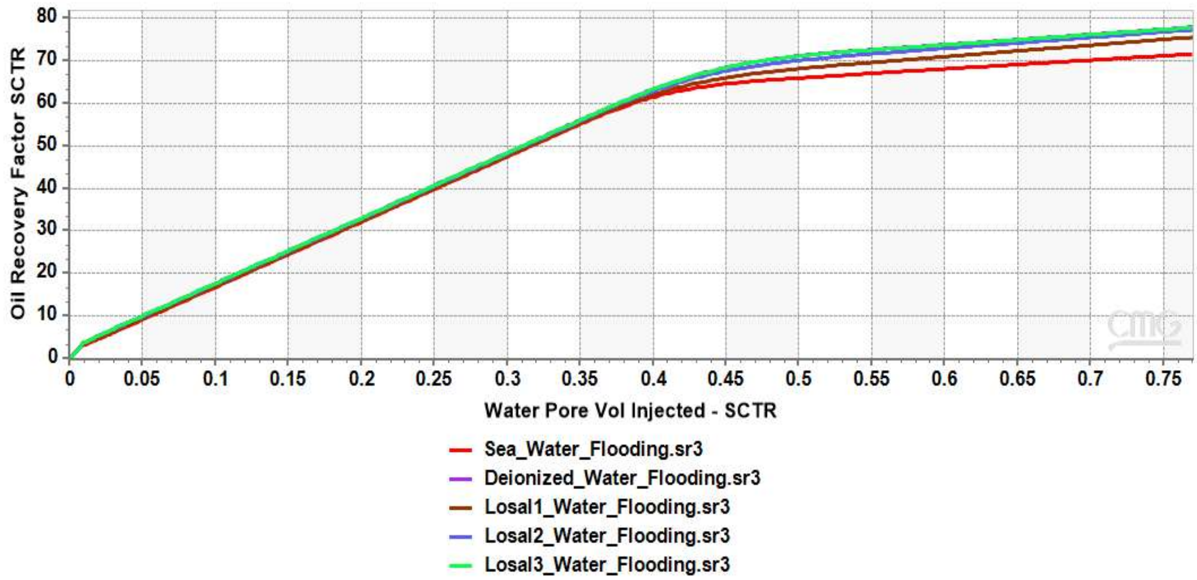

Figure 15. Oil recovery factor from different simulation scenarios of low salinity waterflooding

This increase of oil recovery factor by decreasing water salinity is attributed to the multi-ion exchange and mineral reactions that take place when low salinity water is injected into the rock containing clay minerals. There is wettability alteration from oil wet to preferred water wet when low salinity water is injected. In fact, the multi-ion exchange and wettability alteration are the two main mechanisms that oil is freed from pores and displaced by water in the case of LSWF. In addition, low salinity waterflooding increases oil recovery by breaking the rock-brine-oil interfacial tension. So, there is dissolution of rock minerals like calcite and dolomite which respectively release Ca^{2+} and Mg^{2+} with carboxyl complex in a multi-ion exchange during low salinity waterflooding.

On contrary, high salinity waterflooding results no wettability change instead there is more of ion adsorption. The adsorption of divalent ions like Ca^{2+} on clay surface creates a strong interfacial tension between oil and clay surface.

5.7. Conventional WAG vs LSWAG

The combination of waterflooding and gas injection while also focusing on the effect of salinity content in injected water was evaluated and the performances of conventional WAG and LSWAG injections were compared. The simulations results of conventional and LSWAG injections showed that the combination of waterflooding from upper zones and CO_2 gas injection from lower zones of the reservoir, and reducing vertical to horizontal permeability ratio improves significantly the total sweep efficiency. The contribution of CO_2 gas injection in improving the oil displacement was observed for both conventional WAG and LSWAG injections. The waterflooding contributed on improving the volumetric sweep efficiency in both cases but low salinity content in LSWAG injection particularly increases microscopic sweep efficiency due to multi-ion exchange. In other words, the increase of oil recovery factor by LSWAG injection is mainly attributed to multi-ion exchange and wettability alteration processes that take place during low salinity waterflooding. From the graphs in Figure 16, LSWAG injection produced higher oil recovery factor up to 6% more than sea water or conventional WAG after 6 years.

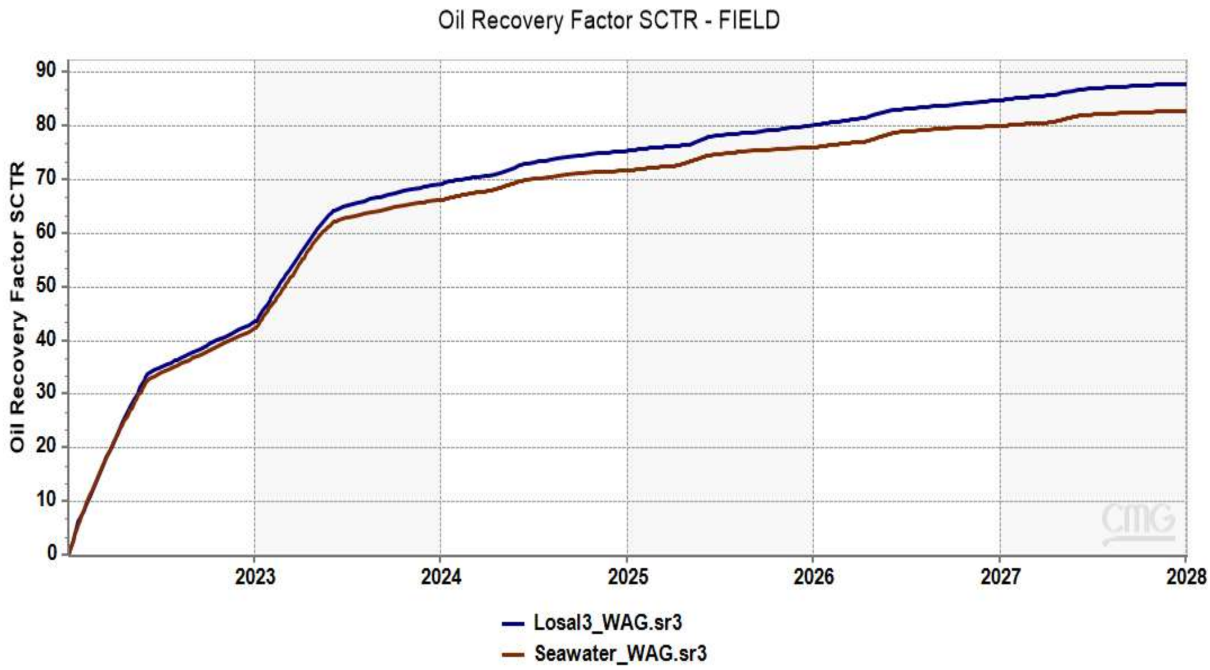

Figure 16. Comparisons of oil recovery factor from conventional WAG and LSWAG with maximum oil flow rate of 500bbl/day.

6. Conclusions

The effect of initial phase of crude oil, gravity, injection depth, and vertical permeability were considered and adjusted to minimize water and gas breakthrough while improving oil recovery factor during waterflooding, CO_2 gas flooding and WAG injection. The application of conventional WAG injection and LSWF individually was a success in improving oil recovery. However, this study showed that the combination or hybrid of the two methods improve further oil recovery for a typical sandstone reservoir. The effect of LSWF on releasing and displacing oil from pore surfaces is described through different mechanisms mainly wettability alteration and multi-ion exchange.

A series of simulation runs of different scenarios of waterflooding, CO_2 gas flooding, and WAG injection were performed by using CMG-GEM simulator. After the results were discussed and analyzed; the following conclusions were drawn:

1. The conventional WAG injection is the combination mechanism of waterflooding and gas injection that was invented to improve individual method of oil recovery. During WAG process, the oil sweep efficiency increases from individual waterflooding and gas injection, and as a result oil recovery factor increases. In this study, an increase of about 10% of oil recovery factor by conventional WAG injection to continued classical waterflooding and CO_2 gas injection was observed.

2. The oil recovery factor is higher with oil initially in single phase (liquid) than in two phases (liquid-gas) due to high gas to oil ratio for oil initially in two liquid-gas phases.
3. The waterflooding from upper zones and gas injection from lower zones of reservoir increase oil sweep efficiency and also prevent early breakthrough of injected fluids.
4. The low vertical to horizontal permeability ratio while injecting gas from lower zones and water from upper zones increases further the sweep efficiency as horizontal flow of water in upper layers and gas in lower layers respectively improve.
5. The water salinity effect was observed while comparing oil recovery factors from simulations of conventional WAG and LSWAG. There is up to about 6% increase of oil recovery factor from conventional WAG with sea water with salinity of 51,346 ppm to LSWAG with diluted sea water with salinity of 1027ppm.

Authors Statement

The authors confirm contribution to the paper as follows: study conception and design: Emmanuel Bucyanayandi, Muhammed Said Ergül, Ibrahim Kocabaş; data collection, analysis and interpretation of results: Emmanuel Bucyanayandi; draft manuscript preparation: Emmanuel Bucyanayandi, Ibrahim Kocabaş. All authors reviewed the results and approved the final version of the manuscript.

Conflict of Interest

The authors declare no conflict of interest.

References

Alpak, F. O., Lake, L. W., and Embid, S. M. (1999), "Validation of a Modified Carman-Kozeny Equation To Model Two-Phase Relative Permeabilities," *SPE Annual Technical Conference and Exhibition*, Houston, Texas.

Behrenbruch, P., & Goda, H. M. (2006), "Two-Phase Relative Permeability Prediction: A Comparison of the Modified Brooks-Corey Methodology with a New Carman-Kozeny Based Flow Formulation," *Proceedings - SPE Asia Pacific Oil and Gas Conference and Exhibition 2006: Thriving on Volatility*, 2, 810–827.

Bernard, G. G. (1967), "Effect of Floodwater Salinity on Recovery Of Oil from Cores Containing Clays," *38th Annual Calfornia Regional Meeting of the Society of Petroleum Engineeers*, California, USA.

Bonder P. (2010), "EOR-the time is now: Its contribution of world energy supply," *Society of Petroleum Engineers, Distinguished Lecturer Program*.

Brooks, R. H., & Corey, A. T. (1964), "Hydraulic properties of porous media," *Hydrology Papers*, 3, 1–37.

Buckley, J. S., Takamura, K., & Morrow, N. R. (1989), "Influence of Electrical Surface Charges on the Wetting Properties of Crude Oils," *SPE Reservoir Engineering*, 4(03), 332–340.

Dang, C. T. Q., Nghiem, L. X., Chen, Z., & Nguyen, Q. P. (2013), "Modeling Low Salinity Waterflooding: Ion Exchange, Geochemistry and Wettability Alteration," *Proceedings - SPE Annual Technical Conference and Exhibition*, 6, 4302–4323.

Dang, C., Nghiem, L. X, Nguyen, N., Chen, Z., & Nguyen, Q. P. (2015), "Modeling and Optimization of Low Salinity Waterflood," *Society of Petroleum Engineers - SPE Reservoir Simulation Symposium 2015*, 1, 55–73.

Dang, C., Nghiem, L. X, Nguyen, N., Chen, Z., & Nguyen, Q. P. (2016), "Mechanistic Modeling of Low Salinity Water Flooding," *Journal of Petroleum Science and Engineering*, 146, 191–209.

Delshad, M., Kong, X., Tavakoli, R., Hosseini, S. A., & Wheeler, M. F. (2013), "Modeling and Simulation of Carbon Sequestration at Cranfield Incorporating New Physical Models," *International Journal of Greenhouse Gas Control*, 18, 463–473.

Egbe, D. I. O., Jahanbani Ghahfarokhi, A., Nait Amar, M., & Torsæter, O. (2021), "Application of Low-Salinity Waterflooding in Carbonate Cores: A Geochemical Modeling Study," *Natural Resources Research*, 30(1), 519–542.

Gaines, G. L., & Thomas, H. C. (1953), "Adsorption Studies on Clay Minerals. II. A Formulation of The Thermodynamics of Exchange Adsorption," *The Journal of Chemical Physics*, 21(4), 714–718.

Hamouda, A. A., & Valderhaug, O. M. (2014), "Investigating Enhanced Oil Recovery from Sandstone by Low-Salinity Water and Fluid/Rock Interaction," *Energy and Fuels*, 28(2), 898–908.

Hosseini, S. A., Lashgari, H., Choi, J. W., Nicot, J. P., Lu, J., & Hovorka, S. D. (2013), "Static and Dynamic Reservoir Modeling for Geological CO2 Sequestration at Cranfield, Mississippi, U.S.A.," *International Journal of Greenhouse Gas Control*, 18, 449–462.

Hovorka, S. D., Choi, J. W., Meckel, T. A., Trevino, R. H., Zeng, H., Kordi, M., and Nicot, J. P. (2008), "Comparing Carbon Sequestration in an Oil Reservoir to Sequestration in a Brine Formation—Field Study," *9th International Conference on Greenhouse Gas Control Technologies (GHGT-9)*, 1(1). Washington, D.C.

Hustad, O. S., & Holt, T. (1992), "Gravity Stable Displacement of Oil by Hydrocarbon Gas After Waterflooding," *Eighth Symposium on Enhanced Oil Recovery, Tulsa: Society of Petroleum Engineers (SPE).*

Jerauld, G. R., Lin, C. Y., Webb, K. J., & Seccombe, J. C. (2008), "Modeling Low-Salinity Waterflooding," *SPE Reservoir Evaluation & Engineering*, 11(06), 1000–1012.

Knappskog, O. A. (2012), "Evaluation of WAG injection at Ekofisk," M.Sc. Thesis, *University of Stavanger*, Norway.

Lu, J., Kharaka, Y. K., Thordsen, J. J., Horita, J., Karamalidis, A., Griffith, C., and Hovorka, S. D. (2012), "CO2–Rock–Brine Interactions in Lower Tuscaloosa Formation at Cranfield CO2 Sequestration Site, Mississippi, U.S.A.," *Chemical Geology*, 291, 269–277.

McGuire, P. L., Chatham, J. R., Paskvan, F. K., Sommer, D. M., & Carini, F. H. (2005), "Low Salinity Oil Recovery: An Exciting New EOR Opportunity for Alaska's North Slope," *SPE Western Regional Meeting, Proceedings*, 439–453.

Mississippi Oil and Gas Board (1966), Cranfield Field, Cranfield Unit, basal Tuscaloosa Reservoir, Adams and Franklin Counties. Jackson Mississippi.

Modelling of Low Salinity Water Flooding using STARS and GEM | Computer Modelling Group Ltd. (n.d.). Retrieved June 24, 2022, from https://www.cmgl.ca/training/modelling-low-salinity-water-flood.

Muggeridge, A., Cockin, A., Webb, K., Frampton, H., Collins, I., Moulds, T., & Salino, P. (2014), "Recovery Rates, Enhanced Oil Recovery and Technological Limits," *Philosophical Transactions of the Royal Society A: Mathematical, Physical and Engineering Sciences*, 372.

Qiao, C., Li, L., Johns, R. T., & Xu, J. (2015), "A Mechanistic Model for Wettability Alteration by Chemically Tuned Waterflooding in Carbonate Reservoirs," *SPE Journal*, 20(4), 767–783.

Soong, Y., Howard, B. H., Dilmore, R. M., Haljasmaa, I., Crandall, D. M., Zhang, L., and Mclendon, T. R. (2016), "CO2/Brine/Rock Interactions in Lower Tuscaloosa Formation," *Greenhouse Gases: Science and Technology*, 6(6), 824–837.

Srisuriyachai, F., & Muchalintamolee, N. (2014), "Cation Interference in Low Salinity Water Injection in Sandstone Formation," *76th European Association of Geoscientists and Engineers Conference and Exhibition 2014: Experience the Energy - Incorporating SPE EUROPEC 2014*, 2014(1), 3565–3569.

Stancliffe, J. R., & Adams, R. E. (1986), "Lower Tuscaloosa Fluvial Channel Styles at Liberty Field, Amite County, Mississippi," *Gulf Coast Association of Geological Societies Transactions*, 36, 305–313.

Tang, G. Q., & Morrow, N. R. (1999), "Influence of Brine Composition and Fines Migration on Crude Oil/Brine/Rock Interactions and Oil Recovery," *Journal of Petroleum Science and Engineering*, 24(2–4), 99–111.

Teklu, T. W., Alameri, W., Kazemi, H., Graves, R. M., and AlSumaiti, A. M. (2017), "Low Salinity Water–Surfactant–CO2 EOR," *Petroleum*, 3(3), 309–320.

Touray, S. T. (2013), "Effect of Water Alternating Gas Injection on Ultimate Oil Recovery," M.Sc. Thesis, *Dalhousie University*, Halifax, Nova Scotia, Canada.

Zitha, P., Felder, R., Zornes, D., Brown, K., and Mohanty, K. (2011), "Increasing Hydrocarbon Recovery Factors," *Society of Petroleum Engineers*.

Scientific Research Communications

Research Article

Sci. Res. Comm. (2023)
Volume 3, Issue 1
doi: 10.52460/src.2023.004

A Novel Wastewater Load Allocation Approach for River Basins Using Simulation-Optimization Models

Derya Sadak[1] **M. Tamer Ayvaz**[2,*] **Alper Elçi**[3] **Mehmet Dilaver**[4] **Selma Ayaz**[4]

[1] Department of Water Management, Delft University of Technology, Delft, Netherlands
[2] Department of Civil Engineering, Pamukkale University, Denizli, Turkiye.
[3] Department of Environmental Engineering, Dokuz Eylul University, Izmir, Turkiye.
[4] Marmara Research Center, Kocaeli, Turkiye.

[*] Corresponding author: tayvaz@pau.edu.tr

Received: 31.10.2022 Accepted: 29.01.2023

Abstract

In this study, a new wastewater load allocation approach using a linked simulation-optimization model is proposed to determine the receiving body-based discharge limits by considering the discharge standards used by the European Union Water Framework Directive. By using the proposed approach, wastewater loads of point sources can be determined in such a way that the parameters exceeding the water quality targets (WQT) in receiving water bodies meet the relevant WQT. The simulation part is used to determine pollutant concentrations throughout the river system using the AQUATOX water quality simulation model. However, since AQUATOX is an independent simulation model and its source code is not publicly available, it is not possible to execute it with the optimization model for the generated load combinations. Therefore, a concentration-response matrix (CRM) is developed as a surrogate water simulation model by using the outputs of the AQUATOX model. After this process, the developed CRM is integrated into an optimization model where the heuristic differential evolution (DE) optimization approach is used. The performance of the proposed simulation-optimization approach is evaluated on a sub-watershed of the Kucuk Menderes River Basin by considering different waste load allocation scenarios for the $CBOD_5$ water quality parameter. The results showed that the proposed simulation-optimization approach can effectively allocate the wastewater loads among different point sources by considering the WQT values of the $CBOD_5$ parameter.

Keywords: Wastewater; load allocation; simulation-optimization

1. Introduction

Wastewater load allocation (WLA) is an important component of water quality management and plays a key role to obtain satisfactory water quality in river basins. Treated and untreated wastewater discharges contribute to the deterioration of river water quality, which can cause lethal effects on aquatic life. Therefore, a considerable number of published studies exist on solutions to control wastewater discharge loads and increase water quality through water resources planning and management (Boose, 2002; Jia and Culver, 2006; Deng et al., 2010; Su et al., 2018; Afshar et al, 2018). These studies generally use trial-and-error based approaches to meet the relevant water quality standards; however, it is not practical to obtain solutions for multiple pollutant sources (Boose, 2002). Recently, most WLA studies have only been carried out to determine the quantity of reducing pollution levels at the sources by simulation-optimization model until obtaining satisfactory water quality and maximum discharge load considering the economic efficiency of production facilities (Burn and Yulianti, 2001; Cho et al., 2004; Jia and Culver, 2006; Deng et al., 2010; Zou et al., 2010, Han et al., 2011; Afshar and Masaumi, 2016; Afshar et al., 2018; Saadatpour et al., 2019; Su et al., 2019). Thus, many studies involving simulation-optimization models can be found in the scientific literature. Among them, Deininger (1965) first employed simulation-optimization models where linear programming based deterministic optimization approach was used to improve the water quality by considering the dissolved oxygen concentration in the river system. Similarly, Revelle et al. (1968) used linear programming to obtain pollutant loads that result in satisfactory water quality in river system. On the other hand, Liebman and Lynn (1966) and Klemetson and Grenny (1985) used dynamic programming to minimize wastewater management costs.

Note that in the conducted studies, the water quality processes in river systems were simulated with different simulation models such as QUAL2E (Burn and Yulianti, 2001; Parmar and Keshari, 2014; Saadatpour and Afshar, 2007), QUAL2K (Saadatpour et al., 2019), CE-QUAL (Afshar et al., 2018), WASP4(Cardwell and Ellis, 1993), etc. These water quality simulation models have been combined with both heuristic and deterministic optimization approaches. In those approaches, pollutant loads were equally allocated (equality approach) among the point sources, no matter which simulation and optimization models are used (Burn and Yulianti, 2001; Cho et al., 2004; Afshar and Masaumi, 2016; Afshar et al., 2018; Saadatpour et al., 2019). Although this equity approach seems quite reasonable for points sources with similar characteristics, it may not be reasonable to allocate the same pollutant loads to sources that have different characteristics and capacities. In 2020, an unequally load allocation approach have been suggested to overcome with this problem in the literature and this approach have been used with deterministic GRG optimization technique (Sadak et al., 2020).

In this study, a novel simulation-optimization approach is proposed for allocating the wastewater discharge loads considering water quality targets (WQTs). In contrast to most previous studies, waste loads are allocated among point sources by assigning different allocation weights for each source. In the simulation part of the proposed approach, carbonaceous biochemical oxygen demand ($CBOD_5$) is considered the main water quality parameter, and the AQUATOX (Park et al., 2008) model is used to simulate the fate and transport of this parameter in the river system. It should be noted that the water quality model should be executed separately in an iterative fashion for each scenario that was generated by the optimization model. However, AQUATOX is an independent simulation model, and it cannot be executed directly from the optimization model for the generated load allocation scenarios. Therefore, a concentration-response-matrix approach (CRM) is developed that is based on the resulting concentration of the discharged pollutant in the river. CRM is basically a surrogate water quality model that provides the change in pollutant concentration in the river for unit load discharges. The surrogate water quality model approach based on CRM was originally developed to solve groundwater problems by Gorelick (1982a, 1982b), but Su et al. (2019) and Sadak et al. (2020, 2022) have used it to solve surface water quality problems. This developed CRM-based surrogate model is then combined with a heuristic optimization model where the DE optimization approach is used. The performance of the proposed simulation-optimization approach is evaluated on a sub-watershed of the Kucuk Menderes River Basin by considering different waste load allocation scenarios. The identified results indicated that the proposed simulation-optimization model can successfully allocate the pollutant loads by considering different load allocation weights.

2. Problem Definition

The problem of waste load allocation by means of the proposed simulation-optimization approach can be defined by the conceptual example given in Figure 1, where concentration curves are intended to show just increases in concentrations, and do not reflect the real outcome of an advection-dispersion process.

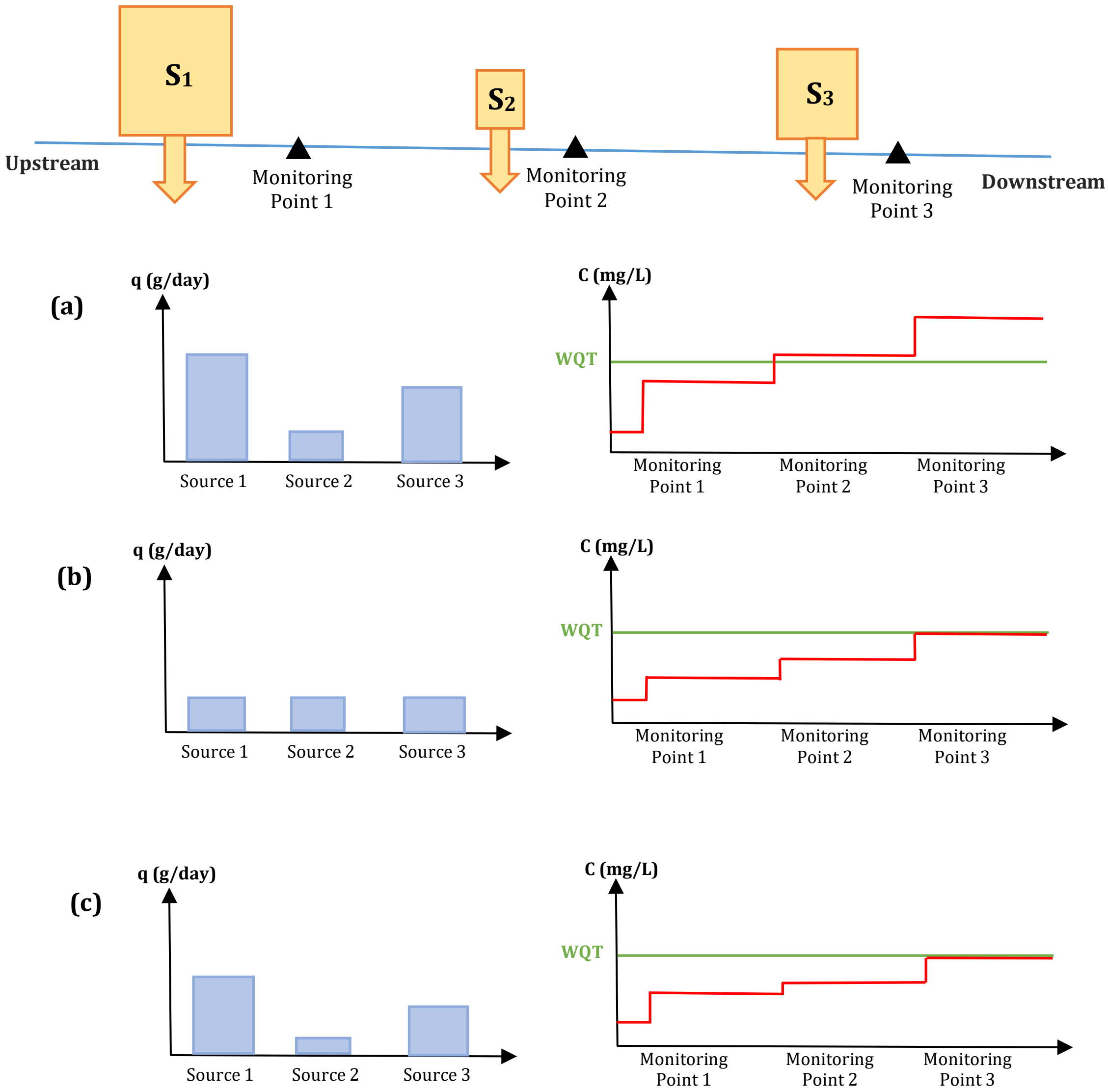

Figure 1. A conceptual model of wastewater load allocation (a) before allocation, b) equal allocation approach, c) proposed allocation approach

As can be seen from the conceptual example, there are three pollutant point sources in the river system. The influence of these source locations on the receiving water body can be measuring concentrations at three monitoring points, each located downstream of a source. Figure 1(a) represents a case where no allocation plan is followed by the decision-makers. In this case, each source discharges the pollutant without considering the WQT in the receiving water body, therefore WQTs are not satisfied at the second and third monitoring points. In Figure 1(b), the optimization approach has been applied by considering the equality approach such that all the sources have the same pollutant loads. As shown, WQT limits are satisfied for all the monitoring points. On the other hand, in Figure 1(c), the pollutant loads are allocated using weights that are proportional to initial load allocations. As can be seen, the final loads are allocated proportionally to the initial condition while satisfying the WQT at all monitoring locations. Similarly, it is possible to assign different load allocation weights to different locations depending on their relative load allocation importance to each other. The following section explains how this proposed load allocation procedure is mathematically applied to the solution of the problem.

2.1. Proposed Simulation-Optimization Approach

The objective of the optimization model is to maximize the total pollutant loads at the source locations subject to WQTs at the monitoring points. Mathematically, this optimization objective can be formulated as in Eq (1): $(i = 1, 2, 3, \dots, n_d;\ \ j = 1, 2, 3, \dots, n_m;\ \ t = 1, 2, 3, \dots, n_t)$:

$$Z = \max\left\{\sum_{i=1}^{n_d}(q_i - \lambda_1 \times (q_i - \omega_i \times q^*)^2) - \lambda_2 \times \sum_{j=1}^{n_m}\sum_{t=1}^{n_t}\left(C_j(t) - \tilde{C}\right)^2\right\} \tag{1}$$

subject to Eq (2), Eq (3), Eq (4), Eq (5) and Eq (6):

$$q_i = \mathcal{C}_i \times Q_i \tag{2}$$

$$q^* = \frac{\sum_{i=1}^{n_d} q_i}{\sum_{i=1}^{n_d} \omega_i} \tag{3}$$

$$C_j(t) = \sum_{i=1}^{n_d} \alpha_{i,j}(t) \times q_i + C_j^0(t) \tag{4}$$

$$\mathcal{C}_{\min} \le \mathcal{C}_i \le \mathcal{C}_{\max} \tag{5}$$

$$\alpha_{i,j}(t) = \frac{\partial\left(\hat{c}_j(t) - c_j^0(t)\right)}{\partial q_i} \tag{6}$$

where, n_d is the number of point sources, n_m is the number of monitoring points, n_t is the time step and q_i is the load of the i^{th} point sources, Z is the objective function value to be maximized, λ_1 is the first penalty coefficient, which maintains the weighted load allocation among pollution sources, λ_2 is the second penalty coefficient that ensures highest possible load discharges from the point sources, ω_i is the load allocation weight of point sources, q^* is the allocated load, which ensures that the load of the pollutant is allocated among the source locations at desired levels (q^* equals to the mean of q_i , if ω_i values are all equal to 1), $C_j(t)$ is the concentration of the j^{th} pollutant calculated by the response-matrix and $\tilde{C}$ is the WQT for the CBOD$_5$ parameter, $\mathcal{C}_{\min}$ and $\mathcal{C}_{\max}$ are the minimum and maximum CBOD$_5$ concentrations.

As can be seen from Equation 1, the objective function of the optimization model includes two penalty functions. The first penalty function is used to allocate the pollutant loads among the source locations proportionally with the given load allocation weights (ω_i). The second penalty function is used to ensure that the differences between the simulated pollutant concentration and WQT value are minimized. Note that the optimization formulation given above also includes the components of the CRM-based surrogate model. The proposed CRM based surrogate model is based on the principle of linear superposition which requires of linear relationship between the input and output data. It can also be used to simulate the fate and transport of the multiple water quality parameters. The elements of CRM are calculated by executing the AQUATOX water quality simulation model for unit load discharges from the source locations. After each model execution, the resulting pollutant concentrations at the monitoring points are saved. The background concentrations are then subtracted from the simulated concentrations to obtain an independent response of the system for the given unit loadings. The calculated CRM can then be used as a surrogate water quality simulation model and integrated into the optimization model for solving the WLA problem. Detailed information regarding the proposed CRM-based water quality simulation model can be found in Sadak (2019). Note that all solutions are conducted using the differential evolution (DE) approach in the optimization model. DE is an evolutionary-based heuristic optimization approach and has similar computational steps with the genetic algorithm (GA) where the natural evolution process is simulated through mutation, selection, and crossover operations. Despite their similarities, there are some differences such as most GA applications consider the binary coding system whereas DE considers real number coding systems. Furthermore, each candidate solution in GA is subjected to the genetic evolution process if the associated probability of that process is satisfied whereas each candidate solution in DE is subjected to those processes without considering any probability. Compared to other heuristic optimization algorithms, DE is relatively easy to employ and is less prone to get stuck in local optimums which is one of the reasons it is used to solve the WLA problems in this study.

3. Study Area

The applicability of the proposed simulation-optimization approach is evaluated by considering hypothetical but realistic water quality parameters on a tributary of a sub-watershed of the Kucuk Menderes River Basin (KMRB). The KMRB is located in the western part of Turkiye (Figure 2) and lies between 38° 41′ 05′′ and 37° 24′ 08′′ N latitudes and 28° 24′ 36′′ and 26° 11′ 48′′ E longitudes. The main river reach of the basin has a mean discharge of 11.45 m3/s and nearly 130 km length that originates from the Kiraz region and together with other tributaries, it discharges all the carrying water to the Aegean Sea. In particular, the city of Izmir, which is the third largest city in Turkiye, is located in the lower basin. Therefore, the water quality of the Kucuk Menderes River is prone to serious environmental stresses since industrial and agricultural activities are very dominant around Izmir.

Figure 2 also includes the location of this tributary which is called the Ilica Stream. Note that this hypothetical example includes 5 point sources, and the impact of these sources is recorded at three monitoring points. Locations of the point sources and monitoring points are given in Figure 3. Among the point sources shown in Figure 3, S_1 represents a domestic wastewater treatment plant, S_2 is considered as a point source representing the mass influx from the tributary, Uladi Stream. The remaining three sources (S_{3-5}) represent the discharge locations of the industrial facilities in the region. After defining the point sources and monitoring locations, the fate and transport of the $CBOD_5$ water quality parameter is simulated by using the AQUATOX simulation model. This study is one of the outputs of the TUBITAK research project, and data related to the study area were obtained due to detailed field studies. As mentioned earlier, a hypothetical water quality model has been created using real field measurement and pollutant point sources.

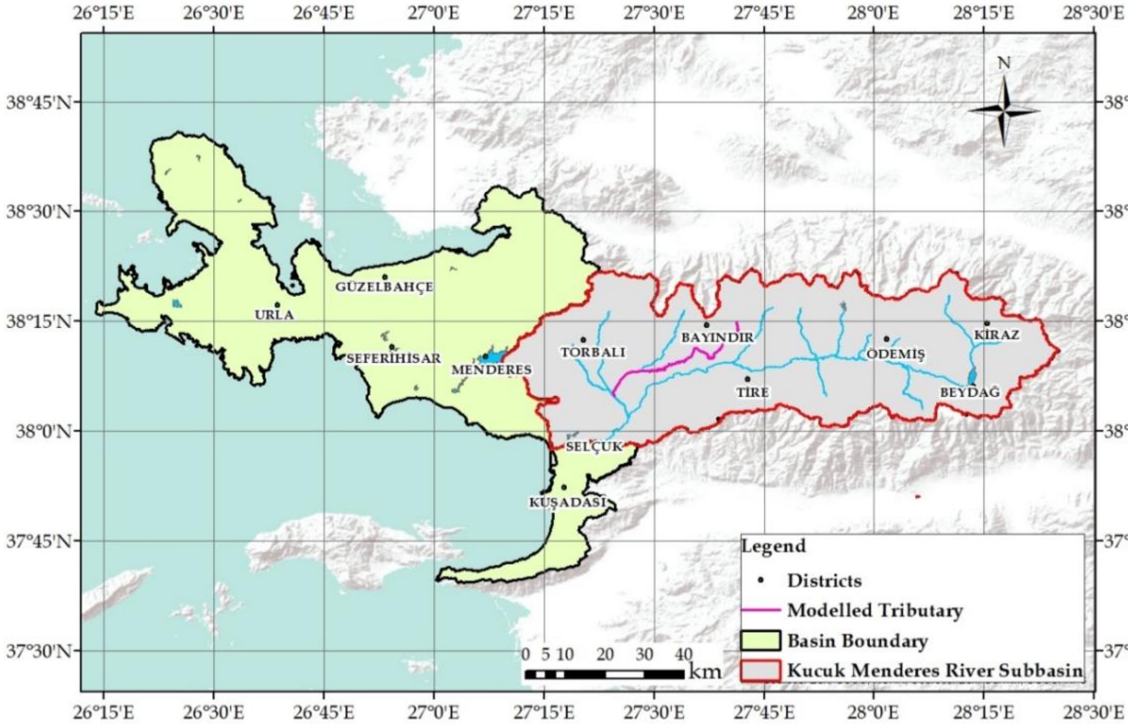

Figure 1. The Kucuk Menderes River and its basin boundary

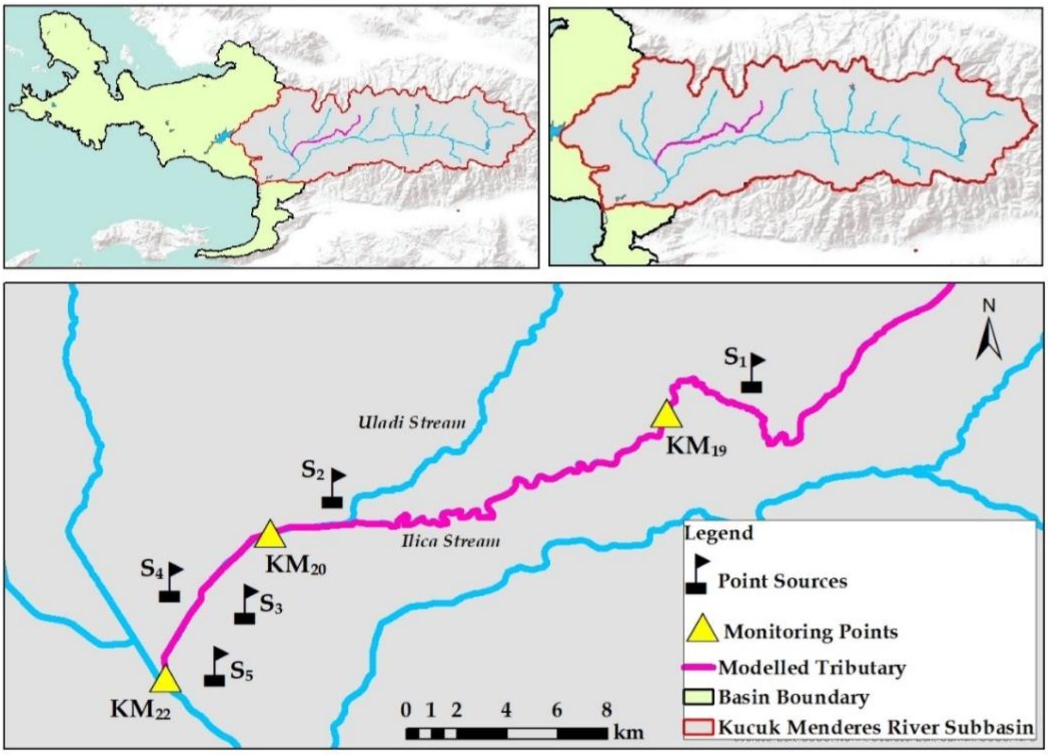

Figure 2. Application study area on the Kucuk Menderes river sub-basin

4. Model Application

As explained previously, the proposed simulation-optimization approach aims to allocate the pollutant loads among the source locations based on the given load allocation weights. To this aim, four different hypothetical load allocation scenarios have been considered to evaluate the applicability of the proposed load allocation scheme (Table 1). In the first scenario, the load allocation weights are taken as 1 for all the sources. In the other scenarios, different load allocation weights are considered for the point sources to evaluate if the pollutant loads are proportionally allocated among the source locations or not. For all the scenarios, the following site characteristics were used: Number of sources: $n_d = 5$ (S_1, S_2, S_3, S_4, S_5); Number of pollutants: $n_c = 1$ (organic matter in the form of suspended and dissolved detritus); Number of monitoring points: $n_m = 3$ (KM-19, KM-20, KM-22); Number of time steps: $n_t = 30$ days. Note that the penalty coefficients of λ_1 and λ_2 have been selected as 1 and 10^9 , respectively according to previous trials. Furthermore, the WQT for the model output $CBOD_5$ was selected as $\tilde{C} = 8$ mg/L considering environmental quality standards for the optimization process.

Table 1. The load allocation coefficients (ω_i) for each scenario

Sources	Scenario 1	Scenario 2	Scenario 3	Scenario 4
S_1	1	2	1	2
S_2 (Tributary)	1	1	1	1
S_3	1	1	1.5	1
S_4	1	1	1	2
S_5	1	1	2.5	3

5. Results

Application results of the simulation-optimization approach for Scenario 1 – 4 are summarized in Figure 4. It is evident that the proposed approach allocates the total pollutant loads among point sources proportionally with the given load allocation weights. For example, since the load allocation weights in Scenario 1 are the same, all the sources get the same pollutant loads as expected by the optimization model. For Scenario 2, since only the first source has a weight of 2 whereas the others have 1, the first source location gets two times greater pollutant loads than the others in the basin. Note that all of these load allocation weights are hypothetically generated for evaluating the applicability of the proposed simulation-optimization approach.

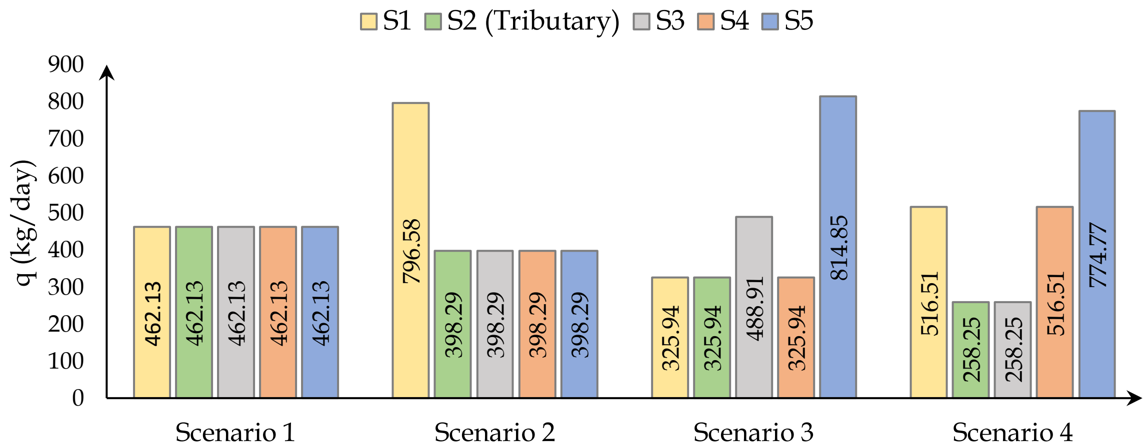

Figure 4. Simulation-optimization model results for each scenario

Another important result of the simulation-optimization model is the $CBOD_5$ concentrations which, it should be lower than 8 mg/L throughout the river system for the satisfactory water quality. For the output $CBOD_5$ concentrations, comparison of the post allocation final calculated values at the monitoring points with the corresponding WQT is given in Table 2. As can be seen for all the scenarios, the calculated $CBOD_5$ concentrations are lower than the WQT at KM-19 and 20. On the other hand, the $CBOD_5$ concentration is equal to the WQT at monitoring point KM-20, which is an expected result since KM-20 is located in the downstream reach of the tributary. This also means that the simulation-optimization approach allocates the maximum amount reasonable load among the sources.

Table 2. Resulting $CBOD_5$ concentrations for the obtained load allocations of each scenario

	$\tilde{C}$ (mg/L)	$CBOD_5$ concentrations in the stream after load allocation $C_j(30)$ (mg/L)			
		Scenario 1	Scenario 2	Scenario 3	Scenario 4
KM-19		2.33	4.01	1.64	2.60
KM-20	8	5.82	6.51	4.80	5.40
KM-22		8.00	8.00	8.00	8.00

6. Conclusions

In this study, a simulation-optimization approach is proposed for solving the WLA problems in river basins. The proposed approach aims to allocate the pollutants loads among the sources by considering environmental WQT values in the receiving water body. Furthermore, this proposed approach considers the load allocation weights for all the point sources to allocate the total loads as to be proportional to the provided weights. This is one of the most important contributions of this study since the proposed approach suggests controlling the load allocations at certain levels for all the source locations. To simulate the fate and transport of the pollutants in river systems, a new CRM-based surrogate water quality simulation approach is also developed which is the other important contribution in this study. This developed CRM-based surrogate model is integrated with a DE-based optimization model. The performance of the proposed simulation-optimization approach is evaluated on a sub-watershed of the Kucuk Menderes river basin in Turkiye by considering different waste load allocation scenarios. Identified results indicated that the proposed simulation-optimization approach can successfully allocate pollutant loads by considering the provided load allocation weights and by satisfying the WQT values for all the monitoring points.

Acknowledgments

Acknowledgments: This study is funded by The Scientific and Technological Research Council of Turkiye (TUBITAK) under Project Number 116Y413/116Y414/116Y415.

Author Statement

The authors have contributed to this paper in this manner:

Derya Sadak: Development of the simulation-optimization approaches, programming, manuscript preparation; M. Tamer Ayvaz: Development of the simulation-optimization approaches, programming, evaluation of the results, manuscript preparation; Alper Elçi: Building of the water quality simulation model, evaluation of the results, manuscript preparation; Mehmet Dilaver: Evaluation of the results, manuscript preparation; Selma Ayaz: Evaluation of the results, manuscript preparation.

Conflict of Interest

There is no conflict of interest for this study.

References

Afshar, A., & Masoumi, F. (2016). Waste Load Reallocation in River–Reservoir Systems: Simulation–Optimization approach. *Environmental Earth Sciences,* 75 (1), 53.

Afshar, A., Masoumi, F., & Solis, S. S. (2018). Developing a Reliability-Based Waste Load Allocation Strategy for River-Reservoir Systems. *Journal of Water Resources Planning and Managemen*t, 144(9).

Boese, G. W. (2002). Approaches to the Allocation of Loads in TMDLs. *Water Environment Federation,* 2002(8), 930–953.

Burn, D. H., & Yulianti, J. S. (2001). Waste-Load Allocation Using Genetic Algorithms. *Journal of Water Resources Planning and Management*, 127(2), 121-129. https://doi.org/10.1061/(ASCE)0733-9496(2001)127:2(121).

Cardwell, H., & Ellis, H. (1993) Stochastic Dynamic Programming Models for Water Quality Management. *Water Resour. Res*., 29(4), 803–813.

Cho, J. H., Ki, S. S., & Sung, R. H., (2004). A River Water Quality Management Model for Optimising Regional Wastewater Treatment Using a Genetic Algorithm. *Journal of. Environmental Management*, 73(3), 229-242.

Deininger, R. A. (1965). Water Quality Management: The Planning of Economically Optimal Pollution Control Systems. *Ph.D. Thesis*, Northwestern University.

Deng, Y.X., Zheng, B.H., Guo, F., Lei, K., & Li, Z.C. (2010). Study on the Total Water Pollutant Load Allocation in the Changjiang (Yangtze River) Estuary and Adjacent Seawater Area. *Estuarine, Coastal and Shelf,* (3), 331–336.

Directive 2000/60/EC of the European Parliament and of the Council of 23 October 2000 on Establishing a Framework for Community Action in the Field of Water Policy

Gorelick, S. M. (1982a). Optimal Dynamic Management of Groudwater Polluant Sources. *Water Resources Research*, 18(1), 71-76.

Gorelick, S. M. (1982b). A model for Managing Sources of Groundwater Pollution. *Water Resources Research*, 18(4), 773– 781.

Han, H.Y., Li, K.Q., Wang, X.L., Shi, X.Y., Qiao, X.D., & Liu, J. (2011). Environmental Capacity of Nitrogen and Phosphorus Pollutions in Jiaozhou Bay, China: Modeling and Assessing. *Marine Pollution Bulletin*, 63 (5), 262–266.

Jia, Y. B., & Culver, T.B. (2006). Robust Optimization for Total Maximum Daily Load Allocations. *Water Resources Resources*, 42(2).

Klemetson, S.L., & Grenny, W.J. (1985). Dynamic Optimization of Regional Wastewater Treatment Systems. *Journal of Water Pollution Control Federation*, 57(2), 128–134.

Liebman, J. C., & Lynn, W. R. (1966). The Optimal Allocation of Stream Dissolved Oxygen. *Water Resources Research*, 2(3).

Park, R. A., Clough, J. S., & Wellman, M. C. (2008). AQUATOX: Modeling Environmental Fate and Ecological Effects in Aquatic Ecosystems. *Ecological Modelling,* 213(1), 1-15

Parmar, D. L., & Keshari, A. K. (2014). Wasteload Allocation Using Wastewater Treatment and Flow Augmentation. *Environmental Model Assessment*, 19, 35-44.

Revelle, C.S., Loucks, D.P., & Lynn, W.R. (1968). Linear Programming Applied to Water Quality Management. *Water Resour. Res.*, 4(1), 1–9.

Sadak, D. (2019). Identification of Receiving Water Body Based Discharge Limits by Using Simulation-Optimization Models. M*aster's Thesis (Pamukkale University Institute Of Science, Civil Engineering)*.

Sadak, D., Ayvaz, M. T., & Elçi, A. (2020). Allocation of Unequally-Weighted Wastewater Discharge Loads Using a Simulation-Optimization Approach. *Journal of Hydrology*, 588.

Sadak, D., Ayvaz, M. T., Elçi, A., Dilaver, M., & Ayaz, S. (2022). A Simulation-Optimization Approach for Solving the Wastewater Load Allocation Problems in River Basin Systems. *International Conference Hydroscience & Engineering*, May 26-27, Izmir, Turkiye.

Saadatpour, M., & Afshar, A. (2007). Waste Load Allocation Modeling Fuzzy Goals; Simulation-Optimization Approach. *Water Resources Management*, 21, 1207-1224.

Saadatpour, M. Afshar, A., & Khoshkam, H. (2019). Multi-objective Multi-pollutant Waste Allocation Model for Rivers Using Coupled Archived Simulated Annealing Algorithm with QUAL2Kw. *Journal of Hydroinformatics*, 21(3), 397-410.

Su, Y., Li, K., Liang, S., Lu, S., Wang, Y., Dai, A., Li, Y. B., Ding, D., & Wang, X. (2019). Improved Simulation–Optimization Approach for Identifying Critical and Developable Pollution Source Regions and Critical Migration Processes for Pollutant Load Allocation. *Science of Total Environment*, 646, 1336-1348.

Su, Y., Li, K.Q., Yang, B., Liang, S.K.,Wang, X.L., Bao, X.W., Jiang,W.S., & Li, Y.B. (2018). Improving Land-based Total Nitrogen Load Allocation Using a Variable Response Matrix-based Simulation–Optimization Approach: A Case Study. *Ecological Indicators*, 91, 575–588.

Zou, R., Liu, Y., Riverson, J., Parker, A., & Carter, S. (2010). A Nonlinearity Interval Mapping Scheme for Efficient Waste Load Allocation Simulation-Optimization Analysis. *Water Resour. Res.*, 46 (8), W08530.

Scientific Research Communications

Research Article

Sci. Res. Comm. (2023)
Volume 3, Issue 1
doi: 10.52460/src.2023.005

Numerical Modeling of Flow Pattern at a Right-angled River Bend Using CCHE2D Model

Animesh Das[1,*] Sushant Kumar Biswal[2]

[1] Civil Engineering Department, National Institute of Technology, Agartala, Tripura, India
[2] Civil Engineering Department, National Institute of Technology, Agartala, Tripura, India
[*] Corresponding author: sushantb69@gmail.com

Received: 14.10.2022 Accepted: 31.01.2023

Abstract

In this study, the CCHE2D model is used to analyse the flow pattern in a meander reach of the Gomati River. The finite volume method is used by the numerical model to solve the depth-averaged two-dimensional equations with $k - \varepsilon$ turbulence closure. The numerical findings were compared with field data for two different flow rates in order to calibrate the CCHE2D model using various Manning's roughness coefficients. The results show that for the minimum and maximum discharges, a smaller Manning's roughness factor ($0.015 \geq n \geq 0.025$) is more favorable to a higher Manning's roughness factor ($0.030 \leq n \leq 0.040$). The results of the numerical model demonstrated that fluctuations in hydraulic parameters including shear stress, velocity, flow depth, and Froude number in the river bend are greatly influenced by the existence of centrifugal force and helical cells. The linear relationship between velocity and shear stress is presented across the whole study reach, as indicated by the R-square and linear correlation coefficient (r) components. The results of the model show that the flow field within the river bend can be accurately simulated by the computational model.

Keywords: Gomati River; CCHE2D; Manning's coefficient; meander reach

1. Introduction

One of the most common river patterns found in nature are meandering rivers, which are formed into different shapes by rivers due to their dynamic character. Its platform is always changing, and these changes have a big impact on the morphology and hydraulic condition. Meandering rivers are single channels with a sinuous planform composed of a succession of loops that are often irregular, asymmetrical, and complex in reality though being shown as having regular form and size (Hooke, 2013). The effects of secondary flow, free surface variation, section geometry, and flow separation along the inner bend wall, which are not seen along straight paths, combine to produce extremely complex three-dimensional (3D) flows in meander rivers or river bends. One of the key aspects of open channel flows is the distribution of flow velocity in the longitudinal and lateral directions. This aspect is related to a variety of flow characteristics, such as the water profile, the distribution of shear stress, secondary flow, channel conveyance, and other flow entities. Secondary currents are one of the important characteristics that define flow in meander bends. According to Chang (1984), even for small curves without flow separation, flow resistance or the energy cost caused by transverse flow can be extremely large. Many researchers have studied flow dynamics in a wide variety of channel bend configurations using various methods owing to the major significance of this content (Tominaga and Nagao, 2000; Blanckaert and Graf, 2001; Booij, 2003; Blanckaert and De Vriend, 2004; Lu et al., 2004; Bodnar and Prihoda, 2006; Roca et al., 2007; Blanckaert, 2009; Zhou et al. 2009). These studies aim to collect data on flow variables in channel bends and analysis of the results that have provided the knowledge base for understanding the bend flows. Due to improvements in computers and numerical computation techniques, Computational Fluid Dynamics (CFD) models have seen a substantial increase in use in recent decades for studying outdoor channels and river dynamics. In order to solve difficult hydrodynamic issues, numerical models have been applied widely at different scales. Various types of numerical models have been employed to explain the details of flow within bends and meandering channels using different turbulence modelling techniques, such as the direct numerical simulation (DNS), large eddy simulations (LES), or the Reynolds-Averaged Navier–Stokes (RANS) approach.Ye and Mccorquodale (1998) simulated the flow and mass transfer in a 270° curved channel using a mathematical model of 3D free surface flows. A fractional three-step implicit algorithm uses a collocated grid system to solve the governing equations. A two-dimensional (2D) numerical model was used by Lien et al. (1999) to study the flow pattern at a 180° bend with a rigid bed. They found that the secondary flow significantly affects the flow patterns and the path of maximum velocity along the channel. Huang et al. (2009) used various pressure solution techniques along with different turbulence closure methods, to evaluate the spiral flows in an experiment's curved channel, use models like the $k - \varepsilon$ model and the mixing-length model. To understand hydrodynamics sedimentation and its transport mechanism, a general tool CCHE2D was developed by National Center for Computational Hydro Sciences and Engineering (NCCHE), University of Mississippi. CCHE2D is widely used by the riverine scientist for sediment and flow modelling Singh (2005); Kamanbedast (2013). CCHE2D model has been used for simulation at the Nile River (Elbogdady reach), and multi parametric sensitivity with different roughness parameters were evaluated using RSQ and r factors (Nassar, 2011). Mohanty et al. (2012) investigated wide meandering compound channels using CCHE2D to analyse the depth-averaged velocity. The results indicated that centrifugal force and secondary flow have a significant impact on the flow patterns in a channel bend. The maximum velocity in the main channel is closer to the inner bend whether it is above or below the bank level, according to McKeogh and Kiely's (1989) analysis of the velocity profile in meandering compound rivers. Elyasi and Kamandbedast (2014) used the CCHE2D model to investigate numerical modeling of river flow with a 90 degree bend. The results of flow pattern simulations in meandering sections using the CCHE2D model in the Khoshke-rud river in Iran show that using numerical flow simulations for flow modeling is a step closer to being a universal predictor of processes in meandering rivers (Fathi et al., 2012). Yusefi Haghivar et al. (2017) used CCHE2D model to investigate the hydraulic parameters of flow depth and velocity in the Karoon River, Iran. Ultimately, it became clear that there was a subtle harmony between changes in river depth and flow, with most changes occurring in meanders and bends. Scott and Jia (2005) concluded that CCHE2D is capable of simulating both hydrodynamic and sediment properties of complex river network and has proved the model as a valuable tool for engineering projects. Current study performs flow analysis in the meander reach of the Gomati River using the CCHE2D modelling software.

A review of the literature shows that there are few comprehensive studies of 2D numerical modelling of meandering flow. The goal of this work is to analyse earlier studies that assessed a river meander’s flow characteristics using numerical techniques. In the present study, the flow pattern of the Gomati River s analysed using the most recent CCHE2D modelling software. This study utilizes a numerical model that solves the 2D depth-averaged conservation equations to examine the flow characteristics of a meander reach with a 90° angled bend for the Gomati channel. The main goals of this study are to analyse the flow patterns in meander reaches and to measure various hydraulic parameters in the Gomati River study course, including shear stress, total specific discharge, velocity, and Froude number. Different Manning's roughness coefficients are used as the initial conditions to calibrate the CCHE2D model for the Gomati River flow simulation, and simulation results are compared with measured flow data.

2. Materials and Methods

2.1 Study Area

The Gomati River, 56 kilometers south-west of Agartala, is the site of a significant field project on the river bend that includes in this study (Figure 1). The Gomati catchment covers 2492 km² (1921 km² belongs to hilly region and only 571 km² about 23% lies on the plain) is located in the lower middle part of Tripura. It is located between 23°47′N and 23°47′N in latitude and 91°14′E and 91°58′E in longitude. The Gomati River is the largest river of State of Tripura, India and the river is 167.4 kilometers in length, with an elevation range of 18.288 to 112.166 meters above mean sea level.

Table 1. Physical parameters of the present study.

Stream length (s_L), m	Valley length (V_L), m	Width (B), m	Bed slope (S)	Angle (β), degree	Radius of curvature (R_C), m	Sinuosity (K)
94.62	53.16	42.7	0.0006	90	60.22	1.78

The Gomati River's 94.62 m bend is used in the current study for flow simulation to understand the behavior of river flow dynamics. A bathymetric survey was carried out to obtain information at the study site under consideration. Hydrologic data were collected throughout the field campaign at upstream stage recorders, and were converted to discharge values using stage-discharge rating curves (Figure not shown). The rating curve is the relationship between stage (river water level) and streamflow (discharge). A rating curve was established, because at many channel locations, the discharge is not a unique function of stage; but also the slope of the water surface, the channel geometry, and the unsteadiness of flow. So, the rating relationship thus established is used to transform the observed stages into the corresponding discharges. Field data is analyzed analytically and compared to stage record data.

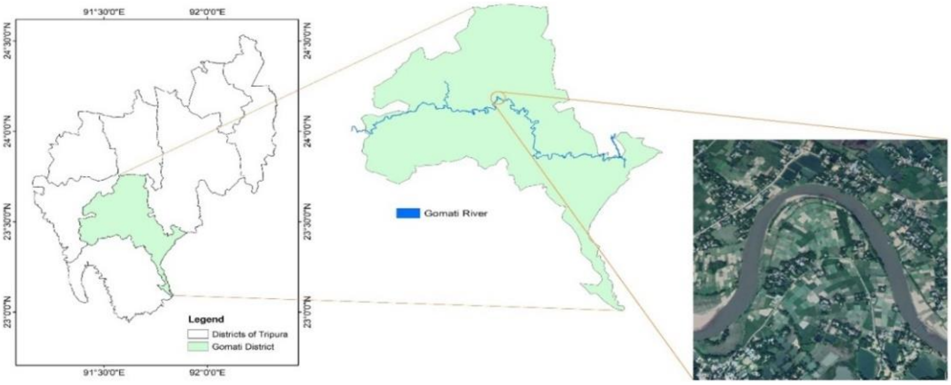

Figure 1. Location map of the considered reach of Gomati River

2.2. CCHE2D Model

The CCHE2D model is a comprehensive software programme for the 2D modelling and analysis of morphological phenomena and free surface flows. Figure 2 shows the flow chart for the flow simulation modelling process utilising the digital elevation model and the integration of CCHE2D models and Arc GIS. The package comprises of the numerical models, a mesh generator (CCHE2D Mesh Generator) and a Graphical User Interface (CCHE2D-GUI). For the CCHE2D model system, the mesh generator helps in the formation of a complex structured mesh system. The CCHE2D series, which includes the grid generator and CCHE2D-GUI, was used to create a topographical file that could be loaded as part of the modelling procedure. In the earlier, each of the flow data is input using a flow input device, which is then utilised to do analysis and show the results. In the former, topographic data are used to construct a mesh. The digital elevation topography data received that was clipped in ArcGIS primarily contained the river bend that is significant for the overbanks. The Digital Elevation Model (DEM) was cropped and then converted to ASCII output in order to be input into CCHE2D Model Generator. After the topography data was loaded into the CCHE2D grid generator, the block defining the boundaries of the river was generated. The mesh generating toolbar was used to discretize the algebraic mesh created from the topography into finer meshes. A minimum number of dry grid cells were used with arbitrary initial flow parameters, such as the initial depth of the water surface at the river inflow and outlet. The water surface level was interpolated using the interpolation tool in the set flow beginning conditions toolbar. The roughness characteristics were entered into the CCHE2D-GUI with probable values for the overall topography. The water surface level and flow discharge were set using intake boundary condition and outlet boundary condition, respectively, in the current study. Ten-second time steps were utilised to simulate an entire day. This study only utilise the hydraulics capability of CCHE2D.

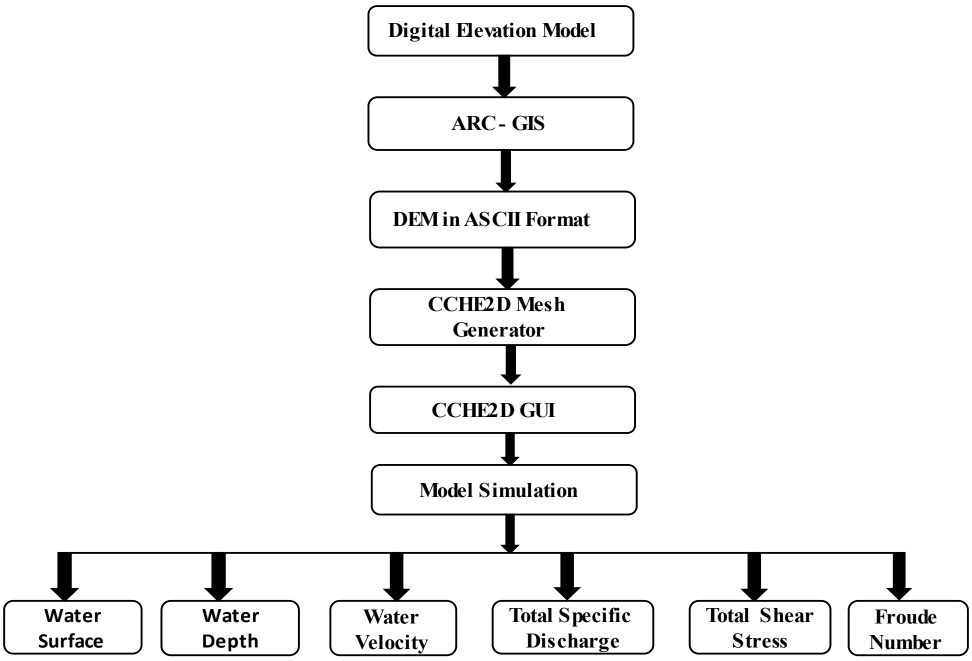

Figure 2. Flow chart shows the operations involved in the flow simulation modelling with the digital elevation model and the combination of Arc GIS and CCHE2D models

2.3 Numerical Method

Numerical model was applied to solve depth-averaged two-dimensional conservation equations with $k-\varepsilon$ turbulence closure using CFD software (CCHE2D) model. In the present study, the Finite volume method (FVM) with the second order upwind scheme is used to discretize the governing equations. The governing 2D continuity and momentum equations for an incompressible fluid flow are written as Eq. (1), Eq. (2) and Eq. (3):

Continuity Equation

$$\frac{\partial Z}{\partial t} + \frac{\partial (hu)}{\partial x} + \frac{\partial (hv)}{\partial y} = 0 \tag{1}$$

Momentum Equations

$$\frac{\partial u}{\partial t} + u\frac{\partial u}{\partial x} + v\,\frac{\partial u}{\partial y} = -gh\frac{\partial Z}{\partial x} + \frac{1}{h}\left[\frac{\partial (h\tau_{xx})}{\partial x} + \frac{\partial (h\tau_{xy})}{\partial y}\right] - \frac{\tau_{bx}}{\rho h} + f_{Cor}v \tag{2}$$

$$\frac{\partial v}{\partial t} + u\frac{\partial v}{\partial x} + v\,\frac{\partial v}{\partial y} = -gh\frac{\partial Z}{\partial y} + \frac{1}{h}\left[\frac{\partial (h\tau_{yx})}{\partial x} + \frac{\partial (h\tau_{yy})}{\partial y}\right] - \frac{\tau_{by}}{\rho h} + f_{Cor}u \tag{3}$$

where u and v are depth integrated velocity components in x and y directions respectively, g is gravitational acceleration, z is the water surface elevation, ρ is water density, h is the local water depth, f_{Cor} is the Coriolis parameter, τ_{xx}, τ_{xy}, τ_{yx} *and* τ_{yy} are the depth integrated Reynolds stresses and τ_{bx}, τ_{by} are shear stresses on the bed surface. The Coriolis parameter f_{Cor} was ignored in this analysis because it has no significant influence for small areas (Dutta et al., 2010).

The DEM, river location, initial water surface elevation, discharge, and Manning's roughness coefficient are the basic input data requirements for operating the CCHE2D model. In addition to the initial conditions, the boundary conditions are applied at the inlet and outlet sections. The flow discharge was defined as a constant valuee for simulation as the inlet boundary condition, and the water surface level was defined for the model as a outlet boundary cconditions. Grids to represent flow depth and flow velocity at any time increment specified by the user compensate the CCHE2D model's output. Grid sensitivity study has been performed to work out the specified number of grid points and their distribution by refining the grid points.

4. Results and Discussions

DEM file in ASCII format was gridded numerically and algebraically. The export results from the mesh editor are given in Figure 3 that shows the bed elevation with minimum and maximum values of 32.79 m and 67.24 m, respectively. The CCHE2D mesh generator was used to interpolate the bed height at random. In order to reduce adverse depths, the beginning water level was higher than 32.79 m for the purpose of this study. The results of the CCHE2D-GUI's flow simulation are shown in Figure 4. The largest long-term monthly average is shown together with the water surface elevation in metres after a simulation time longer than a day.

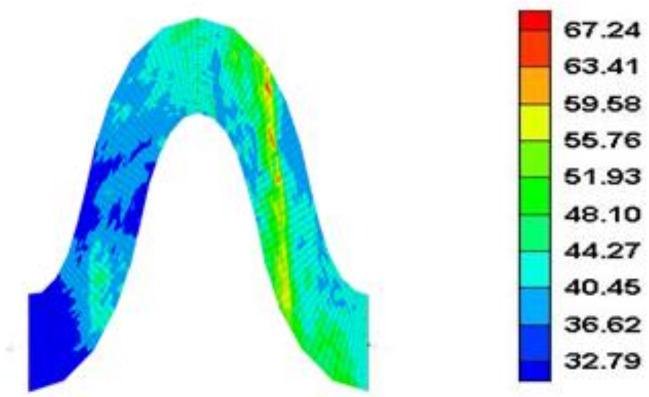

Figure 3. Initial bed elevation (m) generated by CCHE2D

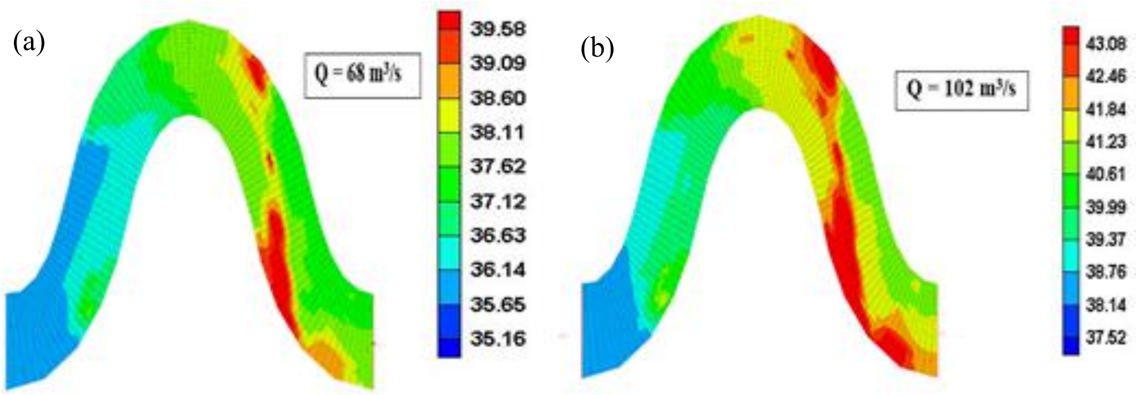

Figure 4. Water surface profile at 90^o meander (a) Q=68 m^3/s, (b) Q=102 m^3/s

In various cross sections of the 90° river bend from the study stretch, Figure 5 shows the cross-profiles of the water surface computed from the CCHE2D numerical model. Due to the presence of secondary currents in the bend, the gradient of the water surface increases to the outer bank. The results show that at a flow of 102 m^3/s, the water surface level rises upstream and attain maximum depth of 6.38 m, while the water depth at the edge of the river is almost zero. The large depth provides information about the size of the river carrying a significant amount of flow. Using more reliable inputs, such as bathymetric data, which can modify the depth results and provides more accurate data on the submerged surfaces The maximum water depth, specific ”Isch’rge, velocity, Froude numbers and total shear stress are reached very near the centreline of river. The results show that the minimum water depth for the reach of study is 0.001 m, and the associated low-depth zones, there is no stream velocity. The muddy area inside the Gomati boundaries, where the discharge is most likely to occur on a long-term monthly average, is shown by this depth. The numerical results demonstrate that as flow enters the curve, centrifugal force leads the water surface to locate a transversal slope. Figure 6 shows the water depth profiles based on six roughness coefficients of 0.015, 0.020, 0.025, 0.030, 0.035, and 0.040 that were obtained from the CCHE2D model and observed data. It can be shown that both the water depth profiles of numerical model and the observational data show a regular trend for different roughness coefficients. The water depth profile of the Gomati River reach was analysed in order to find the optimum roughness coefficient. Two components of the linear correlation coefficient I and coefficient of determination(R^2), as specified by Eq. (4) and Eq. (5), were used in statistical analysis to compare the observed and simulated data for all tests in accordance with Figure 6.

$$\text{Correlation } (r) = N\sum AB - (\sum A \sum B)/[(N\sum A^2) - (\sum A)^2]\,[N\sum B^2 - (\sum B)^2]^{0.5} \tag{4}$$

$$\text{RSQ } (R^2) = \sum_i^j (B - \bar{A})^2 / \sum_i^j (A - \bar{A})^2 \tag{5}$$

where B is the simulated variable, A is the observed variable, $\bar{A}$ is the sample mean of A value, and N the total number of variables.

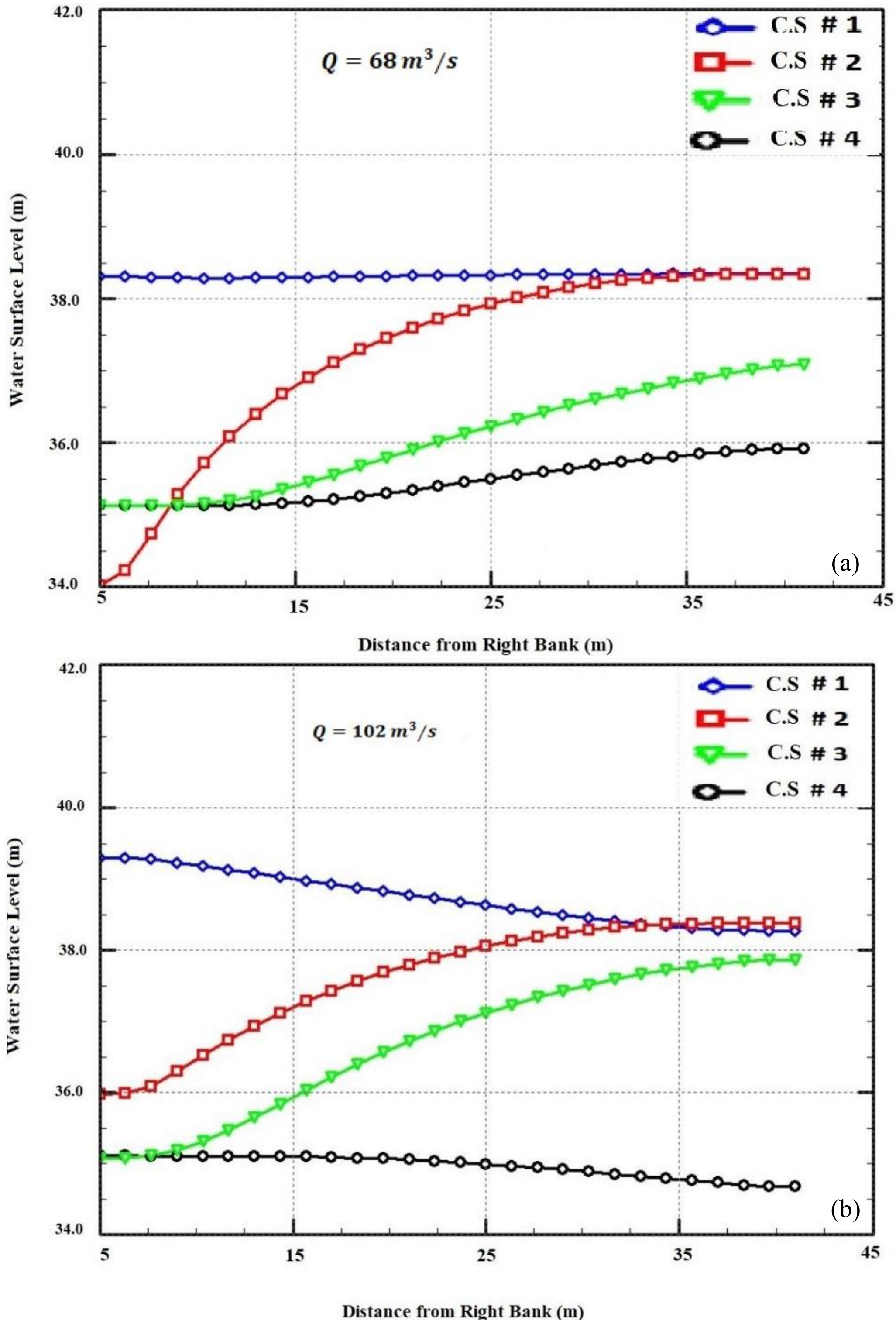

Figure 5. Cross-profiles of water surface at 90^o meander (a) Q=68 m³/s, (b) Q=102 m³/s

Figure 7 shows that Manning's roughness coefficients for low and high discharges (68 m³/s and 102 m³/s) lie within in the range of ($0.015 \geq n \geq 0.025$). Due to the higher roughness coefficients ($0.030 \geq n \geq 0.040$) and smaller depth for modelling, it can be said that the impact of roughness of the bed on flow is greater for low discharge and that the results are better and more accurate when compared to observational data. Therefore, lower roughness coefficients are more acceptable for low and high discharges.

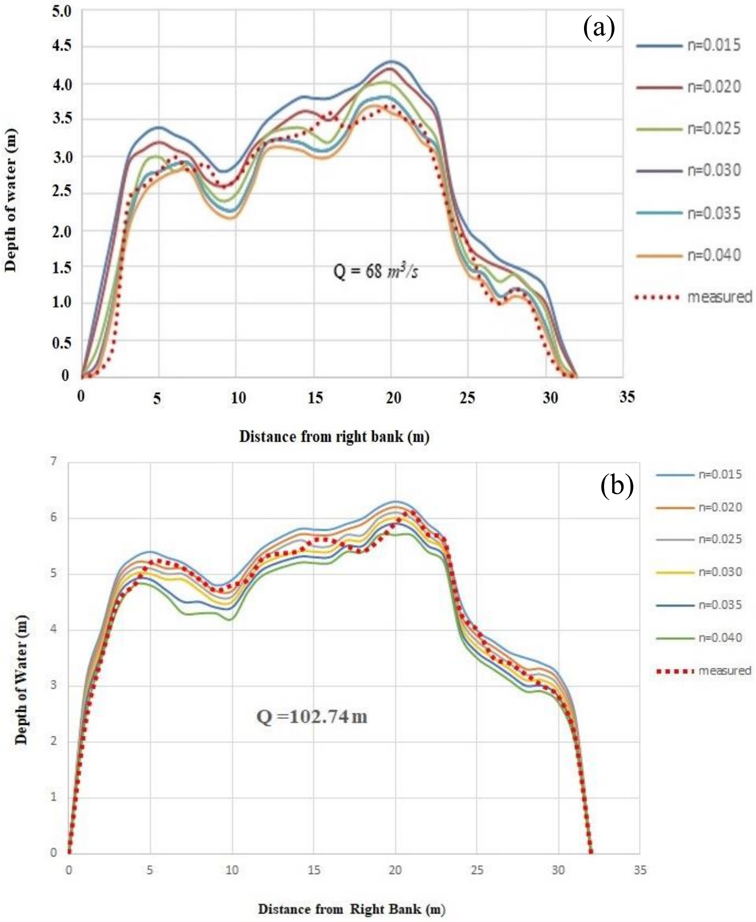

Figure 6. Water depth elevation at 90^o meander (a) Q=68 m^3/s, (b) Q=102 m^3/s

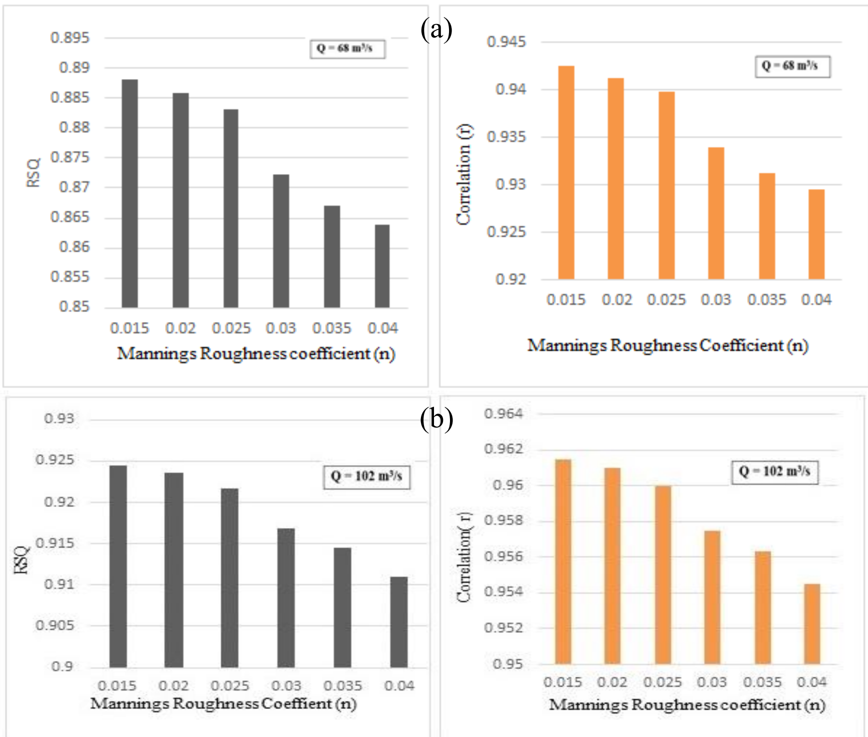

Figure 7. The performance of the CCHE2D model for different Manning's roughness coefficients (a) Q=68 m^3/s, (b) Q=102 m^3/s

Figure 8 shows the velocity profile for a specific discharge along the meandering path through the channel. In the early stages of the meander path, the region of still higher velocity is along the inner wall to the left of the channel section. The higher velocity moves toward the middle of the channel during the cross-over section, as is usually observed in straight channels. Based on this observation, a meandering channel acts like a straight channel just before the cross-over section. The higher velocity goes to the right of the channel section at sections after the cross-over; this is outer wall of the channel section (Figure 9).

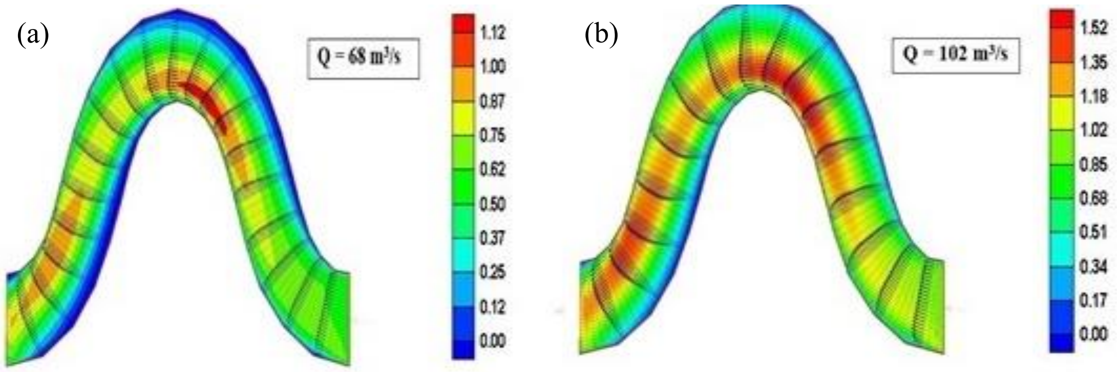

Figure 8. Velocity vector at 90^omeander (a) Q=68 m^3/s, (b) Q=102 m^3/s

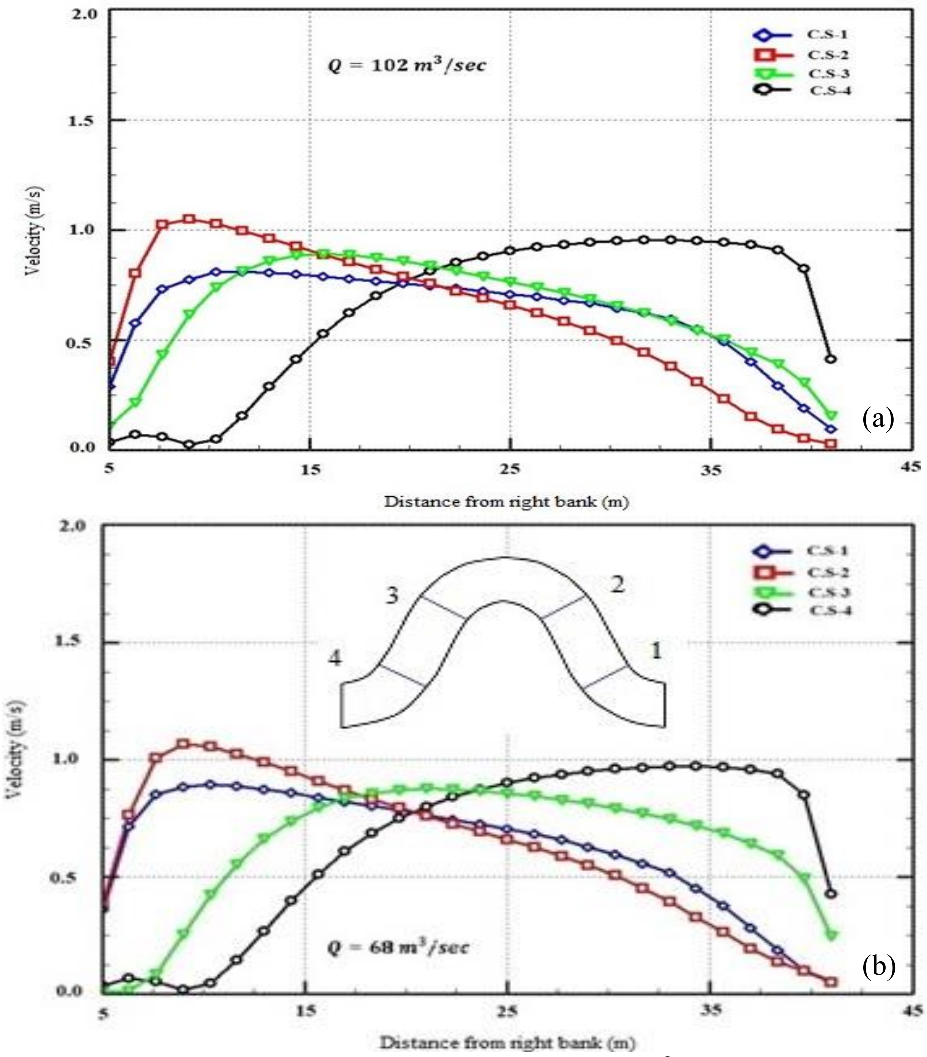

Figure 9. Cross-profiles of velocity at 90^omeander for 102 m^3/s discharges (a) Q=68 m^3/s, (b) Q=102 m^3/s

The boundary shear force distribution along the channel bed directly affects the flow characteristics of an open channel flow. Throughout the bend, the shear stress generally increases with flow and peaks at its highest levels during the highest discharge (Figure 10).

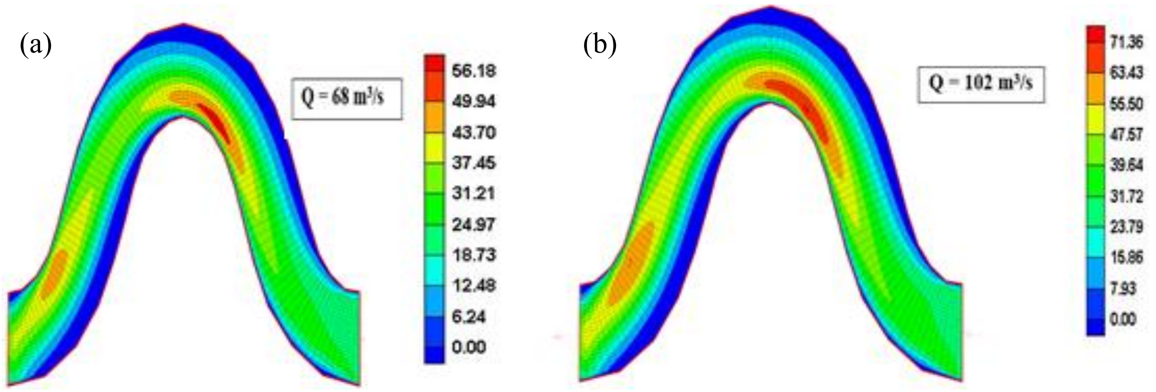

Figure 10. Shear stress at 90^o meander (a) Q=68 m³/s, (b) Q=102 m³/s

The total specific discharge (m²/s) is at its highest along the centreline of the river, as per Figure 11 of the present work, that examines the influence of parameters like specific discharge and Froude number on the flow dynamics.

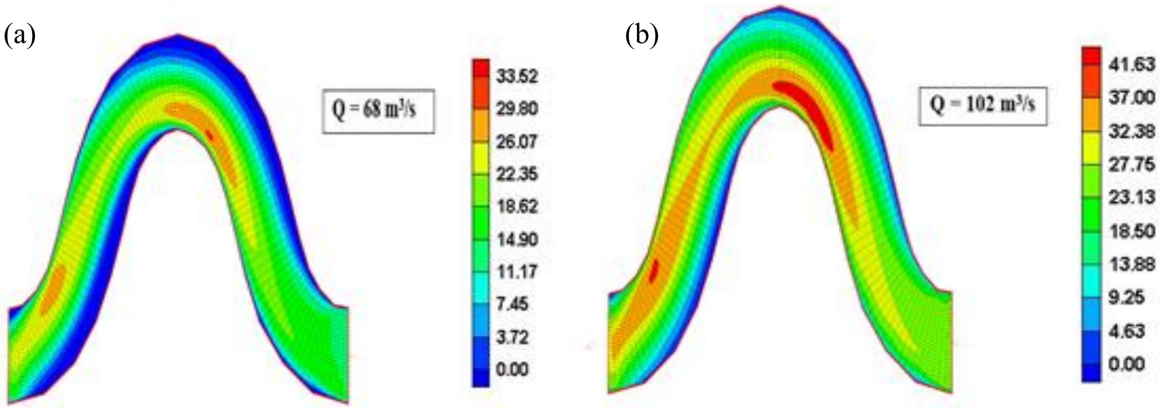

Figure 11. Total specific discharge at 90^omeander (a) Q=68 m³/s, (b) Q=102 m³/s

Figure 12 shows the Froude number mapping, which indicates that the flow in the upstream reach is subcritical ($Fr < 1$), but that it becomes supercritical ($Fr > 1$) as a result of the obstruction in the contraction area upstream. The current study confirmed that the majority of the flow in the channel reach is subcritical.

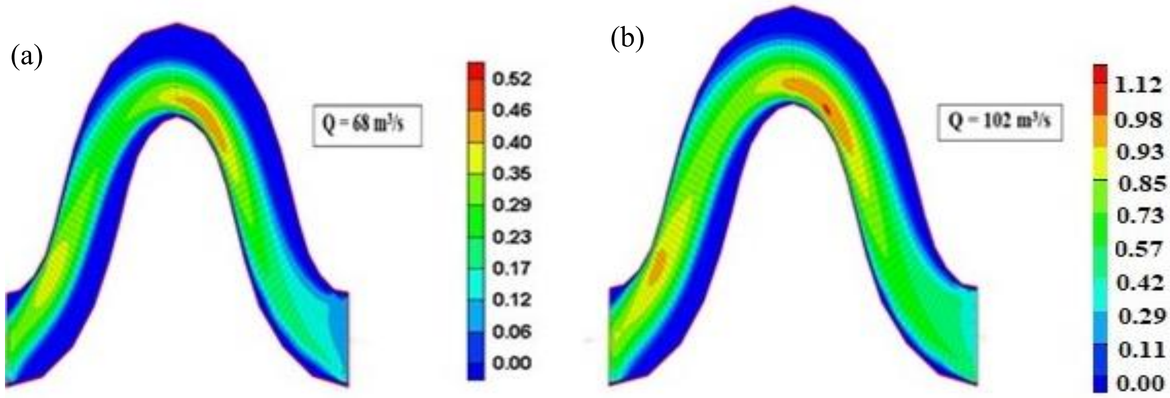

Figure 12. Froude number at 90^o meander (a) Q=68 m³/s, (b) Q=102 m³/s

4. Conclusions

In this study, the flow attributes at a Gomati River bend have been numerically solved using the CCHE2D model. The numerical results were simulated using field data. According to the model results, the roughness factor values of 0.030–0.040 will have better results, and for medium and high discharges, the roughness factor ranges of 0.015–0.025 will provide results that are more accurate. The simulation results also imply that, the average velocity for the discharges of 68 m^3/s and 102 m^3/s in the study reach is 0.56 m/s and 0.77 m/s, respectively. Additionally, the average shear stress for the two discharges mentioned above is 27.99 and 35.62 N/m^2, respectively. The analysis demonstrates that the water surface and the highest velocities in the river arch evolve toward the outer bank. The present study results show that the model is efficient to simulate wide range of flow parameters in riverine system and can better predict sedimentation and erosion. Therefore, the results of this numerical models are reliable and useful in the engineering and operational projects of the Gomati River.

Acknowledgments

The authors would like to thank National Institute of Technology Agartala for providing financial support in completing this study and would like to thank International Conference on Hydroscience and Engineering (ICHE) for the opportunity to publish this work.

Conflict of Interest

The authors declare no conflict of interest.

References

Blanckaert, K. (2009). Saturation of Curvature-Induced Secondary Flow, Energy Losses, and Turbulence in Sharp Open-Channel Bends: Laboratory Experiments, Analysis, and Modeling. *J. Geophys. Res. Earth Surf.*, 114.

Blanckaert, K., & Graf, W. H. (2001). Mean Flow and Turbulence in Open-Channel Bend. *J. Hydraul. Eng.*, 127, 835–847.

Blanckaert, K., & De Vriend, H. J. (2004). Secondary Flow in Sharp Open-Channel Bends. J. *Fluid Mech.*, 498, 353–380.

Bodnar, T., & Prihoda, J. (2006). Numerical Simulation of Turbulent Free-Surface Flow in Curved Channel. *Flow Turbul. Combust.*, 76, 429–442.

Booij, R. (2003). Measurements and Large Eddy Simulations of the Flows in Some Curved Flumes. *J. Turbul.*, 4, 1–17.

Chang, H. H. (1984). Variation of Flow Resistance through Curved Channels. *J. Hydraul. Eng.*, 110(12), 1772-1782.

Dutta, S., Medhi, H., Karmaker, T., Singh, Y., Prabu, I., & Dutta, U. (2010). Probabilistic Flood Hazard Mapping for Embankment Breaching. *ISH Journal of Hydraulic Engineering*, 16(1), 15–25 https://doi.org/10.1080/09715010.2010.10515012.

Fathi, M., Honarbakhsh, A., Rostami, M., Nasri, M., & Moradi, Y. (2012). Sensitive Analysis of Calculated Mesh for CCHE2D Numerical Model. *World Appl Sci J.*, 18, 1037–1051.

Hooke, J. M. (2013). Chapter: River meandering. In *Treatise on Geomorphology* San Diego, CA: Academic Press, 260–288.

Huang, S., Jia, Y., Chan, H., & Wang, S. S. Y. (2009). Three-Dimensional Numerical Modeling of Secondary Flows in a Wide Curved Channel. *J. Hydrodynamics*., 21(6), 758-766.

Kamanbedast, A. A., Nasrollahpour, R., & Mashal, M. (2013). Estimation of Sediment Transport in Rivers Using CCHE2D Model (Case Study: Karkheh River). *Indian Journal of Science and Technoloigy,* 6(2), 138-14 DOI:10.17485/ijst/2013/v6i2.9.

Lien, H. C., Yang, J. C., Yeh, K. C., & Hsieh, T. Y. (1999). Bend-Flow Simulation Using 2D Depth-Averaged Model. *Journal of Hydraulic Engineering,* 125(10), 1097-1108.

Lu, W., Zhang, W., Cui, C., & Leung, A. (2004). A Numerical Analysis of Free-Surface Flow in Curved Open Channel with Velocity-Pressure Free-Surface Correction. *Comput. Mech.,* 33, 215–224.

McKeogh, E. J., & Kiely, G. K. (1989). Experimental Study of the Mechanisms of Flood Flow in Meandering Channels, *Proceedings of the 23rd IAHR Congress*, 491–498.

Mohanty, P. K., Dash, S. S., & Khatua, K. K. (2012). Flow Investigations in a Wide Meandering Compound Channel. *Int. J. Hydraul Eng.,* 1(6), 83– 94.

Nassar, M. A. (2011). Multi-parametric Sensitivity Analysis of CCHE2D for Channel Fow Simulation in Nile River. *J. Hydro. Environ. Res.,* 5, 187–195

Roca, M., Martin Vide, J. P., & Blanckaert, K. (2007). Reduction of Bend Scour by an Outer Bank Footing: Footing Design and Bed Topography. *J. Hydraul. Eng.*, 133, 139–147.

Scott, S. H., & Jia, Y. (2005). Simulation of Sediment Transport and Channel Morphology Change in Large River Systems. *Us-China Workshp On Advanced Computational Modelling In Hydroscience & Engineering*.

Singh, V. (2005). Two Dimensional Sediment Transport Model Using Parallel Computers. *Doctoral Dissertation*, Faculty of the Louisiana State University and Agricultural and Mechanical College in partial fulfillment of the requirements for the degree of Master of Science in Civil Engineering in The Department of Civil and Environmental Engineering by Vikas Singh B. Tech., Banaras Hindu University, India.

Tominaga, A., & Nagao, M. (2000). Secondary Flow Structure in Bends of Narrow Open Channels with Various Cross Sections. *Proceedings of the 4th International Conference on Hydroscience and Engineering*, Seoul, Korea, 26–29 September 2000.

Ye, J., & Mccorquodale, J. A. (1998). Simulation of Curved Open Channel Flows by 3D Hydrodynamic Model. *J. Hydraul. Eng*., 124(7), 687-698.

Yusefi Haghivar, M., Behdarvandi Askar, M., Moalemi, S. (2017). Investigation Fow Depth and Fow Speed Changes in the Karun River. *Open J. Mar. Sci.,* 7, 289–299. https://doi.org/10.4236/ ojms.2017.72021